On Microstructure and Corrosion Behavior of AlSi10Mg Alloy Fabricated by Direct Metal Laser Sintering

By

Parisa Fathi Ahad Beklo

A thesis

presented to the Memorial University of Newfoundland

in partial fulfillment of the

thesis requirement for the degree of

Master of Engineering

in

Mechanical Engineering

St. John’s, Newfoundland and Labrador, Canada

AUTHOR'S DECLARATION

I hereby declare that I am the sole author of this thesis. This is a true copy of the thesis, including any required final revisions, as accepted by my examiners. I understand that my thesis may be made electronically available to the public.

ABSTRACT

Direct metal laser sintering (DMLS) is an additive manufacturing technique that creates near-net-shape functional components by selectively melting metal powders in two dimensions layer by layer using a high power laser as a heat source. The current thesis details (*i*) the corrosion behavior and microstructure of DMLS-AlSi10Mg_200C versus die cast A360.1 aluminum, confirming that the corrosion resistance of the alloy processed through DMLS was significantly better than the cast counterpart, (*ii*) effects of surface finishing procedure, *i.e*. grinding, polishing, and sandblasting, on corrosion behavior of DMLS-AlSi10Mg_200C Alloy *vs* die-cast A360.1 aluminum, highlighting a better corrosion resistance of DMLS-AlSi10Mg_200C than its cast counterpart with similar surface finish, and (*iii*) the microstructure and corrosion behaviour of AlSi10Mg alloy with low surface roughness fabricated by direct metal laser sintering, elucidating the dominant impact of the alloy's microstructure on controlling the electrochemical performance of the as-printed samples than their surface roughness.

ACKNOWLEDGEMENTS

I would like to sincerely thank my supervisor, Dr. Xili Duan. I would also like to thank Dr. Mohsen Mohammadi from Marine Additive Manufacturing Centre of Excellence (MAMCE), University of New Brunswick, Fredericton, for providing the DMLS fabricated specimens and for useful technical discussions throught the duration of this project.

DEDICATION

To My Loving & Wonderful family:

Ali, Elena, and Aiden

TABLE OF CONTENTS

LIST OF FIGURES

LIST OF TABLES

Chapter 1

INTRODUCTION AND OVERVIEW

1.1 Background

Additive Manufacturing (AM) or "3D printing" refers to processes used to synthesize three-dimensional objects from CAD data in which successive layers of material are formed under computer control [1]. Additive manufacturing offers notable advantages over the traditional manufacturing processes, including geometrical and design flexibility leading to a near-net-shape component, higher productivity, reduced materials and energy, environmentally friendly, and cost efficiency [2]. In particular, Direct Metal Laser Sintering (DMLS) [3], also known as Selective Laser Melting (SLM) [1], Laser Beam Melting (LBM) [3], or Laser Metal Fusion (LMF) (Trumpf GmbH & Co. KG), is an additive manufacturing technology for fabrication of metallic components by precise melting of the powder metal in two dimensions layer by layer using a high power laser as the heat source until the near-net-shape part in 3D is produced [5].

The use of lightweight Al alloys in modern manufacturing has drastically increased during the last two decades [6]. Among these alloys, Al-Si-Mg alloys are widely used in the automotive, marine, and aerospace industries, because of their high strength and stiffness to weight ratio, low density, and good corrosion resistance [7]. In particular, Al-Si10-Mg alloy is extensively fabricated using the DMLS process primarily due to its reduced coefficient of thermal expansion, leading to low solidification shrinkage and

reduced susceptibility to hot cracking during solidification [8]. Also, a slight addition of Mg to this alloy (0.20–0.45 wt.% Mg) provides precipitation hardening for the alloy by forming Mg_2Si precipitates upon aging treatments [9,10]. To further benefit from the advanced applications of these strategically vital alloys, they have been also adopted by the additive manufacturing industry as a strong candidate for various engineering applications. So far, the major research on this alloy has been focused on the evolution of microstructure and mechanical properties of the alloy processed through various DMLS processing parameters [11–18], where very little work has been done to understand the corrosion behavior of the DMLS-AlSi10Mg alloy.

The impact of microstructure on the corrosion resistivity of additively manufactured AlSi10Mg alloy has been researched in a few recent studies. Cabrini *et al*. [19] investigated the impact of different post-heat treatments, *i.e*., stress relieving and high temperature annealing followed by water quenching, on corrosion behavior of DMLS-AlSi10Mg alloy. The authors demonstrated that the low temperature stress relieving at 537 K does not affect the susceptibility of the alloy to the selective attack in Harrison solution [19]. However, high temperature annealing at 823 K was reported to promote localized corrosion attack resulted from the accelerated galvanic coupling between the coarse Si particles and surrounding Al matrix [19]. In another study, Cabrini *et al*. [20] outlined the corrosion performance of heat treated laser powder bed fusion AlSi10Mg alloy ranging from 200 °C to 500 °C through intergranular corrosion testing as per ISO 11846 and reported increased susceptibility of the alloy to selective corrosion attack along the melt pool boundaries after

stress relieving in the range of 200 to 300 °C, in contrast to the results observed in their previous study [19]. However, higher temperature heat treatments, *i.e*. 400 °C and 500 °C, were reported to prevent the occurrence of selective corrosion attack along the melt pool boundaries of the alloy as the coarse Si network structure adjacent to the melt pool boundaries starts to disappear at temperatures higher than 400 °C [20]. The local Volta potential analysis results taken from the melt pool borders, reported by Revilla *et al*. [21], confirmed a higher potential difference between the Si phase and the α-Al matrix in the border regions with coarser structure, representing a greater driving force for galvanic corrosion.

Cabrini *et al*. [22] have also evaluated the effect of building direction combined with different surface finishing, including mechanical polishing and shot peening, on corrosion resistivity of DMLS-AlSi10Mg alloy. An improved corrosion resistance was reported for the polished as well as smooth shot-peened surfaces relative to that of the rough as-printed ones [22]. Additionally, the authors reported a reduced corrosion resistance of the surfaces parallel to the building direction (side plane), which was attributed to the higher density of the melt pool borders containing a higher concentration of coarser Si particles [22]. In a similar study on a different Al-Si alloy, Chen *et al*. [23] also studied the anisotropy in corrosion properties of SLM produced Al-12Si and pointed out an opposite behavior. The observed lower corrosion resistance of the building plane (top plane) compared to the plane parallel to the building direction was ascribed to the morphology of the Si phase, having deep and small-bore Si shells embedded in the Al matrix [23]. The authors explained that

the growth of corrosion products on the building plane could cause cracking of the Si shells and consequently degradation of corrosion performance, as opposed to the side plane, containing shallow and large-bore Si shells [23].

Cabrini *et al*. [24] also evaluated the effect of a conversion treatment by short immersion of the AlSi10Mg samples in Ce(III) salt solution. This post-treatment process was not found to be effective in inhibiting corrosion on the as-printed specimen, but was reported to be more effective on polished and pickled surfaces [24]. In a similar study, Leon and Aghion [25] explored the effect of surface roughness on both general corrosion and corrosion fatigue behaviors of additively manufactured AlSi10Mg processed through SLM, by comparing the as-printed surfaces with the polished ones. An improved corrosion resistance and a higher low cycle corrosion fatigue life span were reported for the polished surfaces over the as-printed ones, associated with increased surface roughness of the as-printed sample [25].

One of the limitations of SLM/DMLS manufactured Al alloys components in as-printed condition is their rough surfaces [26]. Balling and dross formation in the melt pool during solidification of the part have been reported as the main reason for the formation of a rough printed surface with arithmetical mean deviation value (R_a) in the range of 8-20 μm in the as-printed condition [27]. This superficial roughness can be detrimental to both fatigue [28] and corrosion properties [22] of the alloy. To improve the surface quality and lower the surface roughness of an additively manufactured component, various post processing techniques have been implemented so far on as-printed surfaces, including

mechanical polishing [22,28], laser polishing [29], chemical etching [30], shot peening [27], sandblasting [31], and grinding [32]. However, the properties of the post processed AM parts, in particular, the electrochemical stability and corrosion performance of the surface, have not been studied extensively. In this context, despite the above mentioned two studies by Cabrini *et al*. [22] and Leon and Aghion [25] were focused on the impact of surface quality on the corrosion behavior of additively manufactured AlSi10Mg, yet, a comprehensive study is needed to understand the influence of commonly used surface finishing procedures, such as post grinding or sandblasting, on the corrosion behavior of additively manufactured AlSi10Mg alloy. There is no previous investigation on the corrosion performance of DMLS-AlSi10Mg subjected to the post-grinding or sandblasting process.

Therefore, a comprehensive review of the literature revealed that the knowledge on the corrosion performance of DMLS produced Al alloys, especially in as-printed and in regular service conditions without surface preparation, is very limited. In addition, the impacts of various surface finishing procedures, including grinding and sandblasting, are still unknown on the sensitivity of the alloys to localized corrosion attack particularly in the presence of chloride. Furthermore, there is no study in the open literature that directly evaluates the microstructural modification and the resultant corrosion performance of a DMLS-AlSi10Mg part through changing the printing process parameters.

1.2 Objectives

The aim of this thesis is to conduct an experimental analysis to (*i*) investigate corrosion behavior of the DMLS-AlSi10Mg_200C alloy in compared with its cast counterpart (Die cast A360.1 Al alloy) with the particular focus on the microstructure and the formed micro-constituents after each manufacturing process, (*ii*) investigate the impact of surface finishing on corrosion performance of AlSi10Mg_200C alloy manufactured through DMLS *versus* cast A360.1 aluminum in seawater environment, (*iii*) achieve a comprehensive understanding of the microstructure and corrosion properties of DMLS-AlSi10Mg parts with significantly lowered surface roughness obtained by tuning the DMLS process parameters instead of applying a post-printing operation.

1.3 Organization of Thesis

This thesis is prepared in a paper-based format and is subdivided into four chapters. Overall, the outcomes of this MEng research work led to three peer-reviewed journal publications (Chapters 2-4) and another two conference papers. The details of each publication are listed below.

Journal Publications

1. **P. Fathi**, M. Mohammadi, X. Duan, A.M. Nasiri, "A comparative study on corrosion and microstructure of direct metal laser sintered AlSi10Mg_200C and die cast A360.1 aluminum", *Journal of Materials Processing Technology* (Impact Factor: 3.817), Volume 259, 2018, pp. 1-14.

2. **P. Fathi**, M. Mohammadi, X. Duan, and A.M. Nasiri, "Effects of Surface Finishing Procedure on Corrosion Behavior of DMLS-AlSi10Mg_200C Alloy *vs* Die Cast A360.1 Aluminum", *JOM (Journal of The Minerals, Metals & Materials Society)* (Impact Factor: 2.471), 2019, pp. 1-12.

3. **P. Fathi**, M. Rafieazad, X. Duan, M. Mohammadi, A.M. Nasiri, "On Microstructure and Corrosion Behaviour of AlSi10Mg Alloy with Low Surface Roughness Fabricated by Direct Metal Laser Sintering", *Corrosion Science Journal* (Impact Factor: 5.238), In Press, Available online 31 May 2019.

Conference Publications

4. **P. Fathi**, M. Rafieazad, M. Mohammadi, X. Duan, and A.M. Nasiri, "Effect of Surface Finishing Procedures on Corrosion Resistance of DMLS-AlSi10Mg_200C Alloy", *International Conference on Aluminum Alloys (ICAA16*), June 17-21, 2018, Montreal.

5. **P. Fathi**, M. Mohammadi, X. Duan, A. Nasiri, "A Comparative Study of Microstructure and Corrosion Resistance of Additively Manufactured AlSi10Mg and Aluminum A360.1 Die Casting", 29th Canadian Materials Science Conference (CMSC-2017), June 20-23, 2017, University of Ottawa, Ottawa, Canada.

In this thesis, Chapter 1 details a comprehensive review of the literature relevant to the additive manufacturing (DMLS) of AlSi10Mg, and in particular is focused on the corrosion performance of the alloy. Chapter 2 provides details on the corrosion and microstructure of Direct Metal Laser Sintered AlSi10Mg_200C and Die Cast A360.1 Aluminum. Chapter 3 reports the effects of surface finishing procedure on corrosion behavior of DMLS-AlSi10Mg_200C alloy *vs* Die Cast A360.1 Aluminum. Chapter 4 documents investigations on the microstructure and corrosion behaviour of AlSi10Mg alloy with low surface

roughness fabricated by direct metal laser sintering. Finally, Chapter 5 provides a summary and recommendations for future research.

1.4 Co-authorship Statement

For all the publications esteemed from this MEng research listed in the previous section, I am the primary author of the articles. As the primary author, I carried out the literature review for each publication, performed the experimental procedure, gathered the results, and prepared the manuscript. The contributions from the co-authors, *i.e*. M. Mohammadi, X. Duan, and A. Nasiri, included reviewing the results, reviewing and revising the prepared manuscripts. The co-author M. Rafieazad in the third journal publication contributed through performing the EBSD and some SEM analysis of the fabricated samples.

Chapter 2

A Comparative Study on Corrosion and Microstructure of Direct Metal Laser Sintered AlSi10Mg_200C and Die Cast A360.1 Aluminum[1]

2.1 Abstract

Direct metal laser sintering (DMLS) is an additive manufacturing technique that creates near-net-shape functional components by selectively melting metal powders in two dimensions layer by layer using a high power laser as a heat source. This technique offers to create parts with complex net-shape structures at an affordable cost with the least lead time. The main purpose of this study is to investigate the corrosion behavior and microstructure of AlSi10Mg_200C manufactured using DMLS compared with its die-cast counterpart (A360.1 die-cast Al alloy). The impact of the alloy's surface finish, *i.e*. as-printed surface versus as-ground one, on the corrosion performance was also investigated. Several AlSi10Mg_200C cube samples were additively manufactured through DMLS technique. In addition, the same size cubes were cut from an aluminum A360.1 die-cast ingot. The corrosion behavior of the two alloys was analyzed utilizing potentiodynamic polarization testing and electrochemical impedance spectroscopy in aerated 3.5 wt.% NaCl

[1] P. Fathi, *et al*., *Journal of Materials Processing Technology* (Impact Factor: 3.817), Volume 259, 2018, pp. 1-14 [116].

P. Fathi, *et al*., 29th Canadian Materials Science Conference (CMSC-2017), June 20-23, 2017, University of Ottawa, Ottawa, Canada.

solution to mimic sea water environment at 25°C. Further, the microstructures and composition of the samples before and after corrosion testing were investigated using Optical Microscopy (OM), Scanning Electron Microscopy (SEM), and Energy Dispersive X-ray (EDX) spectroscopy. The results confirmed that the corrosion resistance of the alloy processed through DMLS was significantly better than the cast counterpart. This was attributed to the fine microstructure produced by DMLS, uniform distribution of the fine Si particles without the formation of any intermetallic, due to the extremely rapid cooling and solidification rate during DMLS process and slightly lower Fe and Cu concentration of the AlSi10Mg alloy. In contrast, the A360.1 cast Al alloy samples experienced severe localized corrosion of the Al matrix in the periphery of the Fe containing IMC and Si flakes. The results also highlighted improved corrosion resistance of the as-printed DMLS sample compared with that of the as-ground one.

2.2 Introduction

Additive Manufacturing (AM) or "3D printing" refers to processes used to synthesize three-dimensional objects from CAD data in which successive layers of material are formed under computer control [1]. Additive manufacturing offers notable advantages over the traditional manufacturing processes, including geometrical and design flexibility leading to a near-net-shape component, higher productivity, reduced materials and energy, environmentally friendly, and cost efficiency [2]. In particular, Direct Metal Laser Sintering (DMLS) [3], also known as Selective Laser Melting (SLM) [1], Laser

Beam Melting (LBM) [3], or Laser Metal Fusion (LMF) [4], is an additive manufacturing technology for fabrication of metallic components by precise melting of the powder metal in two dimensions layer by layer using a high power laser as the heat source until the near-net-shape part in 3D is produced [5].

Marine and shipbuilding industries are among the fastest growing sectors demanding to adopt additive manufacturing [33]. Different alloys such as titanium [34], stainless steels [33], hard steels [35], aluminum [36], nickel aluminum bronze [37], and copper alloys [38] in general are of particular interest of this industry. However, in order to adopt AM to fabricate these alloys for different applications, their intrinsic properties such as basic mechanical properties [39], fatigue [40], high strain rate behavior [41], corrosion fatigue [25], corrosion [21], and heat treatment [42] should be studied. This is due to the extensive presence of random ocean wave loadings, ambient and cold temperatures, seawater corrosive environment, and crush, ballistic, and impact loadings around marine structures.

Aluminum alloys with silicon and magnesium as major alloying elements have created a class of lightweight metallic material possessing decent mechanical properties and corrosion performance [7]. These alloys provide the largest family of all shaped cast components, with a broad range of applications in automotive, aerospace, and particularly marine industry [43]. To further benefit from the advanced applications of these strategically vital alloys, they have been also adopted by the additive manufacturing industry as a strong candidate for various engineering applications. Among all the alloys in this family, AlSi10Mg is one of the most commonly used ones for the DMLS process

[40], which is mainly attributed to its reduced coefficient of thermal expansion, leading to low solidification shrinkage, reduced susceptibility to hot cracking during solidification, and also its solidification characteristics [39]. Previous studies [44,45] confirmed that AlSi10Mg alloy fabricated through DMLS has higher mechanical strength and hardness than traditional cast A360 alloy (similar composition). This was mainly attributed to the fine microstructure resulted from extremely rapid cooling and solidification rate during DMLS process [42,46].

The corrosion behavior of Al-Si-Mg alloys produced by traditional processes, such as casting, is generally known. Szklarska-Smialowska [47] has reported the impact of second phase particles and intermetallics on corrosion behavior of aluminum. The intermetallic phases containing Fe and Cu have been found to be cathodic with respect to the α-Al matrix [48]. Guillaumin and Mankowski [49] also reported that coarse Al–Si–Mg-containing intermetallic act as nucleation sites for pits in 1M NaCl solution, gradually leading to intergranular corrosion. The impact of the second phase and intermetallics was also studied by Fratila-Apachitei *et al*. [50] and Andreatta *et al*. [51] on AlSi(Cu) and 7075 alloys, respectively, in a dry environment using scanning Kelvin probe force microscopy. Fratila-Apachitei *et al*. [50] reported a positive Volta potential difference relative to α-Al matrix for all the formed intermetallics and precipitates in the cast AlSi(Cu) alloy, including Al-Fe, Al-Fe-Si, and Al_2Cu, suggesting that they all are noble with respect to the aluminum matrix. Andreatta *et al*. [51] also observed that solutionizing heat treatment increases the

Volta potential difference between the intermetallics and the matrix in AA7075 alloy, leading to a stronger galvanic couple between the matrix and the intermetallics.

However, the knowledge on the corrosion performance of DMLS produced Al alloys, especially in as-printed and in regular service conditions without surface preparation, is very limited. DMLS built aluminum components are known to have 8-20 µm surface roughness primarily due to balling and dross formation in the melt pool without any post-treatment [27]. The impact of this surface morphology is still unknown on the sensitivity of the alloys to localized corrosion attack particularly in the presence of chloride. This work aims to focus on this gap to investigate corrosion behavior of the DMLS-AlSi10Mg_200C alloy in compared with its cast counterpart (Die cast A360.1 Al alloy) with the particular focus on the microstructure and the formed micro-constituents after each manufacturing process. This study can be used as a roadmap to substitute different conventional alloys with their additively manufactured equivalents.

2.3 Experimental Procedure

Materials

For this study, several AlSi10Mg_200C cube specimens (10 × 10 × 10 mm) were additively manufactured (shown in Figure 2-1) from gas atomized commercial AlSi10Mg_200C powder from EOS using an EOS M290 metal 3D printer machine through DMLS technique (Additive Metal Manufacturing, Inc. (AMM), Concord, ON, Canada). The machine was equipped with a 250 × 250 × 325 mm size platform and a 400 W Yb-fibre laser with 100

μm spot size. The average particle size of the alloy powder with a regular spherical shape was 8.8 ± 7 μm [39]. The nominal composition of the alloy is reported in Table 2-1. To minimize the internal stresses in the printed samples, the DMLS was processed at elevated building platform temperature of 200 °C. The process parameters used during DMLS included laser power of 370 W, scanning speed of 1300 mm/s, hatching distance of 190 μm, and powder layer thickness of 30 μm using strip scanning strategy with 67° laser beam rotation between successive layers. Argon shielding with the oxygen content of 0.1% was applied to minimize the oxidation during the manufacturing process.

Table 2-1: Nominal chemical compositions of AlSi10Mg_200C powder and A360.1 die cast alloy (wt.%)

Element	Si	Mg	Fe	Mn	Ti	Zn	Cu	Al
AlSi10Mg_200C	9.0 - 11.0	0.2 - 0.45	≤ 0.55	≤ 0.45	≤ 0.15	≤ 0.10	≤ 0.05	Bal.
A360.1	9.0 - 10.0	0.4 - 0.6	1.3	0.35	--	0.5	0.6	Bal.

In addition, cubes of the same size (10 × 10 × 10 mm) were cut from an aluminum A360.1 die cast ingot, which has the closest chemical composition to that of the AlSi10Mg_200C. The chemical composition of the A360.1 alloy is also presented in Table 2-1. Due to its near Al-Si eutectic composition and low melting point temperature (see Figure 2-2), this alloy is typically used for cast parts with thin walls and complex geometries.

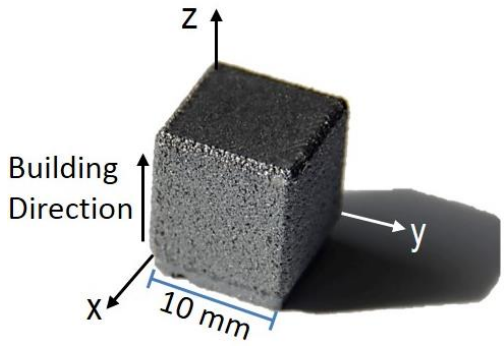

Figure 2-1: DMLS produced cubes from gas atomized AlSi10Mg_200C powder.

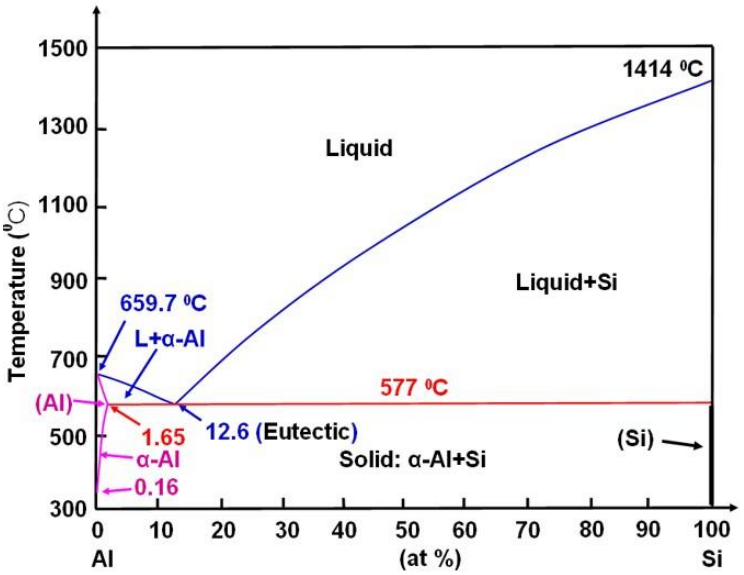

Figure 2-2: Al-Si binary phase diagram (modified from [52]).

Microscopic Characterization

For microscopic analysis of the samples, DMLS produced samples were cut along both building platform plane (x-y plane) and the building direction (z-direction) and mounted in epoxy resin followed by standard grinding and polishing sample preparation procedures.

A similar preparation was applied on the cast sample. To reveal the microstructure of the samples, the polished specimens were then etched using Keller's reagent (2.5 cm^3 HNO_3, 1.5 cm^3 HCl, 1 cm^3 HF, and 95 cm^3 H_2O) for 12 s.

The microstructures and compositions of the samples were observed and analyzed using a Nikon Eclipse 50i optical microscope and an FEI MLA 650F scanning electron microscope equipped with high throughput Bruker energy dispersive X-ray (EDX) analytical system.

Corrosion Testing

Corrosion resistance analysis of the samples, *i.e*. as-printed and as-ground (600 SiC grit finish) DMLS-AlSi10Mg, and as-ground cast sample with 600 SiC grit finish was conducted using an IVIUM CompactStat™ Potentiostat with a three-electrode cell setup. All the tests were repeated at least three times. Experiments were conducted in a multiport glass cell at atmospheric pressure based on the ASTM G5 standard for potentiodynamic polarization measurements [53]. A graphite rod was used as the counter electrode (CE) and saturated silver/silver chloride (Ag/AgCl) was used as the reference electrode (RE). The tested samples were immersed in aerated 3.5 wt.% NaCl solution to simulate sea water corrosion environment. The temperature of the solution was maintained at 25 ± 2 °C. The sample was connected to a copper wire as the working electrode. The applied potential range for the potentiodynamic polarization measurements was from −0.3 V to +0.3 V *vs*. the open circuit potential (OCP) with a scanning rate of 0.125 mV/s. Before the tests, OCP

was monitored for 60 min. After potentiodynamic polarization testing, the microstructures of the samples were studied before and after corrosion products removal. To rapidly remove all the formed corrosion products with minimum removal of the base metal, the samples were immersed in a concentrated HNO_3 solution (15.8 N) in an ultrasonic bath for 30 min [54].

Electrochemical Impedance Spectroscopy (EIS) measurements were also conducted after one hour of immersion time in aerated 3.5 wt.% NaCl solution at 25 °C, with the amplitude perturbation of ±10 mV (sinusoidal potential signal) with respect to the OCP and a frequency range from 10 kHz to 10 mHz with ten points per decade. The impedance spectra were analyzed using IVIUMSOFT electrochemical analysis software.

2.4 Results

Surface Morphology of As-Built DMLS AlSi10Mg_200C

Figure 2-3 shows the SEM micrographs of the typical as-built surface of the AlSi10Mg_200C alloy manufactured by the DMLS process. It is apparent that a high degree of surface irregularity is present as a result of sticking partially melted powder metal particles to the surface. This creates a superficial roughness on the surface of the as-built sample. This roughness is dictated by the DMLS process parameters, including laser power, scan rate, and hatching distance, as shown in a previous study [27].

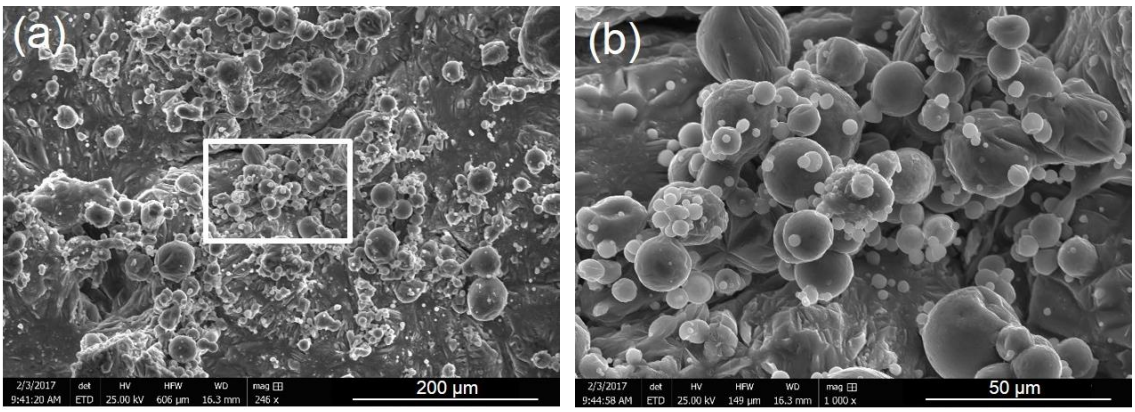

Figure 2-3: (a) SEM photomicrographs of the as-built surface of DMLS-AlSi10Mg_200C sample, (b) higher magnification of the enclosed area in (a).

Microstructure

Optical micrographs of the DMLS produced sample in the as-built condition are shown in Figure 2-4. The well-defined melt pool boundaries can be observed on both top view (perpendicular to the building direction, plane (b) in Figure 2-4a) as well as the front view (plane (c) in Figure 2-4a). The elongated tear-drop shaped features (melt pools (MP)), as shown in Figure 2-4b, were also reported in previous studies [55,56] when a continuous-wave laser beam is used for the DMLS process. The main length of these melt pools on each x-y plane corresponds to the direction of the laser scan, which changes 67° between consecutive layers, resulting in the formation of irregular geometric contours as shown in Figure 2-4b. Due to the size of the melt pool and its rapid solidification rate, the resultant microstructure will be far from equilibrium and contains directional growth features. The side view of the melt pools along the z-axis are shown in Figure 2-4c. This figure shows the semi-circular shape of the overlapped melt pools from the side view representing tracks

of the scan laser with the arrow indicating the building direction. During the building process, the laser beam parameters were modulated to assure a complete melting of each layer of the powdered metal and also partial melting and penetration into the previous layer since a complete wetting between layers is required to achieve a dense component.

Visible irregular porosities were detected mainly at the weld pool boundaries in the DMLS sample with a maximum dimension of ~ 25 μm (shown by small white arrows in Figure 2-4b and Figure 2-4c). The irregular shaped pores could result from the insufficient overlapping between the laser scan tracks or partially melted/unmelted powders. The smaller spherical shaped pores are mainly gas pores resulting from entrapped gases [57].

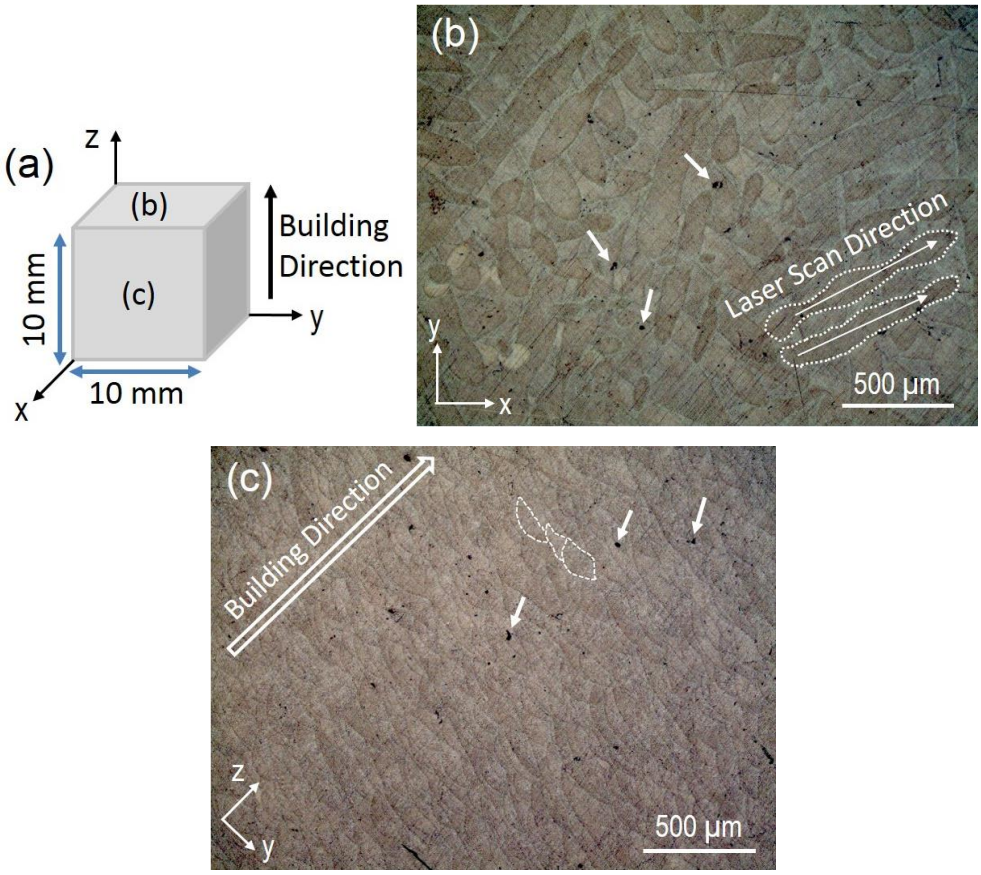

Figure 2-4: (a) Schematic overview of the DMLS-produced sample showing the orientation of the sample. Optical micrographs taken from the AlSi10Mg_200C specimen's (b) top view as shown in (a) (building direction perpendicular to this plane), (c) front view as shown in (a) (along the z-axis).

The SEM images of the top and side views of the DMLS-AlSi10Mg_200C are shown in Fig. 5. Micrographs of both top (Figure 2-5a and Figure 2-5b) and side views (Figure 2-5c and Figure 2-5d) indicated a fine cellular dendritic solidification structure with cells ~ 0.5-2 µm in size containing a continuous network of a secondary phase formed at the

intercellular region. From Figure 2-5a and Figure 2-5c, three different zones can be distinguished across the melt pool (MP), *i.e.* fine cellular structure (MP-Fine, 0.5-1 μm in size) inside the MP, coarse cellular structure (MP-Coarse, 1.5-2 μm in size) approximately 5-10 μm from the MP border, and the heat affected zone (HAZ) around the MP in the adjacent melt pool with the average width of 5 μm, where the structure experiences high temperature just below their melting point temperature. This has resulted in breakage of the intercellular network in the HAZ by coarsening of the intercellular phase, as evidenced by Figure 2-5b and Figure 2-5c. Side view's microstructure (Figure 2-5c and Figure 2-5d) clearly shows non-equilibrium directional solidification features indicating cellular growth towards the centre of the MP, as demonstrated by the dashed arrow in Figure 2-5c.

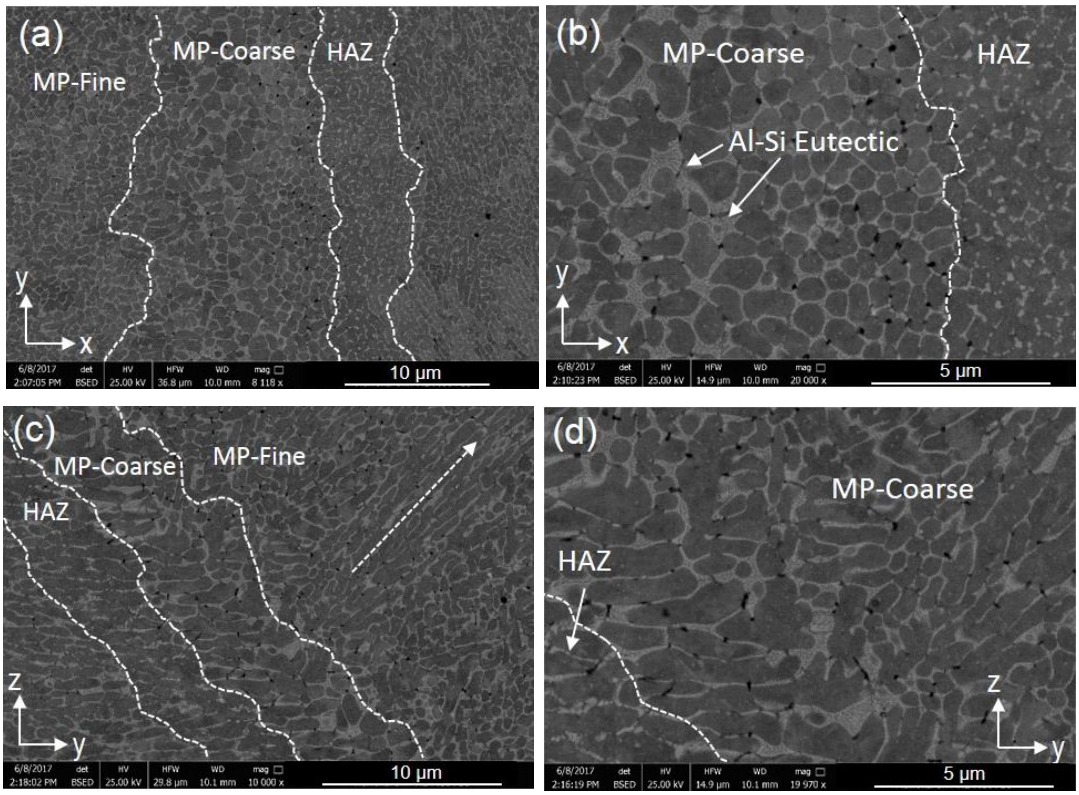

Figure 2-5: SEM micrographs of DMLS-AlSi10Mg_200C: (a), (b) top side plane (plane (b) as shown in Fig. 4a), (c) and (d) a cross section along the building direction (plane (c) as shown in Fig. 4a).

EDX mapping analysis of the melt pool was performed to investigate the compositional dependence of the microsturture in more detail. The EDX maps of Al, Si, Mg, Mn, and Cu along with the superimposed image of all maps are shown in Figure 2-6. The results confirmed that the cells are primarily composed of α-Al solid solution while Si is preferentially precipitated along the cellular boundaries. It can be observed that other elements, *i.e*. Mg, Mn, and Cu, are more uniformly distributed compared to Si. Similar fine structure of α-Al matrix decorated with a network of Si-phase has been reported in various

previous studies, such as by Rosenthal *et al*. [58]. Formation of Al-Si lamellar eutectic structure was also detected primarily in the MP-coarse region (Figure 2-5b).

Cellular dendritic structure typically forms when metal solidifies with a very high velocity of the solidification front and minimum solute concentration [59]. In Al-Si alloys, it has been reported that high cooling rates can extend the solubility of Si in Al (Birol, 2007). The DMLS technique, similar to other laser additive metal manufacturing processes, is able to generate very high cooling rates (10^3-10^{11} K/s) [62], thus leading to increased solid solubility of Si in Al matrix. Consequently, the degree of constitutional under cooling is reduced since Si concentration in the liquid phase decreases. In addition, the extremely rapid cooling rates of the DMLS process and the resultant rapid solidification lead to an extremely high velocity of solidification front. Therefore, a cellular dendritic structure forms in DMLS-AlSi10Mg_200C.

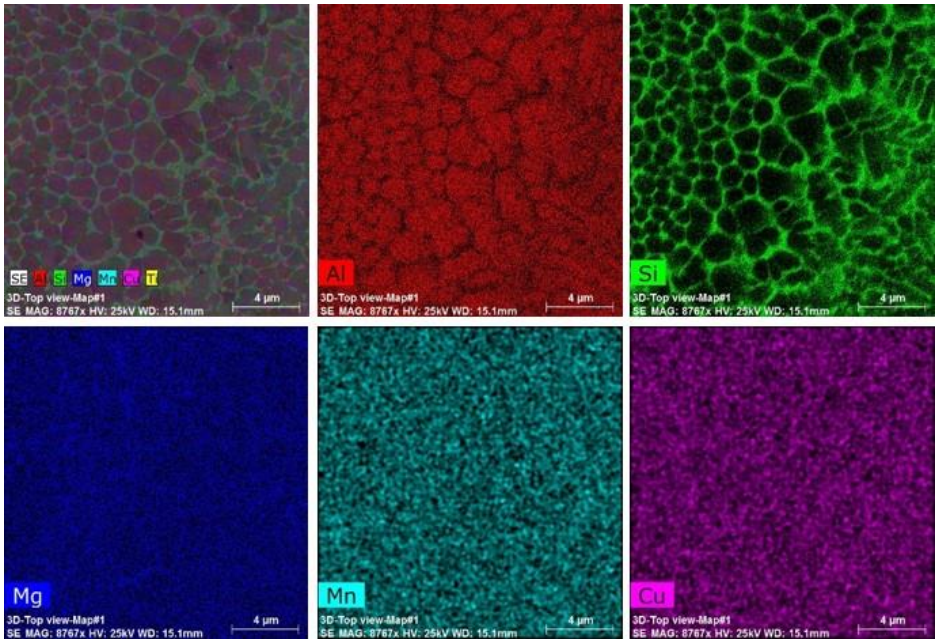

Figure 2-6: SEM-EDX concentration maps taken from the DMLS-AlSi10Mg_200C melt pool structure indicating maps of Al, Si, Mg, Mn, and Cu.

Figure 2-7 shows the SEM micrographs of the microstructure of the A360.1 cast sample. The microstructure of the alloy consisted of solid-solution α-Al matrix, and various types of micro-constituents, including Chinese script-shaped large cored phases, needle-like/platelet-shaped features, and irregular shaped dispersed particles. According to the EDS point and mapping analysis results (Figure 2-8), the Chinese script phase and also some of the light gray needle-like shaped features containing 66.5 ± 0.8 wt.% Al, 22.1 ± 1.0 wt.% Fe, 8.2 ± 0.2 wt.% Si, 2.3 ± 0.1 wt.% Cu, and 0.9 ± 0.1 wt.% Mg represented the α-$Al_{15}(Fe,Mg,Cu)_3Si_2$ stoichiometric intermetallic compound (IMC), presented in Figure 2-7b. It has been reported that the presence of AlFeSi IMC degrades mechanical properties and corrosion resistivity of the alloy, primarily due to the morphology and low adhesion of

this phase to the α-Al matrix [63]. The addition of Mg or Mn to the composition of this alloy minimized the formation of detrimental AlFeSi IMC by forming the α-$Al_{15}(Fe,Mg)_3Si_2$ and Mg_2Si phases, resulting in mechanical and corrosion properties improvement of the alloy [64].

The platelet shaped features and irregular shaped dispersed particles contained 100 wt.% Si were identified to be eutectic Si particles. In addition, SEM-EDX mapping analysis results confirmed existence of an irregular-shaped phase with a high Mg concentration containing 18.5 ± 0.5 wt.% Al, 16.2 ± 0.8 wt.% Cu, 34.6 ± 1.5 wt.% Mg, and 30.7 ± 1.2 wt.% Si, which was found to be $Al_4Cu_2Mg_8Si_7$ with honeycomb structure (shown in Figure 2-7c). The literature data revealed that the Mg content of the Al-Si-Mg alloy leads to the formation of this honeycomb type AlMgSiCu intermetallic [65].

SEM micrographs of the cast structure also revealed a plate/needle-like shaped precipitate containing 60.1 ± 2.1 wt.% Al, 27.2 ± 0.6 wt.% Fe, and 12.7 ± 0.5 wt.% Si. This phase is visible on both Figure 2-7a and Figure 2-7c. The compositional analysis results and the literature data revealed that this needle-like phase corresponds to β-Al_5FeSi intermetallic [66].

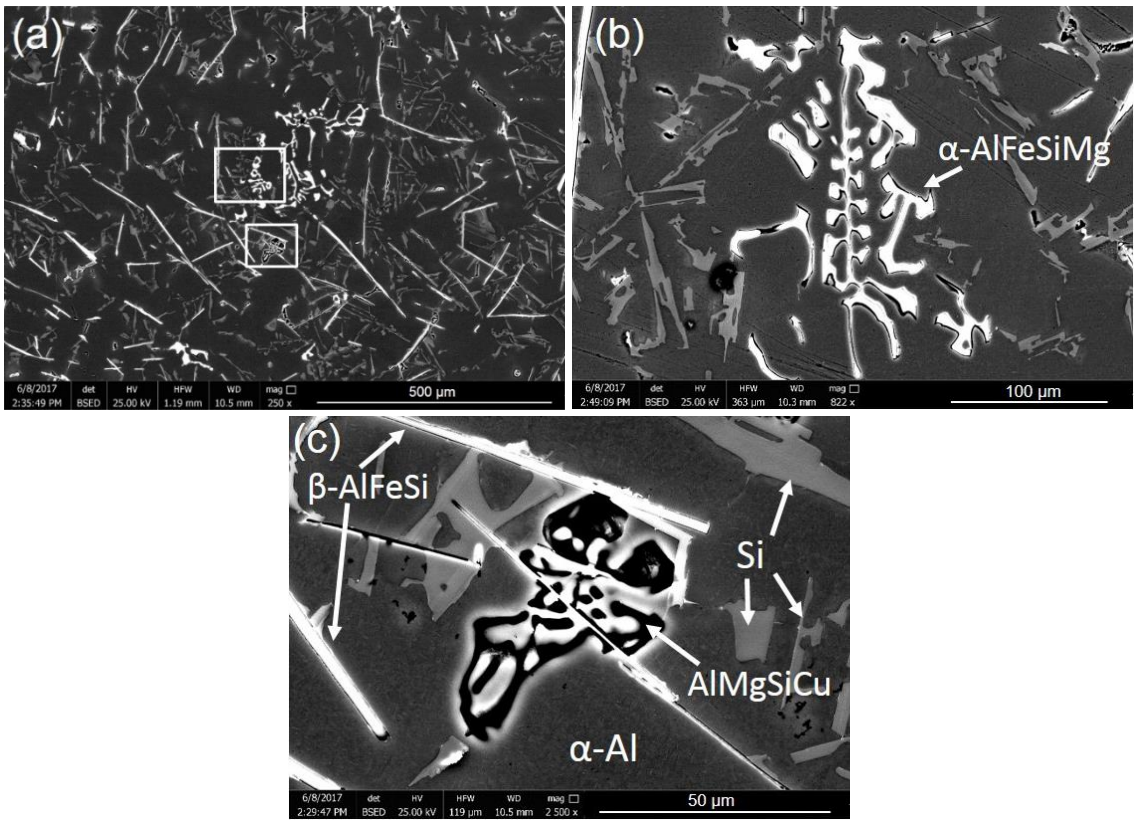

Figure 2-7: SEM micrographs of the die cast A360.1 Al alloy at different magnifications.

(b) and (c) are the higher magnifications of the enclosed areas in (a).

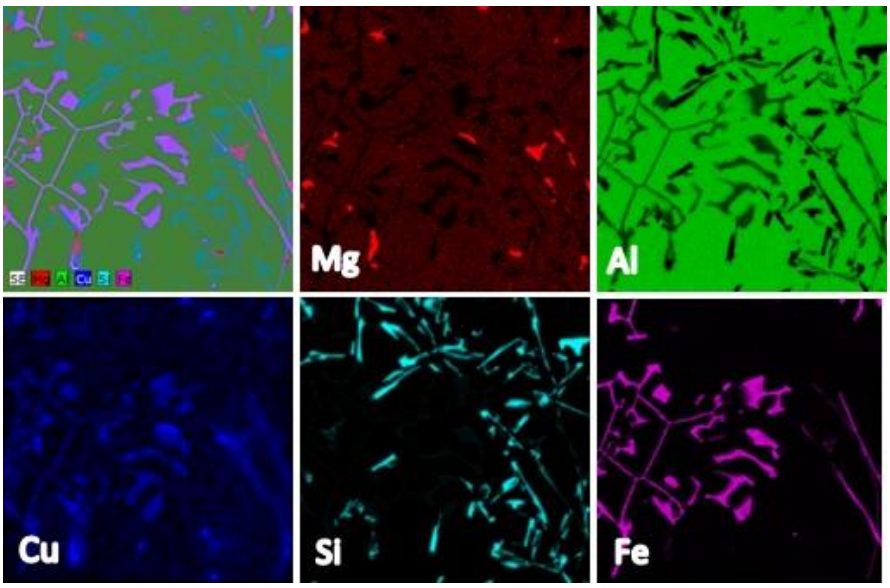

Figure 2-8: SEM-EDX concentration maps taken from the die cast A360.1 Al alloy microstructure indicating maps of Mg, Al, Cu, Si, and Fe.

Potentiodynamic Results

The potentiodynamic polarization plots in Figure 2-9 show corrosion behaviors of all samples comparing the DMLS-AlSi10Mg_200C in as-printed and as-ground surface condition with the A360.1 cast alloy. The preliminary observation of the graphs confirms a higher corrosion resistivity in DMLS samples than the cast alloy sample since as a general trend, better corrosion resistance is shown by an increase in corrosion potential and a decrease in corrosion current density (shown by the dashed arrow in Figure 2-9).

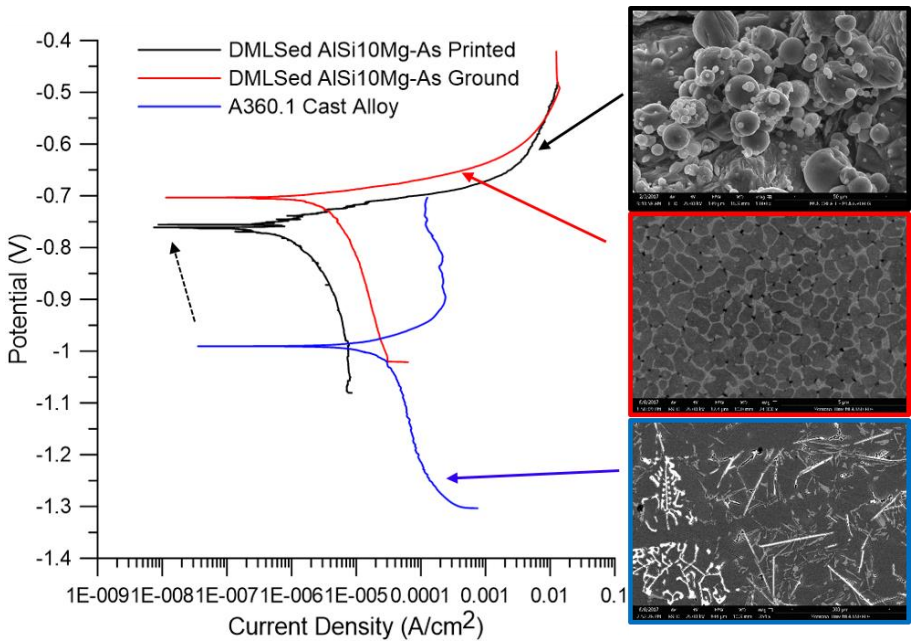

Figure 2-9: Potentiodynamic curves comparing the corrosion behavior of DMLS-AlSi10Mg_200C with as-printed and as-ground surface finish to A360.1 cast alloy.

Table 2-2 presents the extracted data from the potentiodynamic plots shown in Figure 2-9 including the corrosion potential, polarization resistance, corrosion current density, and the corrosion rate of each of the samples. The shift in corrosion potential of the samples from the lowest (for the cast sample) to the highest potentials (for the as-ground DMLS sample) can be ascribed to several factors, such as variation in the volume fraction and the type of existing micro-constituents in the structure, *i.e.* Si and other IMCs, and also uniformity of the corrosion layer on the surface. Cathodic branches of the plots for all samples indicate a narrow current region, suggesting a cathodic-controlled corrosion reaction in the aerated NaCl electrolyte. The lower cathodic current density range of the

as-printed DMLS sample confirms that the cathodic reaction was more effectively hindered in this sample compared to the other two samples.

The as-printed DMLS samples evidenced a very limited passive region just above its corrosion potential. The sharp increase in the corrosion current density of the as-ground DMLS-AlSi10Mg sample in the anodic branch suggests that the surface pitting was freely initiated at the corrosion potential, corresponding to an approximately equal values of corrosion potential and pitting potential. The steeper slope on the anodic branch of the as-printed sample indicated a greater passivation tendency for this sample than the as-ground DMLS sample. For the cast alloy, the corrosion potential has shifted to more active values (-0.98 V *vs*. OCP) and the polarization plot shows a passive region, indicating that the corrosion process is under anodic control.

In general, the as-printed DMLS sample shows an improved corrosion resistance by a factor of 28 compared with that of the cast sample (comparing the corrosion current density of 0.0310 mA/cm^2 for the cast alloy *vs*. 0.0011 mA/cm^2 for the as-printed DMLS sample) despite its rougher surface. The results also revealed that the corrosion potential of the DMLS sample with the ground surface was slightly higher than the as-printed one (-0.706 V *vs*. -0.770 V), while the corrosion current density was relatively raised (0.0047 mA/cm^2 *vs*. 0.0011 mA/cm^2). Therefore, even though the as-ground samples had a smoother surface finish, there is a loss of corrosion resistance after grinding operation.

Table 2-2: Potentiodynamic polarization parameters obtained for A360.1 cast alloy and DMLS-AlSi10Mg_200C in 3.5 wt.% NaCl solution

Sample	Corrosion potential (V)	Polarization resistance (Ohm)	Anodic slope (V/dec)	Cathodic slope (V/dec)	Corrosion current density (A/cm^2)	Corrosion rate (mm/year)
A360.1 Cast Alloy	-0.980 ± 0.078	162.9 ± 14.665	0.062 ± 0.005	0.476 ± 0.048	$31.05 \pm 2.640 \times 10^{-6}$	0.327 ± 0.028
AlSi10Mg_200C As-Printed	-0.770 ± 0.120	2955 ± 470.850	0.034 ± 0.007	0.192 ± 0.037	$1.146 \pm 0.172 \times 10^{-6}$	0.013 ± 0.002
AlSi10Mg_200C As-Ground	-0.706 ± 0.077	686.4 ± 77.231	0.029 ± 0.003	0.350 ± 0.042	$4.775 \pm 0.524 \times 10^{-6}$	0.055 ± 0.006

Corrosion Morphology

Figure 2-10 shows the SEM images from the surfaces of the corroded samples after the electrochemical testing. The A360.1 cast sample (Figure 2-10a and Figure 2-10b) revealed non-uniform corrosion of the surface with some corrosion pits and large corroded areas. A significant amount of corrosion products was also detected on the surface. In comparison, Figure 2-10c and Figure 2-10d clearly evidenced that the rough surface of the as-printed DMLS produced sample after the potentiodynamic polarization test remains very similar to that before the test (compare Figure 2-3a to Figure 2-10c) without any significant pitting attack. In contrast, the as-ground DMLS produced sample revealed some pitting attacks along the melt pool boundaries with some corrosion products accumulated on the surface, but not as significant as the A360.1 cast sample (compare Figure 2-10f with Figure 2-10b).

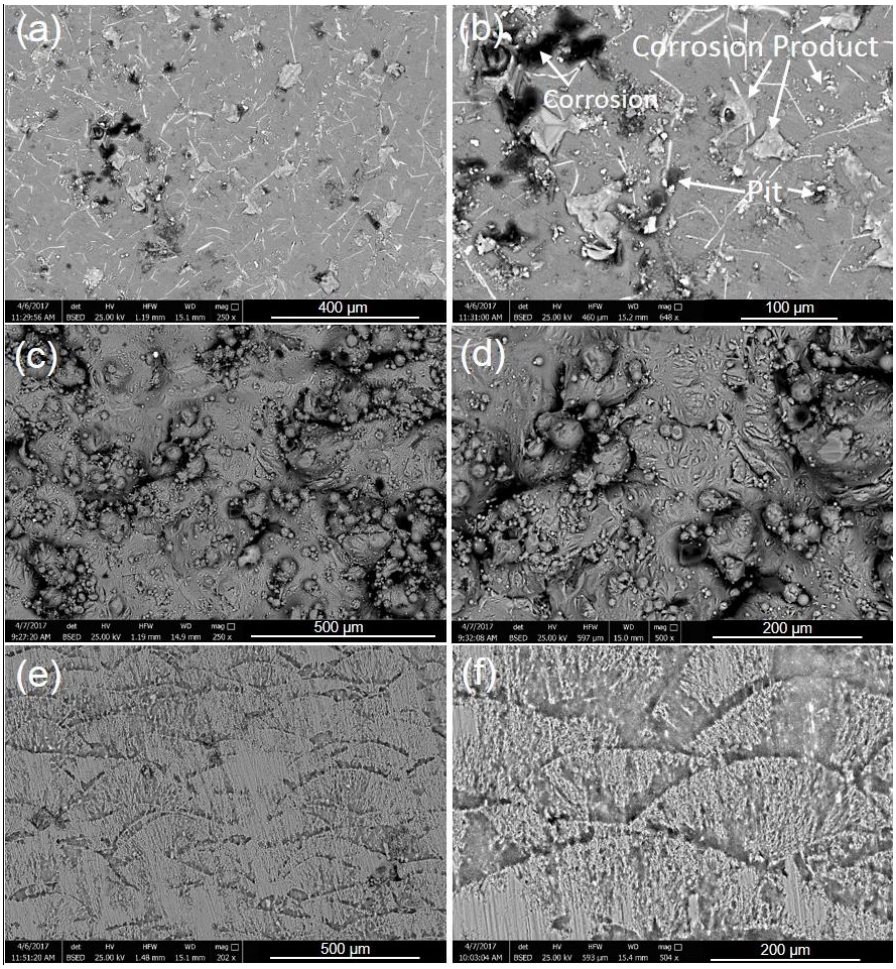

Figure 2-10: SEM images of the surface after the potentiodynamic test before removing corrosion products, (a) and (b) A360.1 cast alloy, (c) and (d) as-printed DMLS-AlSi10Mg_200C, (e) and (f) as-ground DMLS-AlSi10Mg_200C.

In order to investigate the severity of the corrosion attack on the surface of all samples following the electrochemical testing, the formed corrosion products were removed by immersing the samples in concentrated HNO_3 solution for 30 min, as recommended by Ferrer and Kelly [54]. SEM micrographs of the A360.1 cast alloy surface after removing

corrosion products are shown in Figure 2-11 followed by its EDX concentrations maps presented in Figure 2-12. Microstructural analysis of the corroded A360.1 cast alloy surface confirmed severe corrosion in the form of large pits. As shown by the red arrows in Figure 2-11, localized corrosion of the α-Al matrix at the periphery of α-AlFeMgSi and β-FeAlSi IMCs, and Si precipitates can be detected. Therefore, $Al_{15}(Fe,Mg)_3Si_2$ dendrite, β-Al_5FeSi IMC, and Si phase form a micro-galvanic cell with α-Al matrix and function as localized cathodes. This stimulates the micro-galvanic corrosion of anodic α-Al matrix near the periphery of these micro-constituents. The Mg-rich phase ($Al_4Cu_2Mg_8Si_7$) was not detected on the surface of the corroded sample, and therefore, it has been dissolved from the surface during the potentiodynamic polarization testing. The SEM-EDX concentration maps in Figure 2-12 confirm that localized corrosion attack has removed the $Al_4Cu_2Mg_8Si_7$ IMC from the location marked by the thick white arrow in Figure 2-11b. It was also reported by Pech-Canul *et al*. [67] that Mg from the Mg-rich intermetallic phase preferentially dissolves in chlorides solution. The addition of Mg to this alloy and the subsequent formation $Al_{15}(Fe,Mg)_3Si_2$ and $Al_4Cu_2Mg_8Si_7$ phases is a common practice for the strengthening of the alloy, since the formation of needle-like AlFeSi phase can be minimized [68]. However, the $Al_4Cu_2Mg_8Si_7$ phase has lower corrosion potential (more negative) than the α-Al matrix, leading to localized corrosion of the alloy [69], whereas $Al_{15}(Fe,Mg)_3Si_2$ is cathodic relative to the Al matrix. These results are consistent with the scanning Kelvin probe force microscopic (SKPFM) results of A356 cast alloy by Arrabal *et al*. [71] reporting the potential difference of various precipitates relative to the α-Al

matrix. This included coarse flakes of Si, platelets β-AlFeSi, Chinese script α-AlFeSiMg with a potential difference of 300-320 mV, 380-420 mV, and 190-230 mV, respectively, relative to the α-Al matrix [70]. In contrast, a negative potential difference was reported for the Mg-rich intermetallic (*e.g.* Mg_2Si), confirming its anodic behavior relative to the aluminum matrix [70]. The reported potential differences are adequate to advance micro-galvanic corrosion along the Al/precipitates interfaces. However, Jain [72] reported a much lower conductivity for Si than the Fe-containing intermetallics. Therefore, the resulting corrosion damage at the interface of α-Al/Si should be less detrimental than that of α-Al/Fe-containing phases.

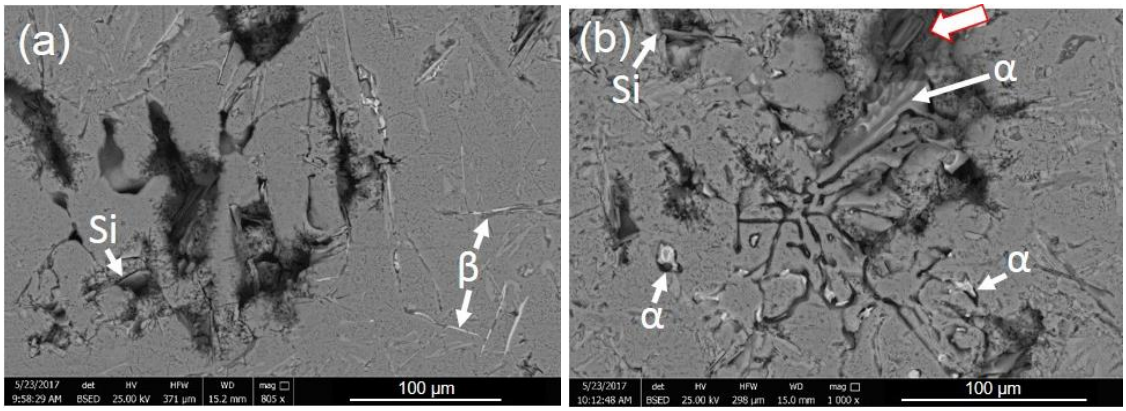

Figure 2-11: SEM images of the A360.1 cast alloy surface after the potentiodynamic test and removing the corrosion products.

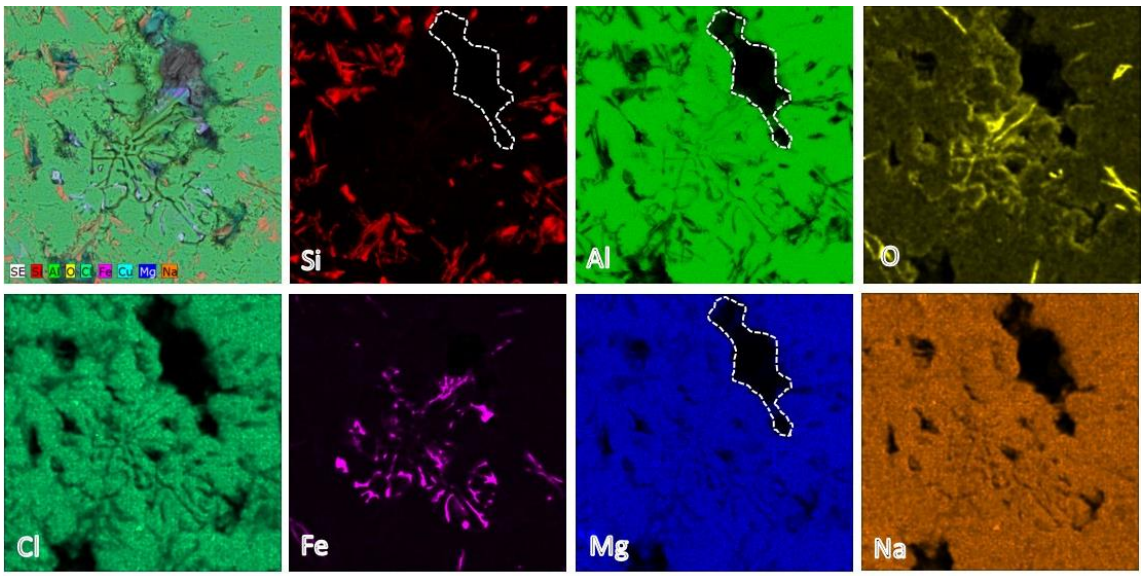

Figure 2-12: SEM-EDX concentration maps taken from the A360.1 cast alloy microstructure after removing the corrosion products indicating maps of Si, Al, O, Cl, Fe, Mg, and Na.

Figure 2-13 shows the SEM images of the as-ground DMLS produced sample after potentiodynamic polarization testing followed by removing the corrosion products. This figure revealed selective corrosion attack along the melt pool boundaries. The EDX concentration maps of the surface (Figure 2-14) confirmed an enrichment of silicon and oxygen along the melt pool borders, where coarsening of Si phase into idiomorphic particles was detected (shown in Figure 2-5). The higher concentration of Si particles as a separate phase and not in a solid-solution form incites the micro-galvanic corrosion of anodic α-Al matrix along the melt pool boundaries. However, the severity of the corrosion attack is not as significant as the cast A360.1 alloy surface.

It is worth noting that the as-printed DMLS samples revealed negligible corrosion, and as a result, no difference was observed on the sample before and after removing corrosion products.

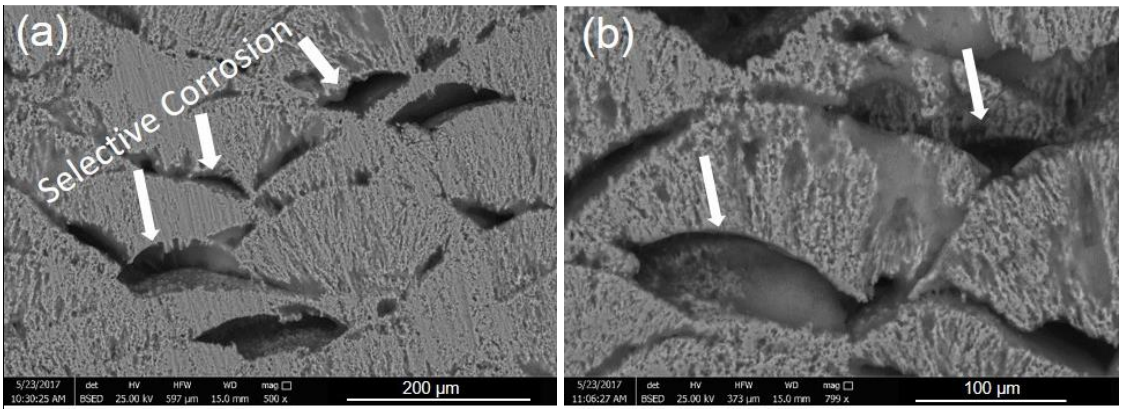

Figure 2-13: SEM images of the as-ground DMLS-AlSi10Mg_200C alloy surface after the potentiodynamic test and removing the corrosion products.

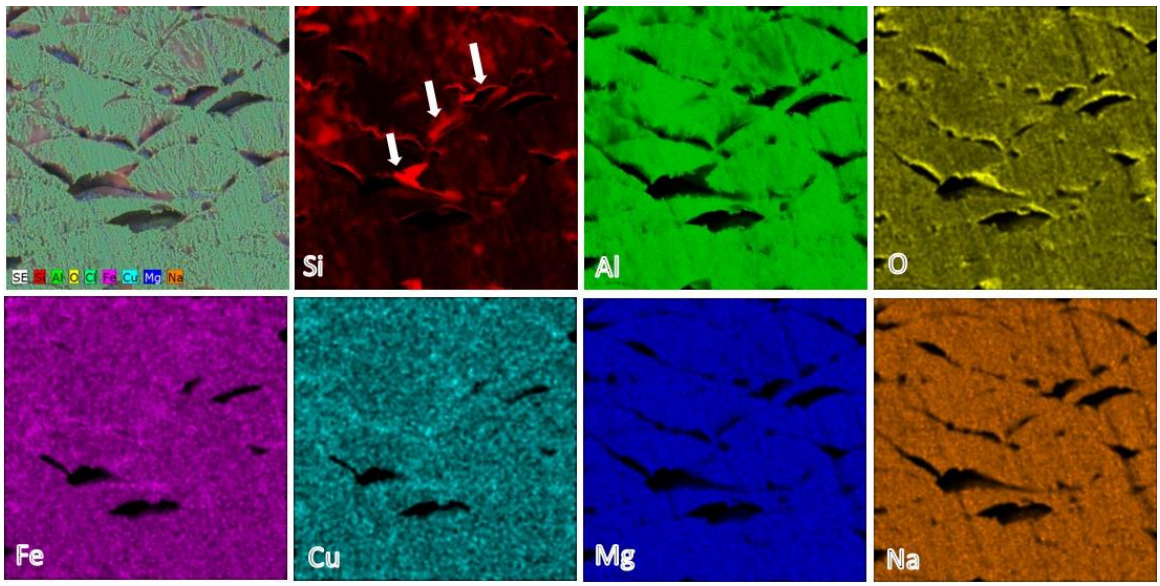

Figure 2-14: SEM-EDX concentration maps taken from the as-ground DMLS-AlSi10Mg_200C microstructure after removing the corrosion products indicating maps of Si, Al, O, Fe, Cu, Mg, and Na.

Electrochemical Impedance Spectroscopy Results

To investigate the integrity of the protective passive layer on the DMLS-AlSi10Mg_200C alloy with different surface finishes *versus* the as-ground A360.1 cast alloy, EIS tests were conducted on all samples after 1 h of immersion time in aerated 3.5 wt.% NaCl solution. The impedance spectra, including Bode and Nyquist plots are presented in Figure 2-15. The impedance response of all the samples represents typical localized corrosion behavior of Al alloys [73]. After 1 h of immersion time, the as-printed surfaces showed the highest resistance with more than one order of magnitude higher values of |Z| than the cast alloy or the ground DMLS-AlSi10Mg_200C sample, confirming a slow kinetic for the corrosion

reactions. This higher impedance of the as-printed sample is consistent with the observed corrosion behavior of the samples during potentiodynamic polarization testing (Figure 2-9), indicating the lowest corrosion current density and corrosion rate for the as-printed sample. It also confirms the existence of a more protective passive film on the as-printed DMLS surface, both in terms of thickness and density, leading to the improved film's resistivity towards the diffusion of aggressive ions, through the passive layer [74]. The observed lower values of the impedance of the ground DMLS sample at lower frequencies is also in agreement with the active-like behavior of the as-ground DMLS surface, as evidenced from the potentiodynamic polarization results in Figure 2-9.

As shown in Figure 2-15b, there is a remarkable difference between the Nyquist plots of the as-printed DMLS-AlSi10Mg_200C and the ground A360.1 cast alloy. The diameter of the capacitive arc for the as-printed DMLS-AlSi10Mg_200C has decreased considerably after grinding off the partially melted powders from the surface. Still, the DMLS-AlSi10Mg ground surface demonstrated a larger capacitive arc than that of the cast A360.1 alloy. Therefore, the DMLS-AlSi10Mg as-printed surface indicated an improved corrosion resistance compared with that of the ground one or the cast surface. This corresponds to the nature of the formed passive film on the surface, indicating the presence of more dense and protective passive layer on the as-printed surface, consistent with the results from the Bode plots (Figure 2-15a) and potentiodynamic polarization results (Figure 2-9).

Comparing the capacitive arc of the as-ground DMLS surface to that of the as-ground cast alloy indicates a larger capacitive arc for the DMLS alloy, which is associated with

the large areas of Si and other IMCs on the surface of the cast sample that form galvanic couples with the surrounding α-Al matrix.

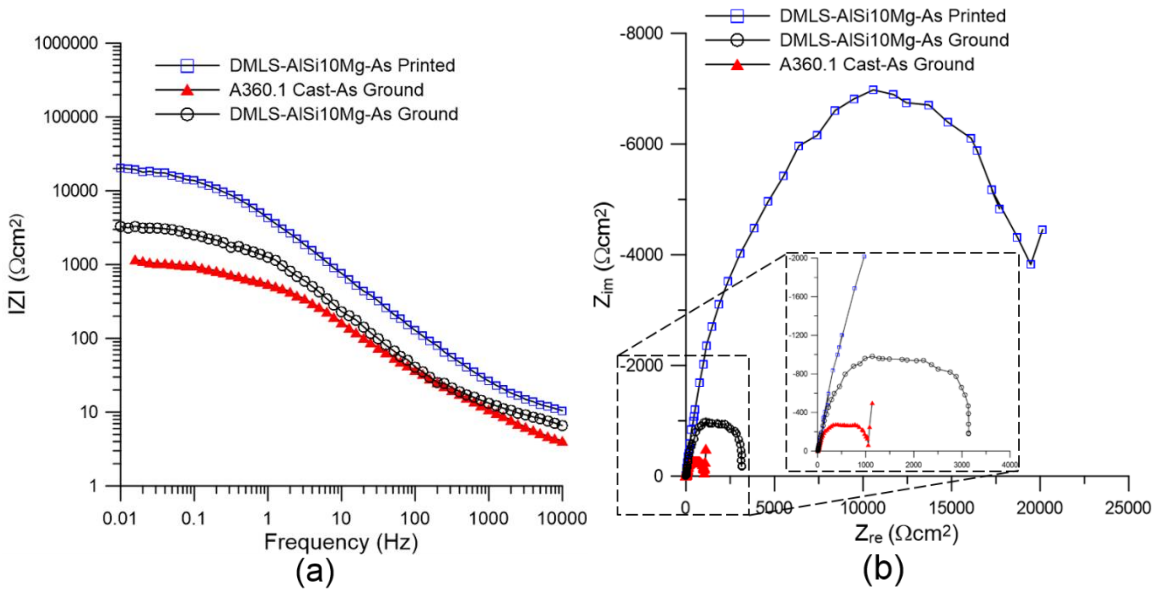

Figure 2-15: EIS spectra, (a) Z modulus and Nyquist plot of DMLS-AlSi10Mg_200C and A360.1 cast samples in 3.5 wt.% NaCl solution for the different surface finishes.

2.5 Discussion

The corrosion resistance of the DMLS-AlSi10Mg_200C alloy was found to be superior to its cast counterpart (A360.1 cast alloy) and also dependent on its surface finish. In addition, the as-printed DMLS samples showed a better corrosion resistance than the as-ground ones. The localized corrosion of the A360.1 alloy primarily occurred at the interface between iron-containing IMCs, *i.e.* $Al_{15}(Fe,Mg)_3Si_2$ and Al_5FeSi, and the α-Al matrix with less

intense corrosion between Si particles and the Al-matrix, dictated by the potential difference as well as the conductivity of the precipitates relative to the α-Al matrix. These results are in contrast with the results reported by Revilla *et al*. [21], in which a similar value of corrosion potential was reported for a SLM-AlSi10Mg alloy and AA4420 cast Al alloy with analogous composition despite their significantly different microstructure and phase distribution. The authors [21] ascribed this behavior to the comparable chemical composition of the alloys. However, all the individual micro-constituents and microstructural features are known to contribute to the final corrosion potential of the component, as evidenced in the current study. Cabrini *et al*. [19] also reported different corrosion potentials for DMLS-AlSi10Mg after various post heat treatment processes even though the chemical composition remains constant.

The obtained microstructure from the DMLS process was found to be extremely fine characterized by the cellular dendritic structure of α-Al matrix containing Si particles along the interdendritic regions. The fast solidification of the melt pool during the DMLS process remains the Al matrix saturated by the alloying elements, *i.e*. Fe, Mg, Cu, *etc*., and the remaining silicon segregates along the interdendritic regions. In the HAZ between two adjacent melt pools, the eutectic Si precipitates coarsen and turn into idiomorphic crystals as a result of high temperature experienced during the process from the adjacent MP, leading to an increase in the diffusion rate of Si in this region. The potentiodynamic polarization testing confirmed that the selective corrosion of the as-ground DMLS specimen predominantly occurred between the melt pool boundaries (the laser tracks),

where the Si network is coarsened. This is attributed to the nobility of the Si phase compared to the α-Al matrix [70]. Osório *et al*. [75] also reported that corrosion resistance of Al-Si alloy decreases by increasing the Si content. This was associated with increasing the fraction of very fine eutectic Si particle, leading to a higher corrosion rate [75]. This is in agreement with the observed preferential corrosion in the melt pool borders of the DMLS-produced sample in this study, where a higher concentration of Si present as an individual phase and not in solid solution form (see Figure 2-13 and Figure 2-14). A similar observation was reported by Cabrini *et al*. [22,24] after potentiodynamic polarization testing of DMLS-AlSi10Mg samples in diluted Harrison solution. The local Volta potential analysis results from SKPFM testing by Revilla *et al*. [21], further confirmed a greater potential difference between α-Al matrix and the Si phase in the melt pool boundaries of SLM-AlSi10Mg alloy with coarser microstructure, representing a higher driving force for galvanic corrosion.

Furthermore, the higher concentration of Fe, Cu, Mg, and Zn alloying elements in the A360.1 alloy compared to the DMLS-AlSi10Mg_200C alloy should not be neglected. In addition to the significant difference between the solidification rate of the DMLS and die-casting processes, the existing compositional discrepancy (~ 0.8 wt.% Fe, 0.6 wt.% Cu, 0.4 wt.% Zn, and 0.2 wt.% Mg) also contributes to the observed microstructural differences in these alloys, and directly influence the electrochemical properties of the alloys. Higher Fe and Cu content of the A360.1 cast alloy promotes formation of Fe and Cu containing intermetallic compounds, which causes detrimental effects on both mechanical and

corrosion properties of the cast alloy. The effect may be less detrimental at very high solidification rates (*e.g.* DMLS process), but as the solidification rate decreases (DMLS → die-casting), the alloy experiences serious loss of corrosion resistivity and mechanical properties [76]. Pius [77] reported that an increase in the Fe content of A356 cast Al alloy from 0.84 wt.% to 1.8 wt.% results in an increase in the volume fraction of intermetallic compounds from 4.2% to 8.6%. Although, Cu addition generally improves mechanical properties of Al-Si-Mg alloys, *i.e.* ultimate tensile strength and hardness, which results in improved machinability of the alloy [78], it can reduce corrosion and stress corrosion resistivity of the alloy [78]. Therefore, lower concentration of Fe and Cu in the DMLS-AlSi10Mg_200C alloy also contributes to the improved corrosion performance of the alloy relative to that of the A360.1 cast alloy. The low content of Zn element in A360.1 cast alloy is only an acceptable impurity element and it does not impact neither the mechanical properties nor the corrosion performance of the alloy [78]. The slightly higher Mg concentration in A360.1 cast alloy than the DMLS alloy can provide improved strengthening and work hardening characteristics to the alloy. It can also enhance corrosion resistivity of the alloy by minimizing the formation of detrimental AlFeSi intermetallic compound [64]; however, the impact was not significant enough to dictate the general corrosion behavior of the cast alloy.

In the case of as-printed DMLS produced specimen, the impedance response of the samples (Figure 2-15) confirmed the existence of a more protective passive layer on the surface as evidenced by its high impedance values at low frequencies than that of the

ground DMLS surface, which is in accordance with the potentiodynamic polarization test results. As shown in Figure 2-3, the as-printed sample is covered by the accumulated partially melted powder particles. The surfaces of the powders are heavily oxidized as evidenced by the SEM-EDX concentration maps of oxygen from the surface of the as-printed sample relative to that of the as-ground DMLS produced surface (Figure 2-16). Similar observation for the AlSi10Mg gas atomized powders used for DMLS process was noted by Olakanmi [79]. The stable passive layer on these particles covers the whole surface and protects the rest of the materials from further oxidation, as evidenced by the wide passive range of the as-printed DMLS sample shown in Figure 2-9. The grinding of the as-printed DMLS sample removes the partially melted powder particles, which acted as a protective barrier against corrosion on the surface, leaving the as-ground surface containing highly active cathodic sites (melt pool boundaries) directly in contact with the corrosive environment. Once the active cathodic sites on the surface of the DMLS sample or cast sample are exposed to the electrolyte, active nucleation of pits around the Si or other IMCs is initiated. This describes the low impedance of both the as-ground DMLS and cast alloys. Therefore, not only the post-grinding of the as-printed DMLS manufactured components is laborious and very difficult over complex shapes, but also it degrades corrosion property of the sample at the early stage of immersion.

In addition, the microstructure of the powders, as shown in Figure 2-17 confirms a coarser dendritic structure with an average cell size of 2.7 ± 0.5 μm for the powders than that of the as-ground DMLS produced specimen (Figure 2-5). It has been reported that the

coarser dendritic structure of the Al-Si-Mg alloys tends to yield higher corrosion resistance than the finer structure with the more extensive distribution of the eutectic mixture [75]. This is another compelling evidence for higher corrosion resistivity of the as-printed DMLS produced sample than the as-ground one. Nonetheless, these results are not consistent with the results reported by Cabrini *et al*. [22] in which an improved corrosion resistance was reported for the DMLS-AlSi10Mg sample 48 h after polishing the as-printed surfaces using 0.1 µm alumina. In a similar study, Leon and Aghion [25] reported a reduced corrosion resistance for the as-printed SLM-AlSi10Mg alloy compared to its polished counterpart. The authors in both works [22,25] associated this behavior with the surface porosities, roughness, and formation of less protective oxide layer on the sample during the DMLS process. However, an opposite behavior was detected in the current study. To clarify this, two major differences can be noted between the tested samples in this study compared with those in previous studies [22,25]. The first difference is that in the current study, electrochemical testing was performed 1-2 h after grinding the surfaces, compared to 48 hr remaining of the polished samples in air in the previous study prior to the corrosion testing [22]. However, this should not contribute to the observed differences in corrosion behaviors of the samples, since it was reported that formation of Alumina (Al_2O_3) on the surface of fresh as-ground/as-polished Al is a rapid thermodynamic process at room temperature under ambient pressure, which grows rapidly to a limiting thickness of 32 Å after 10 min of exposure [80]. Longer exposure time was reported to lead to very slow growth of the oxide layer thickness (40 Å after three months) [80]. Therefore, the thickness

of the formed protective oxide layer on the DMLS samples was approximately consistent in both studies and cannot contribute to the observed differences in their corrosion resistance. The other distinction is the obtained surface roughness from 600 SiC grit finish in this study *versus* 0.1 µm alumina polished surfaces in the previous study [22]. Clearly, the as-ground surface finish has a higher surface roughness than the as-polished surface. This simply results in an increased contact area of solid-liquid interface on the as-ground sample during electro-chemical testing and leads to an enhanced corrosion current density and corrosion rate.

It is worth noting that the polished-finish printed surfaces were not investigated in this study, primarily due to the fact that polishing of large printed industrial components with complex geometries to a mirror finish surface is impractical.

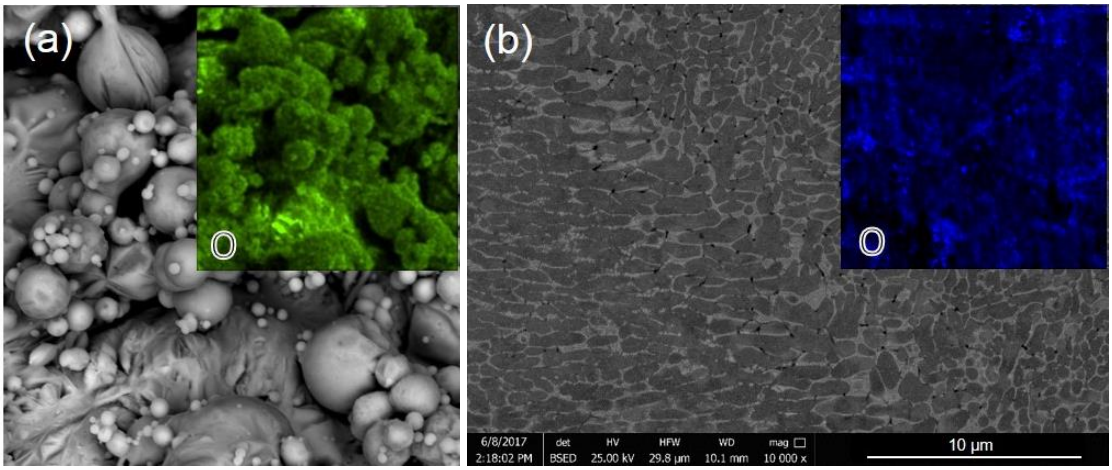

Figure 2-16: The SEM micrographs of (a) the as-printed and (b) as-polished AlSi10Mg_200C samples. The enclosed images show the oxygen concentration maps taken from the surface of each sample.

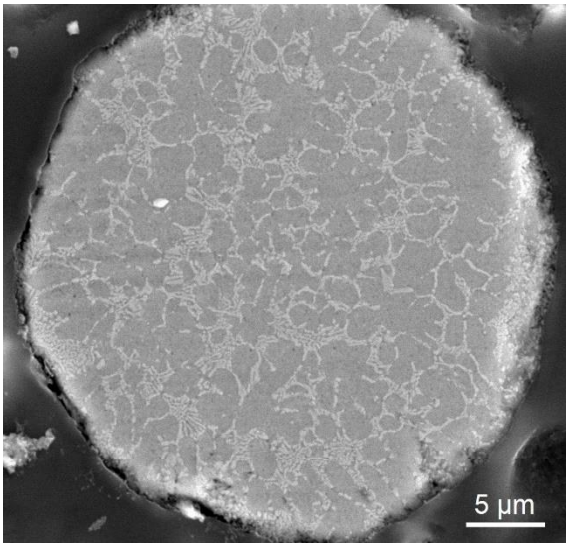

Figure 2-17: Cross-sectional SEM micrographs of AlSi10Mg_200C powder used in this study.

2.6 Conclusions

In this study, corrosion behavior and microstructure of AlSi10Mg_200C alloy produced by DMLS *versus* its cast counterpart, die cast A360.1 Al alloy, were investigated using potentiodynamic polarization testing and electrochemical impedance spectroscopy. The impact of surface grinding on the sensitivity of this alloy to corrosion attack in the presence of chloride was also studied. The results of this study contributed to the following conclusions:

1. The microstructure of DMLS-AlSi10Mg_200C sample was found to be entirely different from its heavily precipitated A360.1 die cast counterpart characterized by a

cellular dendritic structure composed of dendrites of the α-Al solid solution and the interdendritic Si particles.

2. Corrosion of the cast alloy revealed severe localized corrosion of the Al matrix in the periphery of the Fe containing IMC and Si flakes as well as corrosion of the Mg-containing IMC.
3. As-printed and as-ground DMLS-AlSi10Mg_200C samples showed significantly better corrosion resistant, *i.e*. higher corrosion potential accompanied by lower corrosion current densities, to the chloride containing environment than A360.1 cast alloy. This was mainly attributed to the fine microstructure, uniform distribution of fine Si particles without the formation of any intermetallic resulted from extremely rapid cooling and solidification rate during DMLS process, and also the lower Fe and Cu content of the DMLS alloy than its cast counterpart.
4. Selective corrosion (galvanic corrosion) of the α-Al matrix in the melt pool boundaries of the DMLS produced sample, where Si particles separate as idiomorphic crystals, was observed.
5. The corrosion performance of the DMLS-AlSi10Mg_200C was also found to be dependent on its surface finishing. The improved corrosion resistance of the as-printed DMLS sample compared to the as-ground one was mainly attributed to the coverage of the surface by the accumulated partially melted, heavily oxidized powder particles with coarse dendritic structure, which contributes to the formation of a more protective passive film on its surface, as evidenced by the EIS results.

Chapter 3

Effects of Surface Finishing Procedure on Corrosion Behavior of DMLS-AlSi10Mg_200C Alloy *vs* Die Cast A360.1 Aluminum[2]

3.1 ABSTRACT

In this study, the impact of surface finishing procedure on corrosion resistance of AlSi10Mg_200C alloy manufactured through direct metal laser sintering (DMLS) *versus* its die cast counterpart was investigated. The as-printed DMLS-AlSi10Mg_200C and as-cast A360.1 alloys were subjected to various surface finishing processes including grinding and sandblasting. The corrosion performance of the surfaces was then evaluated using potentiodynamic polarization test and electrochemical impedance spectroscopy in aerated 3.5wt.% NaCl solution. The results highlighted better corrosion resistance of DMLS-AlSi10Mg_200C than its cast counterpart with similar surface finish. The grinding of both as-printed DMLS and as-cast samples was found to initially deteriorate the corrosion performance of the surface by exposing cathodic sites to the electrolyte. However, for longer immersion times and after complete repassivation of the surface, the ground surface showed the highest resistance to the selective attack. Sandblasting process was found to have a detrimental effect on corrosion resistance of both alloys.

---

[2] P. Fathi, *et al*., *JOM (Journal of The Minerals, Metals & Materials Society)* (Impact Factor: 2.471), 2019, (5), pp. 1748-1759 [89].
P. Fathi, *et al*., *International Conference on Aluminum Alloys (ICAA16*), June 17-21, 2018, Montreal.

3.2 Introduction

Direct Metal Laser Sintering (DMLS), also known as Selective Laser Melting (SLM) [1], or Laser Metal Fusion (LMF) [3], is an additive manufacturing process that utilizes a precise, high-power laser to micro-join powdered metals and alloys layer by layer to form almost fully dense and functional components in three dimensions from 3D computer-aided design data. Complex geometries not possible with conventional manufacturing processes can be readily manufactured with high accuracy using the DMLS process with no need for time-consuming tooling.

The use of light-weight, high-strength Al alloys in modern manufacturing has drastically increased during the last two decades. Among these alloys, Al-Si-Mg alloys are widely used in transportation applications, particularly for the automotive, marine, and aerospace industries, because of their high strength and stiffness-to-weight ratio, low density, and good corrosion resistance [7]. In addition, having excellent fluidity, cast ability, and recycling potentials have made these alloys great candidates for additive manufacturing through DMLS process [39]. In particular, Al-Si10-Mg alloy is extensively fabricated using the DMLS process primarily due to its reduced coefficient of thermal expansion, leading to low solidification shrinkage and reduced susceptibility to hot cracking during solidification. So far, the major research on this alloy has been focused on the evolution of microstructure and mechanical properties of the alloy processed through various DMLS processing parameters, where very little work has been done to understand the corrosion behavior of the DMLS-AlSi10Mg alloy.

The impact of microstructure on the corrosion resistivity of additively manufactured AlSi10Mg alloy has been researched in a few recent studies. Cabrini *et al*. [19] investigated the impact of different post-heat treatments, *i.e*., stress relieving and high temperature annealing followed by water quenching, on corrosion behavior of DMLS-AlSi10Mg alloy. The authors demonstrated that the low temperature stress relieving at 537 K does not affect the susceptibility of the alloy to the selective attack in Harrison solution. However, high temperature annealing at 823 K was reported to promote localized corrosion attack resulted from accelerated galvanic coupling between the coarse Si particles and surrounding Al matrix. In a recent study, Fathi *et al*. [32] discussed the corrosion behavior and microstructure of AlSi10Mg_200C alloy manufactured through DMLS *vs* its conventional cast alloy with similar composition (A360.1), and reported a noticeably improved corrosion resistance to a chloride containing environment for the DMLS alloy than A360.1 cast alloy, which was attributed to the fine microstructure and uniform distribution of Si particles with no evidence of formation of strongly cathodic intermetallic compounds (IMCs) in the DMLS microstructure [32]. Cabrini *et al*. [22] have also evaluated the effect of building direction combined with different surface finishing, including mechanical polishing and shot peening, on corrosion resistivity of DMLS-AlSi10Mg alloy. An improved corrosion resistance was reported for the polished as well as smooth shot-peened surfaces relative to that of the rough as-printed ones. Additionally, the authors reported a reduced corrosion resistance of the surfaces parallel to the building direction, which was attributed to the higher density of the melt pool borders containing a higher concentration of coarser Si

particles [22]. The local Volta potential analysis results taken from the melt pool borders, reported by Revilla *et al*. [21], confirmed a higher potential difference between the Si phase and the α-Al matrix in the border regions with coarser structure, representing a greater driving force for galvanic corrosion.

In a similar study, Leon and Aghion [25] explored the effect of surface roughness on both general corrosion and corrosion fatigue behaviors of additively manufactured AlSi10Mg processed through SLM, by comparing the as-printed surfaces with the polished ones. An improved corrosion resistance and a higher low cycle corrosion fatigue life span were reported for the polished surfaces over the as-printed ones, associated with the increased surface roughness of the as-printed sample [25]. Despite the above mentioned two studies by Cabrini *et al*. [22] and Leon and Aghion [25] were focused on the impact of surface quality on the corrosion behavior of additively manufactured AlSi10Mg, yet, a comprehensive study is needed to understand the influence of commonly used surface finishing procedures, such as post grinding or sandblasting, on the corrosion behavior of additively manufactured AlSi10Mg alloy. There is no previous investigation on the corrosion performance of DMLS-AlSi10Mg subjected to the post-grinding or sandblasting process.

This study is aimed to investigate the impact of surface finishing on corrosion performance of AlSi10Mg_200C alloy manufactured through DMLS *versus* its cast counterpart, A360.1 aluminum. Various surface finishing processes, including grinding and sandblasting, were studied using potentiodynamic polarization testing and electro-

chemical impedance spectroscopy (EIS). The results of this study will help to understand the dominating factors (surface morphology *vs* microstructure) in controlling the electrochemical behavior of the DMLS-AlSi10Mg material in the marine environment.

3.3 Materials and methods

Materials

The tests were carried out on 10 × 10 × 10 mm cubes (see Figure 3-1a) fabricated through DMLS process from a gas atomized commercial AlSi10Mg_200C powder with average particle size of 8.8 ± 7 µm from EOS, containing 9–11 wt.% Si, 0.2–0.45 wt.% Mg, less than 0.55 wt.% Fe and Mn, Bal. Al, using an EOS-M290 metal 3D printer machine. The DMLS was executed in an argon atmosphere (oxygen content of 0.1%) and elevated building platform temperature of 200°C, to minimize the oxidation and the internal stresses, respectively, during the manufacturing process. Other processing parameters include laser power of 370 W, scanning speed of 1300 mm/s, hatching distance of 190 µm, and powder layer thickness of 30 µm using strip scanning strategy with 67° laser beam rotation between successive layers.

The as-fabricated samples provided the as-printed surface condition. Some of the as-printed samples were subjected to mechanical grinding using 600 grit SiC abrasive paper. This provided the ground surface finish samples. The rest were subjected to sandblasting using a Vaniman micro-abrasive sandblaster, to remove sticky partially melted powders from the surface (sandblasted samples). For this study, 100 µm size aluminum oxide

abrasive blasting media was chosen as the abrasive particle. With the distance of 10 mm between the surface and the blasting nozzle, the surfaces were blasted perpendicularly under the pressure of 100 psi. Further, the same size cubes were sectioned from a die cast A360.1 Al ingot (AlSi10Mg cast alloy counterpart) composed of 9–10 wt.% Si, 0.4–0.6 wt.% Mg, 1.3 wt.% Fe, 0.35 wt.% Mn, 0.5 wt.% Zn, 0.6 wt.% Cu, Bal. Al. To fabricate ground and sandblasted surface conditions on the cast samples, similar mechanical grinding and sandblasting procedures to those of the DMLS samples were applied for the cast samples. All the samples were ultrasonically cleaned in acetone prior to the electrochemical tests.

Microscopic characterization

For microstructural and compositional analysis of the samples, an FEI-MLA-650F scanning electron microscope was used. To prepare the samples for microscopic analysis, the samples were mounted in an epoxy resin followed by standard grinding and polishing sample preparation procedures for Al alloys. The polished specimens were then etched using Keller's reagent.

Electrochemical measurements

Potentiodynamic polarization measurements of the samples with different surface finishes were carried out using an IVIUM-CompactStat™ computer-controlled Potentiostat

connected to a three-electrode cell setup in a multiport glass cell at atmospheric pressure based on the ASTM G5-94 standard [53]. The three-electrode cell configuration includes a graphite rod as the counter electrode (CE), a saturated Ag/AgCl as the reference electrode (RE), and the sample as the working electrode. The test electrolyte was aerated 3.5 wt.% NaCl solution to simulate seawater corrosion environment. The corrosion cell was placed in a temperature-controlled water bath to control the solution temperature at 25±0.5 °C. After immersion in the solution, the open circuit potential (OCP) was monitored for 1 hr for stabilization before the potentiodynamic polarization test. The scans were performed from −0.3 V to +0.3 V *versus* the OCP with a scanning rate of 0.125 mV/s. Repeatability of the results was measured by testing at least three samples. To study the corrosion morphology resulted from the potentiodynamic polarization test, the formed corrosion products on the surface were removed by immersing the samples in a concentrated HNO_3 solution (15.8 N) in an ultrasonic bath for 15 min [54]. EIS measurements were also conducted for immersion times ranging from initial immersion to 96 hr, every 24 hr in aerated 3.5 wt.% NaCl solution at 25 °C, with the amplitude perturbation of ±10 mV (sinusoidal potential signal) with respect to the OCP and a frequency range of 10 kHz to 10 mHz with ten points per decade. The impedance spectra were analyzed using the IVIUMSOFT electrochemical analysis software.

3.4 Results and Discussion

Surface morphology and microstructure

Figure 3-1a shows the as-printed DMLS-AlSi10Mg_200C cubic samples used in this study. The SEM micrographs from the surface of the DMLS-AlSi10Mg_200C at various surface conditions are presented in Figs. 1b–d. The as-printed surface (Figure 3-1b) demonstrates a high degree of surface irregularities resulted from the attachment of partially melted powder metal particles to the surface during the DMLS process creating a superficial roughness on the surface in as-printed condition.Figure 3-1c and Figure 3-1e show the surface morphology of the sandblasted DMLS-AlSi10Mg_200C and A360.1 cast alloy, respectively. Sandblasting eliminates the partially melted particles from the surface. Meanwhile, it introduces randomly deformed areas on the surface generated as the aluminum oxide blasting media impacts the surface. Non-regular peaks and valleys are clearly visible on the sandblasted surfaces. As shown in Figure 3-1d, similar to sandblasting, the mechanical grinding of the surface using 600 grit SiC abrasive paper has also reduced the as-printed surface roughness. The ground surface is characterized by one direction oriented trenches formed during surface preparation. The energy dispersive X-ray (EDX) analysis results also confirmed that surface chemical compositions of both DMLS and cast samples are independent from their surface finish and were found to be similar for all the DMLS samples (10.80±0.20 wt.% Si, 0.35±0.05 wt.% Mg, 0.50±0.04 wt.% Fe, Bal. Al) and all the cast samples (9.82±0.35 wt.% Si, 0.50±0.10 wt.% Mg,

1.02±0.15 wt.% Fe, 0.30±0.06 wt.% Mn, 0.45±0.08 wt.% Zn, 0.38±0.09 wt.% Cu, Bal. Al).

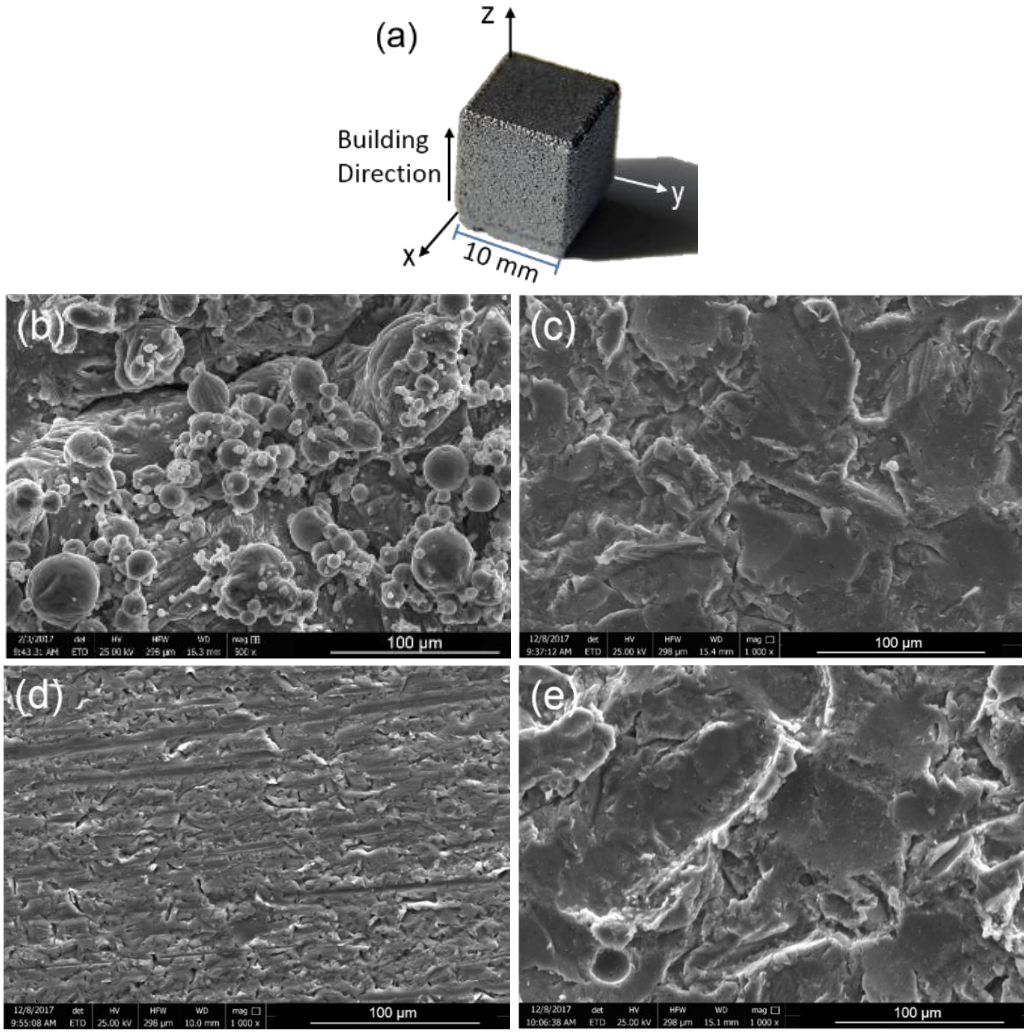

Figure 3-1: (a) DMLS-AlSi10Mg_200C cubes used in this study. SEM images of DMLS-AlSi10Mg_200C surface in (b) as-printed, (c) sandblasted, and (d) ground conditions. Sandblasted surface of A360.1 cast alloy is shown in (e).

Figure 3-2a shows the SEM micrographs of the side view of the DMLS-AlSi10Mg_200C (the y-z plane in Figure 3-1a). All electrochemical measurements in this study were only conducted on the y-z plane since Cabrini *et al*. [22] reported higher susceptibility of this plane to selective corrosion attack in a chloride containing environment than the x-y plane (Figure 3-1a), primarily due to existence of high density of melt pool boundaries on this plane. The microstructure of the DMLS alloy (Figure 3-2a) was characterized by very fine cellular dendritic structure (~ 0.5–2 μm) with non-equilibrium directional solidification features composed of supersaturated α-Al cellular grains and a continuous network of Si phase formed at the intercellular region (confirmed by the EDX-maps shown in Figure 3-2a), resulted from very high cooling rates during solidification. As shown inFigure 3-2a, the cell size changes over the melt pool (MP) from the melt pool center with finer structure (MP-Fine) towards the border with coarser cellular structure (MP-Coarse). A very thin band of heat affected zone (HAZ) (~ 5 μm wide), characterized by broken intercellular network resulted from coarsening of Si phase into idiomorphic crystals, was also detected around each melt pool. This non-uniform cell structure is attributed to the thermal gradient generated by the moving heat source of the DMLS process.

The SEM micrograph of the A360.1 cast alloy and its corresponding EDX concentration maps (Figure 3-2b) showed a conventional casting microstructure, containing α-Al matrix, coarse flakes of Si, and several intermetallic compounds including β-AlFeSi platelets, α-AlFeSiMg with a Chinese script morphology, and AlMgSiCu with

honeycomb structure. An extensive microstructural analysis of the DMLS-AlSi10Mg_200C *vs* A360.1 cast alloy was described in a recent work by Fathi *et al*. [32], confirming that the unique solidification behavior of material during the DMLS process promotes the formation of extremely fine cellular structure.

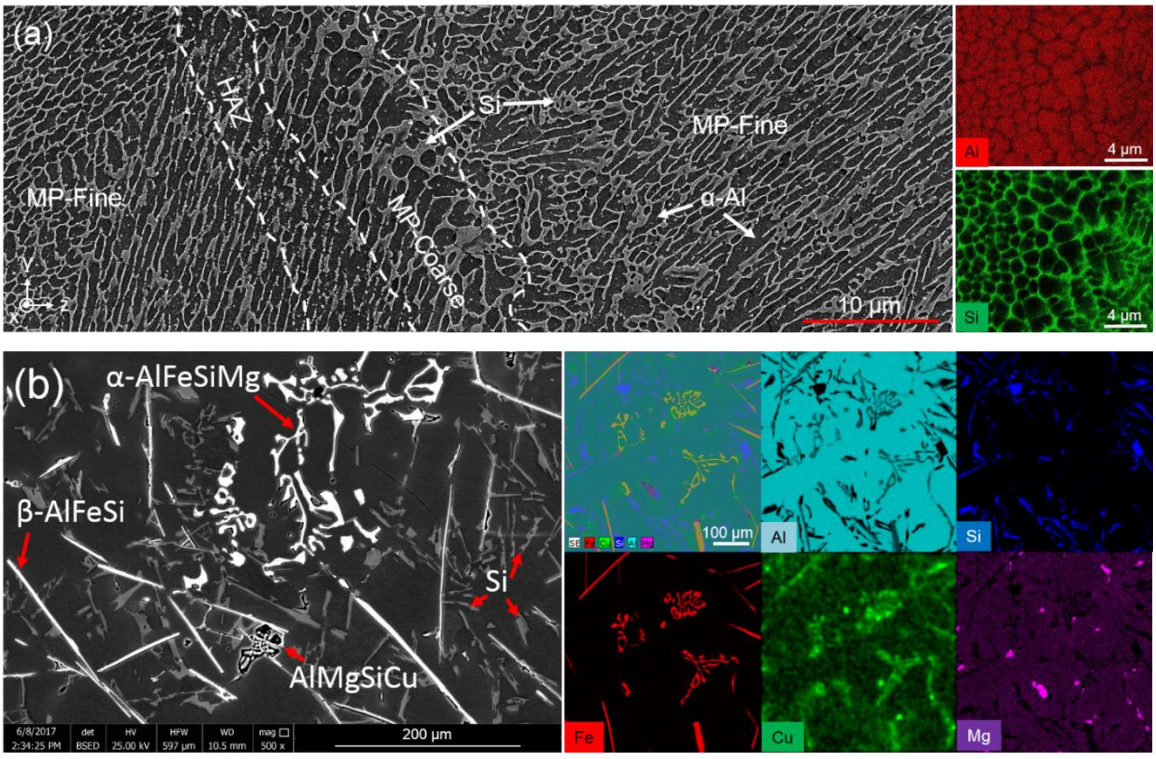

Figure 3-2: The SEM micrographs and EDX concentration maps taken from (a) DMLS-AlSi10Mg_200C and (b) A360.1 cast Al alloy.

Potentiodynamic results

Figure 3-3 shows the potentiodynamic polarization behavior of all the specimens with various surface finishing. To allow the stabilization of the OCP, measurements were started 1 hr after immersion in aerated 3.5 wt.% NaCl solution. The extracted data from the potentiodynamic polarization measurements, including the corrosion potentials, polarizations resistance, anodic and cathodic slopes, and corrosion current densities are listed in Table 3-1. The anodic branch of the Tafel plots shown in Figure 3-3 demonstrates pitting corrosion characteristics for the DMLS samples, where a slight increase in the applied potential induces a rapid increase in the anodic current, meaning $E_{Pit.} \cong E_{Corr.}$. Therefore, surface pitting can be freely initiated at the corrosion potential for the DMLS samples. This active behavior of the surface is more pronounced for the ground and sandblasted DMLS-AlSi10Mg_200C samples. For the as-printed sample, a very narrow passive region above the corrosion potential (between $E_{corr.}$ and $E_{corr.}$ + 0.05 $V_{Ag/AgCl}$) was detected for some of the tested samples (shown in Figure 3-3), that can be neglected since the measured standard deviation value for the corrosion potentials for this sample (±0.12 $V_{Ag/AgCl}$) was greater than the observed narrow passive window (0.05 $V_{Ag/AgCl}$). Similar active-like behavior was also observed by Cabrini *et al*. [22] for the as-printed additively manufactured AlSi10Mg alloy. On the contrary, Cabrini *et al*. [22] reported a wide passive region for the polished DMLS-AlSi10Mg surfaces. The corrosion potential of the DMLS-ground surface was only slightly higher (~ 46-64 mV) than the other surface finishes. These

minor differences in corrosion potentials and pitting potentials is an indication of similar corrosion mechanisms for all DMLS samples with different surface finishes.

The polarization curves of the cast samples show that the corrosion potential has shifted to more active values and is characterized by a wider passive region, confirming a low likelihood of pit nucleation. For both sandblasted and ground A360.1 cast alloy, the passive film breakdown potential (E_{pit}) remained approximately stable (~ 0.705 $V_{Ag/AgCl}$), suggesting that the corrosion layer composition stayed unchanged. On the other hand, the pitting potential of the samples varies from the DMLS samples to the cast alloy, an indication for having passive films with different chemical compositions, since the pitting potential is only dictated by the corrosion layer composition, as reported by Szklarska-Smialowska [47].

As the surface condition of the DMLS samples varies from the as-printed surface to the sandblasted one and from the sandblasted to the ground surface, the corrosion current density increases (see Table 3-1). Therefore, surface grinding of the as-printed DMLS-AlSi10Mg_200C led to a loss of corrosion resistance in just immersed condition.

As a general trend, the DMLS fabricated samples showed better corrosion resistance with lower corrosion current density than those of the cast samples with similar surface finishes.

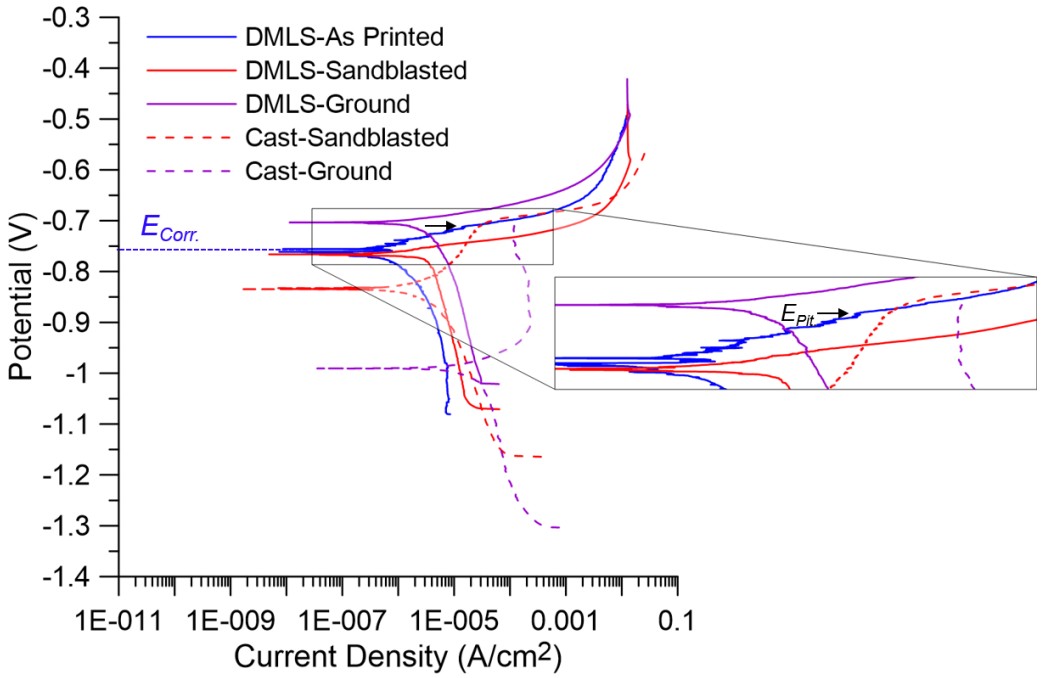

Figure 3-3: Potentiodynamic polarization curves for the as-printed, ground, sandblasted AlSi10Mg_200C, and sandblasted and ground A360.1 cast alloy in aerated 3.5 wt.% NaCl environment.

The surface morphology of the samples after potentiodynamic polarization testing followed by the corrosion products removal is shown in Figure 3-4. The as-printed DMLS-AlSi10Mg surface, which demonstrated the minimum corrosion current density, confirmed a trivial attack on the surface (Figure 3-4a) with no indication of pitting corrosion. Although the sandblasting created a smoother surface finish than the as-printed surface and eliminated the surface porosities (compare Figure 3-1b with Figure 3-1c), it has introduced a superficial roughness. As shown in Figure 3-4b andFigure 3-4d, some localized corrosion attack and surface pitting were noticed on both sandblasted surfaces, but not as severe as

those of the ground surfaces (Figure 3-4c and Figure 3-4e). The DMLS ground surface (Figure 3-4c and Figure 3-4f) experienced a selective attack along the heat affected zone (boundaries of the melt pools), where enrichment of the Si phase (shown by the white arrows on the Si concentration map in Figure 3-4f) and coarsening and breakage of the Si network into an idiomorphic phase were detected (see Figure 3-2a). Fathi *et al*. [32] attributed this behavior to the nobility of the Si relative to the α-Al matrix, which triggers the micro-galvanic corrosion of anodic α-Al matrix along the heat affected zones. The corroded surface of the ground A360.1 cast alloy (Figure 3-4e and Figure 3-4g) evidenced severe corrosion and large pitting of the α-Al matrix at the periphery of the cathodic Si particles and other IMCs shown in Fig. 2b. A detailed study of the corrosion morphology of A360.1 cast alloy is reported in a previous work by Fathi *et al*. [32].

Table 3-1: Potentiodynamic polarization parameters collected from just immersed DMLS-AlSi10Mg_200C and A360.1 Al alloys in aerated 3.5 wt.% NaCl solution

Surface finishing	Corrosion potential ($V_{Ag/AgCl}$)	Polarization resistance (Ω)	Anodic slope (V/dec)	Cathodic slope (V/dec)	Corrosion current density (A/cm^2)
DMLS-As Printed	-0.770 ± 0.120	2955 ± 470.850	0.034 ± 0.007	0.192 ± 0.037	1.146 ± 0.172 $\times 10^{-6}$
DMLS-Sandblasted	-0.752 ± 0.130	438 ± 40.720	0.012 ± 0.009	0.424 ± 0.041	3.497 ± 0.420 $\times 10^{-6}$
DMLS-Ground	-0.706 ± 0.077	686.4 ± 77.231	0.029 ± 0.003	0.350 ± 0.042	4.775 ± 0.524 $\times 10^{-6}$
Cast-Sandblasted	-0.832 ± 0.095	720.3 ± 57.624	0.159 ± 0.004	0.265 ± 0.055	4.645 ± 0.670 $\times 10^{-6}$
Cast-Ground	-0.980 ± 0.078	162.9 ± 14.665	0.062 ± 0.005	0.476 ± 0.048	31.05 ± 2.640 $\times 10^{-6}$

Therefore, the corrosion morphology of the samples and the severity of the corrosion attack are in agreement with the potentiodynamic polarization results, confirming the ground surface to be highly susceptible to localized corrosion attack and the as-printed and the sandblasted surfaces to be more resistant. Fathi *et al*. [32] indicated that the improved corrosion resistivity of the as-printed surface at the initial stage of immersion is attributed to the coverage of the surface by the accumulated heavily oxidized powder particles with coarse dendritic structures that protect the surface from further oxidation.

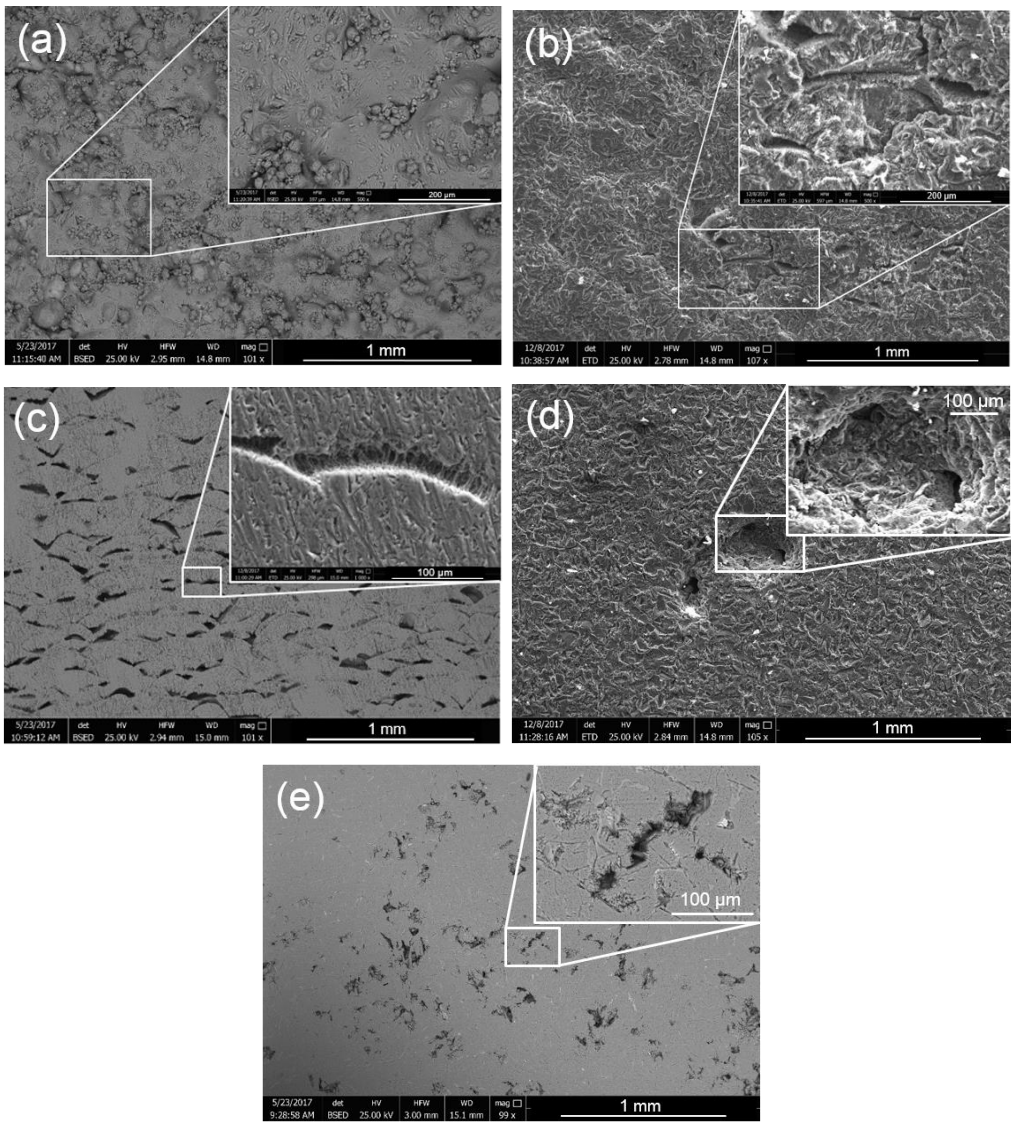
(a)
200 µm
5/23/2017 11:15:40 AM det BSED HV 25.00 kV HFW 2.95 mm WD 14.8 mm mag 101 x
1 mm
(b)
200 µm
12/8/2017 10:38:57 AM det ETD HV 25.00 kV HFW 2.78 mm WD 14.8 mm mag 107 x
1 mm
(c)
100 µm
5/23/2017 10:59:12 AM det BSED HV 25.00 kV HFW 2.94 mm WD 15.0 mm mag 101 x
1 mm
(d)
100 µm
12/8/2017 11:28:16 AM det ETD HV 25.00 kV HFW 2.84 mm WD 14.8 mm mag 105 x
1 mm
(e)
100 µm
5/23/2017 9:28:58 AM det BSED HV 25.00 kV HFW 3.00 mm WD 15.1 mm mag 99 x
1 mm

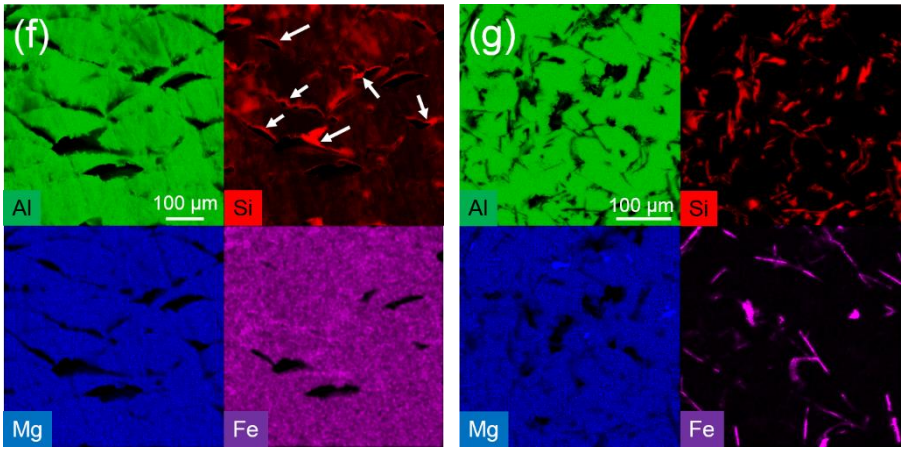

Figure 3-4: SEM micrographs after the potentiodynamic polarization test: (a) as-printed, (b) sandblasted, (c) ground DMLS-AlSi10Mg_200C surface, and (d) sandblasted, and (e) ground A360.1 cast alloy. EDX concentration maps taken from the ground (f) DMLS-AlSi10Mg and (g) A360.1 cast sample after the polarization test.

Electrochemical impedance spectroscopy results

The EIS tests were carried out to evidence the protectiveness of the passive film on all the samples after various immersion times. The impedance spectra over time are presented in Figure 3-5 for the as-printed, ground, and sandblasted DMLS-AlSi10Mg_200C, as well as sandblasted and ground A360.1 cast alloy. For the samples just immersed in the electrolyte solution (t = 0 hr), the Bode plots show significantly lower absolute values of impedance ($|Z|$ Ωcm^2) for both ground DMLS-AlSi10Mg_200C and ground A360.1 cast sample than the as-printed and sandblasted ones at lower frequency range, where the as-printed surfaces show the highest resistance with more than one order of magnitude higher values of $|Z|$

than the sample with the ground surface, corroborating a slow kinetic for the corrosion reactions. The observed superior impedance of the as-printed sample in just immersed condition is also in agreement with the polarization graphs of the samples in Figure 3-3, confirming the lowest corrosion current density for the as-printed sample.

The general trend of the impedance with increasing immersion time for the as-printed and sandblasted surfaces for both DMLS and cast alloys (Figure 3-5a-Figure 3-5e) was found to be similar confirming a decrease in the modulus of impedance at low frequencies. However, both ground surfaces showed a different behavior compared to the as-printed or the sandblasted ones. As evidenced in Figure 3-5, the DMLS-ground specimen showed an increase of the absolute value of the impedance by two orders of magnitude at low frequencies with increasing the immersion time from 0 hr (just immersed) to 48 hr. This increase in the impedance value of the ground surface with the exposure periods exhibited the growth of protective passive film thickness and improvement in the film's resistivity towards diffusion of aggressive ions, through the passive layer, as proposed by Onofre-Bustamante *et al*. [74]. After 72 hr, the modulus of impedance reaches values slightly lower than 10^5 Ωcm^2, indicating still a slow kinetics for corrosion reactions and low corrosion rates. Longer immersion times (96 hr) for the ground surface causes a slight decrease in its absolute value of impedance at low frequencies. Very similar behavior but at one order of magnitude lower impedance value was detected for the cast-ground sample.

The phase angle *vs* frequency plots in Figure 3-5 of the DMLS-AlSi10Mg_200C and A360.1 cast alloy with different surface finishing confirmed a typical behavior of passive

aluminum characterized by a broad and apparent capacitive peak in the frequency range between 0.1–100 Hz. Jafarzadeh *et al*. [81] reported that for aluminum alloys, such wide peaks are ascribed to the superposition of two individual peaks with non-discriminated time constants, one at a lower frequency and the other at a higher frequency. The peak (capacitive loop) at the lower frequency determines the diffusion through the passive layer and inside the localized corroded areas, whereas the peak at the higher frequency can result from the sealing effect of the corrosion film in active areas, such as surface porosities. Such separated capacitive loops can be clearly detected for sandblasted surfaces in just immersed condition (Figure 3-5a) or the as-printed DMLS sample after 96 hr of immersion time (Figure 3-5e).

It is worth noting that for the ground surface, the maximum phase angle has shifted towards the lower frequencies by increasing immersion time, which is another indication for the formation of double layer capacitance and a decrease in active anodic surface area, as reported by Lee *et al*. [82].

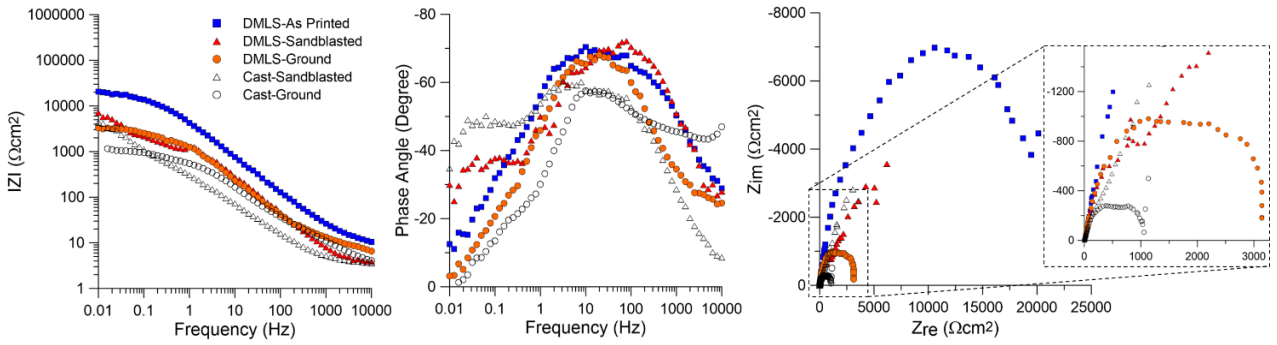

(a) 0 hr (Just immersed)

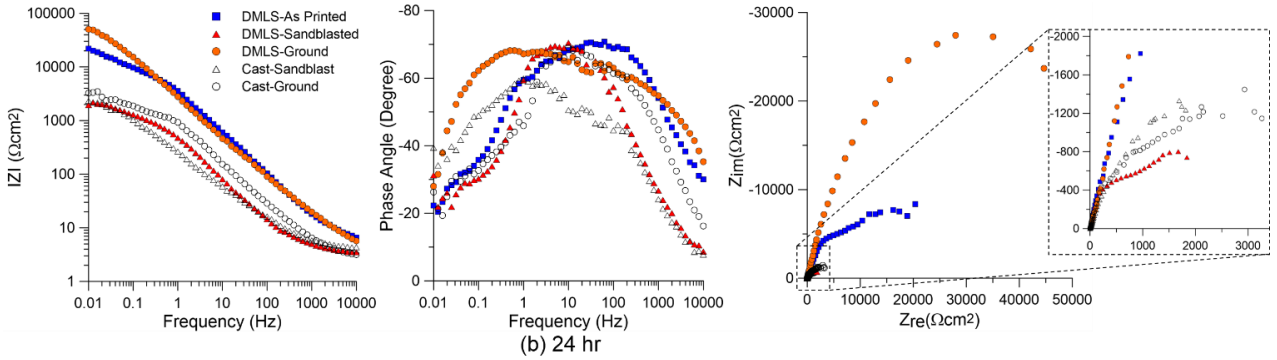

(b) 24 hr

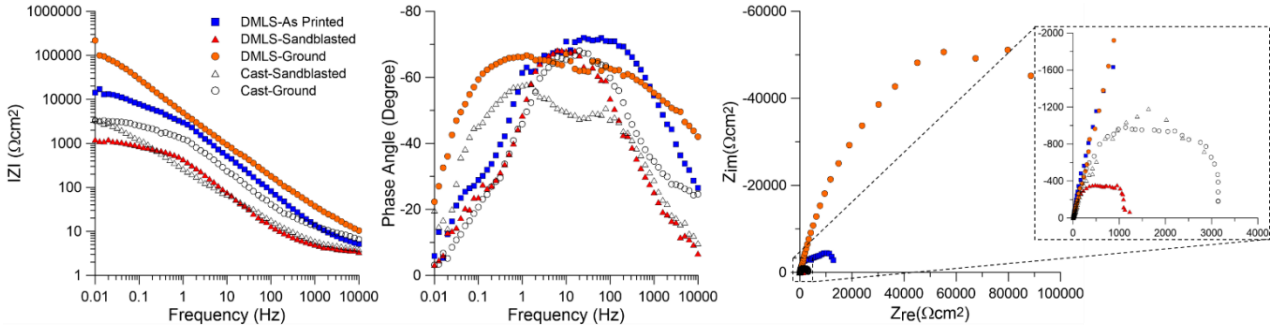

(c) 48 hr

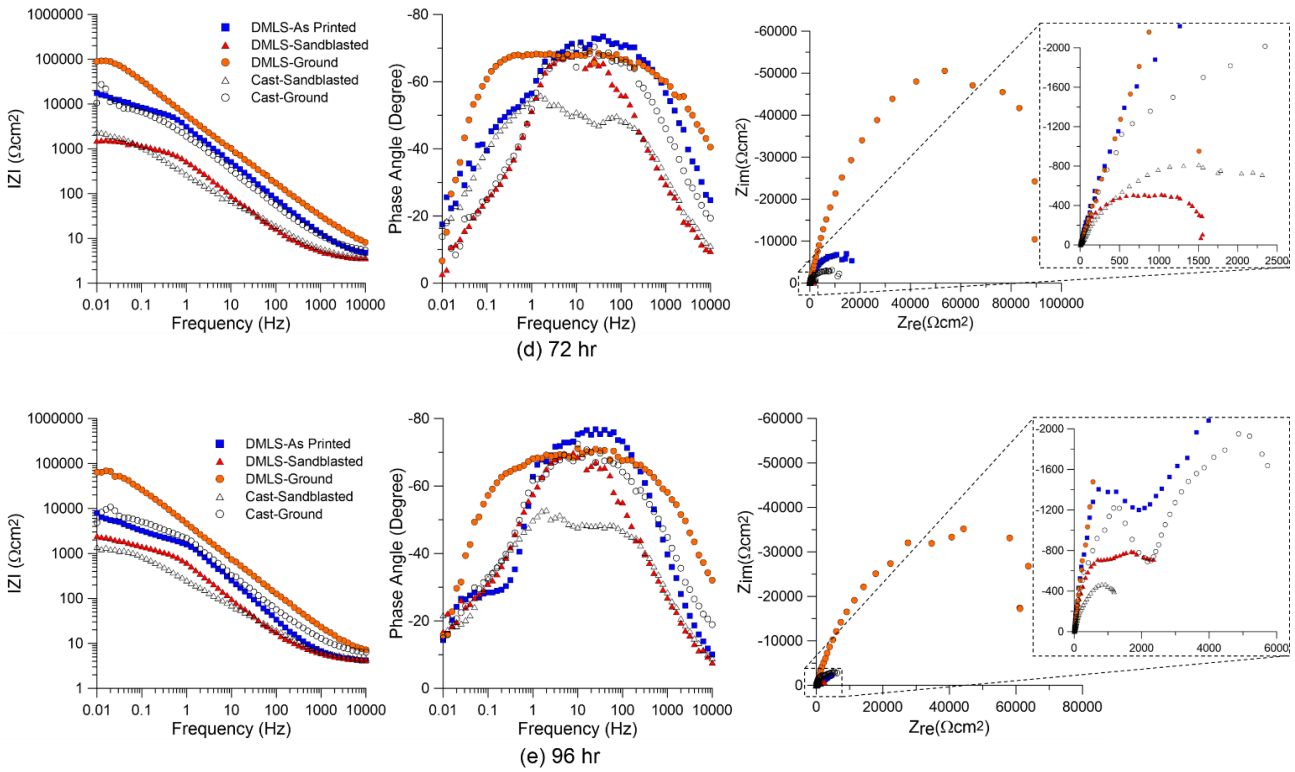

Figure 3-5: EIS spectra of DMLS-AlSi10Mg_200C and A360.1 Al alloys with different surface finishes: (a) right after immersion, and after (b) 24 hr, (c) 48 hr, (d) 72 hr, and (e) 96 hr of immersion time in aerated 3.5 wt.% NaCl solution.

From the Nyquist plots (Z_{im} vs. Z_{re}) in Figure 3-5, the diameter of capacitive arcs for the as-printed DMLS sample and both DMLS and cast sandblasted samples has decreased considerably with exposure time. In contrast, for the ground surfaces (Figure 3-5), the dimension of the capacitive arc increases with exposure periods up to 48 hr and then decreases for longer immersion times (96 hr). For the ground surface, as the exposure time increases, the passivating behavior of the surface enhances as a result of the reduction in

the active surface area of the ground surface and the growth of passive layer, leading to an increase in polarization resistance. After 48 hr of exposure, the enlargement of the capacitive arc reaches its maximum, exhibiting higher corrosion resistance. This corresponds to the formation of a uniform, dense, and protective passive layer, consistent with the results from the Bode plots. At longer immersion times, the diameter of capacitive arc decreases, confirming a reduction in corrosion resistance.

As shown in Figure 3-5, the size of the cast-ground capacitive loop was always noticeably smaller than that of the DMLS-ground sample for all the immersion times. This evidenced the formation of a passive layer with more protective nature on the surface of DMLS sample. However, for the sandblasted surfaces, this difference was less significant and a more comparable capacitive loop size was measured for the DMLS and cast alloys.

EIS spectra fitting

The equivalent electrical circuit, shown in Figure 3-6a, was used to describe the localized corrosion of both alloys. A similar simplified equivalent circuit was used by Cabrini *et al*. [19] to describe the impedance graphs modifications by exposure time for DMLS-AlSi10Mg alloy. In this circuit, R_p and Constant Phase Element (CPE_p) correspond to the resistance and capacitive behavior of the passive layer. It is worth noting that the non-ideal capacitive behavior of heterogeneous interfaces is defined by using the CPE. R_{pit} and CPE_{pit} correspond to the resistance and the constant phase element of the corroding pits,

respectively, and R_{el} is the electrolyte resistance between the test electrode (sample) and the reference electrode. The impedance of a constant phase element is expressed as

$$Z_{CPE} = Y_o^{-1}(j\omega)^{-n} \quad (1)$$

where Y_o is the true capacitance of the protective layer (the CPE constant), ω is the angular frequency, and j is the imaginary unit ($j = \sqrt{-1}$). The constant n is related to the constant phase angle and varies between 0 and 1, as discussed by Arrabal *et al*. [71]. Figure 3-6b shows the fitting of EIS data resulted from the application of the proposed equivalent circuit in Figure 3-6a to the obtained experimental Nyquist data after 72 hr of immersion time. Table 3-2 summarizes the calculated fitted parameters of the equivalent circuit shown in Figure 3-6a for all the immersion times from 0 to 96 hr.

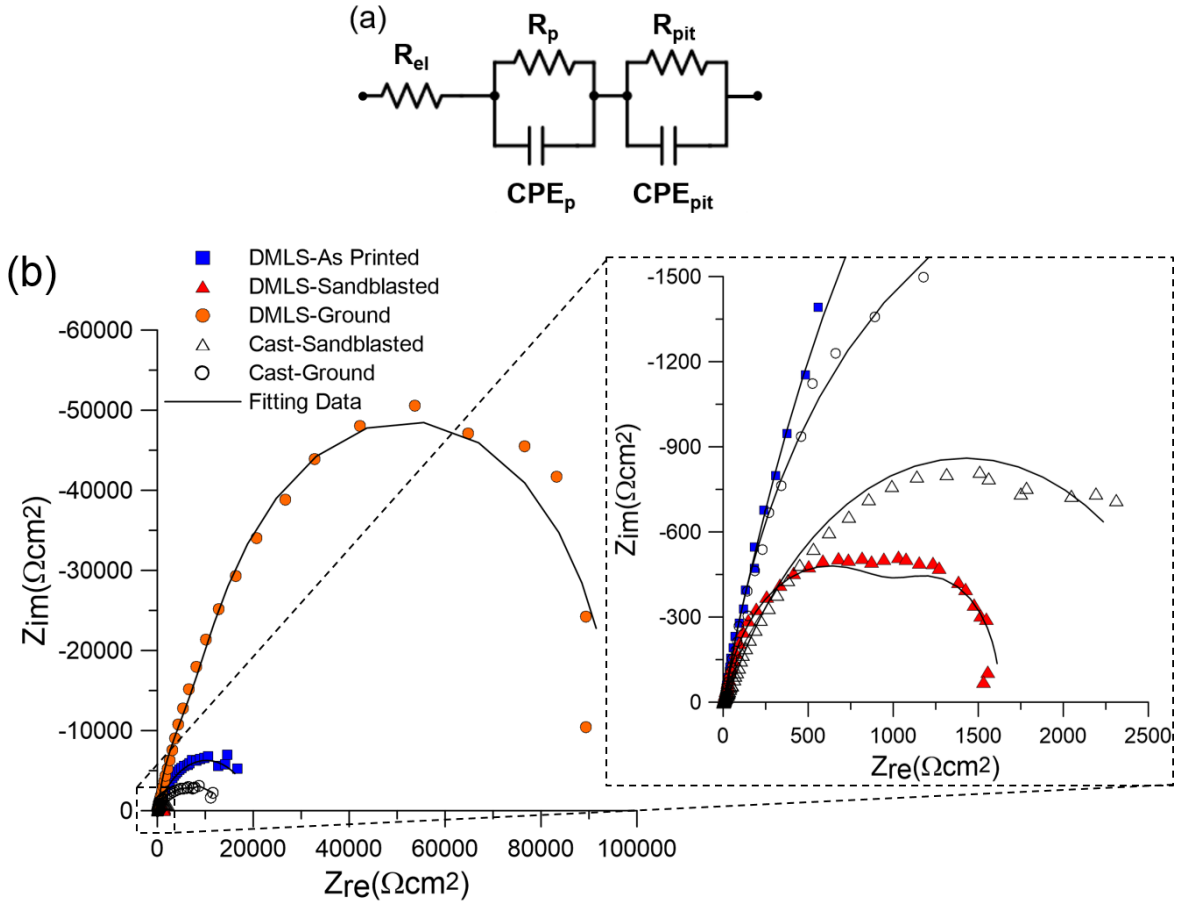

Figure 3-6: (a) The equivalent circuit proposed to describe the EIS data over time for the studied materials and (b) fitting of Nyquist plots (after 72 hr of immersion time) by applying the proposed equivalent circuit in (a).

Table 3-2: EIS parameters of the equivalent circuit shown in Figure 3-6a

Time (*hr*)	CPE_p, Y_o ($\mu S\ Sec^n\ cm^{-2}$)	R_p ($k\Omega\ cm^2$)	CPE_{pit}, Y_o ($\mu S\ Sec^n\ cm^{-2}$)	R_{pit} ($k\Omega\ cm^2$)
DMLS-As Printed				
1	13.44	16.65	23.44	7.00
24	16.24	12.40	17.01	11.54
48	22.27	7.58	24.37	6.59
72	104.72	0.68	11.85	20.27
96	50.62	2.11	29.39	4.94
DMLS-Sandblasted				
1	23.02	7.20	63.85	1.47
24	45.75	2.47	100.07	0.73
48	194.14	0.26	79.73	1.04
72	122.90	0.53	77.36	1.09
96	130.97	0.48	43.96	2.63
DMLS-Ground				
1	84.50	0.95	45.17	2.52
24	6.04	57.99	6.12	56.68
48	37.12	3.42	3.60	129.4
72	4.88	80.71	15.30	13.61
96	5.25	72.16	60.46	1.60
Cast-Sandblasted				
1	86.25	0.92	26.80	5.68
24	31.53	4.41	46.73	2.39
48	79.72	1.04	55.27	1.84
72	1007.53	0.02	42.21	2.80
96	497.68	0.06	62.22	1.53
Cast-Ground				
1	222.66	0.21	87.47	0.90
24	44.82	2.55	42.30	2.79
48	50.16	2.14	66.17	1.39
72	318.92	0.12	16.39	12.22
96	20.31	8.75	93.59	0.81

Comparing the general passive layer resistance of the alloys (R_p) to the pitting resistance (R_{pit}), it is evident that the R_p of the DMLS alloy is higher than its R_{pit} for both as-printed and sandblasted surfaces up to 48 hr, which indicates that the corrosion behavior

initially is more dominated by the pitting attack on the surface than general uniform corrosion. This is consistent with the observed active behavior of the surface from the potentiodynamic polarization results presented in Figure 3-3. For longer immersion times, the pitting resistivity of the surface improves (up to 72 hr for the as-printed sample). The DMLS-ground sample in just immersed condition showed a very low R_p and R_{pit} values confirming a very active surface containing pits that have not been repassivated, as its R_{pit} value suggests. This is also in agreement with the detected high corrosion current density and lower corrosion resistivity of DMLS-ground sample than the as-printed or sandblasted ones during potentiodynamic polarization testing (see Table 3-1). However, after one day of immersion, the complete repassivation of the pits on the DMLS-ground surface is evident, as the comparison of R_{pit} values for 1 hr and 24 hr suggests, leading to an enhanced resistivity of the surface against both pitting and uniform corrosion attacks. As reported by Jafarzadeh *et al*. [81], the pit repassivation in aluminum alloys happens through simultaneous separation of cathodic regions (IMC particles or in general cathodic regions, such as Si particles for the AlSi10Mg alloy) from the pit location on alloy's surface as a result of heavily dissolution of Al matrix around the particle, along with the buildup of the corrosion products. This justifies the observed increase in the impedance values by immersion time for the ground DMLS sample, ascribed to the formation of a more stable passive film on the ground surface after 24 hr of immersion in the electrolyte than the as-printed or sandblasted surfaces. This improvement continues up to 48 hrs, but after longer

immersion times (at 96 hr), the DMLS-ground surface becomes very susceptible to pitting corrosion attack.

By increasing the exposure time from 48 to 72 hrs, the pitting resistance of the DMLS-ground sample decreases considerably, which is attributed to the general removal of the corrosion products from the surface and the exposure of the next cathodic sites (Si) to the corrosive electrolyte. As the R_{pit} data of DMLS-ground sample at 1, 48, and 96 hr suggest, it is expected that the exposure of the Si particles, as the cathodic sites, and occurrence of repassivation happens in a cyclic manner.

Cast samples are generally showing significantly lower R_p and R_{pit} values than those of their DMLS counterparts, confirming a more severe general corrosion and pitting corrosion attack on their surface. This also confirms the potentiodynamic polarization results in Figure 3-3. Starting from 24 hr of immersion time, the R_{pit} values of the sandblasted cast alloy indicate that the repassivation behavior was not detected even after 96 hr of immersion time. This behavior should be mostly associated with the surface roughness of the sandblasted sample, since for the cast-ground sample, after 72 hr of immersion time, repassivation of the pits, although probably incomplete (as some degree of noise at very low frequencies still remained), is evident.

In the case of cast samples, comparing the R_{pit} and R_p values for both sandblasted and ground surfaces confirms a higher pitting resistance than general passive layer resistance, indicating that the uniform corrosion of the cast alloy dictates over the pitting corrosion of

the alloy. This also confirms the observed clear passive region on the polarization curves of the cast samples (shown in Figure 3-3).

Significantly low R_p and R_{pit} values of both DMLS and cast samples with sandblasted surface finish indicate a very low general passive layer resistance along with low pitting resistance of the surface, confirming that the repassivation of the formed pits has not been completed. It also indicates that for the sandblasted surfaces, the superficial roughness of the sample dominates over the impact of microstructure or chemical composition of the alloy in controlling the corrosion properties of the surface, which were reported as the main reason for the improved corrosion resistivity of DMLS-AlSi10Mg alloy than its cast counterpart by Fathi *et al*. [32]. Corrosion resistance degradation (both R_{pit} and R_p values) of the as-printed surfaces as a result of sandblasting can be explained by the removal of the stable partially melted particles from the surface with protective nature, as proposed by Fathi *et al*. [32], accompanied by the introduced surface roughness.

Therefore, to benefit from the improved corrosion properties of the DMLS manufactured components for applications in harsh environments over the conventionally manufactured parts, post-grinding of the as-printed surfaces is strongly recommended; and sandblasting of the parts should be avoided. Otherwise, the superficial roughness of the as-printed or sandblasted surfaces would dominate over the impact of microstructure and deteriorate the corrosion properties of the alloy significantly.

3.5 Conclusions

The impact of surface finishing, *i.e.* as-printed surface, ground, and sandblasted surfaces, on the corrosion performance of DMLS-AlSi10Mg_200C samples *vs* its cast counterpart (die cast A360.1 Al alloy) was investigated in aerated 3.5 wt.% NaCl solution at 25°C. The following conclusions can be drawn from this study:

1. The results highlighted improved corrosion resistance of the DMLS-AlSi10Mg_200C than its cast counterpart with a similar surface finish, known to be dominated by its finer microstructure containing only a continuous network of Si phase formed along aluminum intercellular regions without formation of coarse precipitates and IMC particles with cathodic nature relative to the α-Al matrix. This improvement was more pronounced after grinding than sandblasting.
2. At the initial stage of immersion, the as-printed DMLS-AlSi10Mg_200C surface demonstrated the lowest corrosion current density accompanied by a minor attack on its surface, whereas the ground sample confirmed the highest corrosion current density and was characterized by a selective attack predominantly at the transition zone between the melt pools, where coarsening of the Si particles were observed. This was attributed to the existence of less protective passive film on the ground surface than the as-printed or sandblasted ones at the initial stage of immersion, confirmed by the EIS results.
3. For longer immersion times, *e.g.* after 24 hr of immersion in the electrolyte, the corrosion behavior changed and the ground DMLS-AlSi10Mg surface demonstrated

the highest resistance to the selective attack, which was associated with the formation of a stable, dense, and thick passive film on its surface. Surface porosities and the superficial roughness on the surface of as-printed and sandblasted samples were found to be more detrimental over time and deteriorated the corrosion performance of the alloy, confirming the necessity of performing the post-grinding operation and avoiding sandblasting after additive manufacturing of Al alloy components through DMLS.

Chapter 4

On Microstructure and Corrosion Behavior of AlSi10Mg Alloy with Low Surface Roughness Fabricated by Direct Metal Laser Sintering[3]

4.1 Abstract

In this study, in-depth microstructure and electrochemical properties of highly smoothed AlSi10Mg parts fabricated through direct-metal-laser-sintering are reported. The samples with the lowest surface roughness were characterized by having a periodic large and small melt pools (MPs) pattern in their upskin layers. Consequently, a noticeably coarser eutectic-Si network, Al-dendrite and grain size formed along the larger MPs' borders, rationalized by their slower solidification rate. Such microstructural features were found to control/deteriorate the electrochemical performance of the as-printed samples than their surface roughness. An improved electrochemical stability for the samples that experience the fastest solidification rate along their MP-boundaries was revealed.

[3] P. Fathi, *et al*., *Corrosion Science Journal* (Impact Factor: 5.238), In Press, Available online 31 May 2019 [117].

4.2 Introduction

In contrast to subtractive manufacturing technologies, additive metal manufacturing corresponds to the process of fabrication of metallic objects layer by layer using a 3D computer-aided design (CAD) model [1]. To accomplish this, various additive manufacturing techniques have been developed so far to fabricate metallic components using metal powder, which can be classified into two process families: 1) Selective laser melting (SLM) also known as direct metal laser sintering (DMLS) or selective electron beam melting (SEBM); 2) Laser metal deposition (LMD), also known as direct laser fabrication (DLF) [83]. In DMLS/SLM process, a high energy laser beam is used to selectively melt and join metal powder layer by layer until a fully dense and functional part is fabricated [84]. Likewise, the SEBM process functions based on a layer by layer deposition of metal powder followed by subsequent melting of each layer; however, instead of a laser in an argon protected atmosphere, a high energy electron beam is used as the heat source in a vacuum environment [85]. A DMLS/SLM fabricated part is known to have different properties than its SEBM fabricated counterpart, mainly ascribed to different heating and cooling rates that the material experiences during sintering process associated with each technique [83,84]. In addition, the former has been characterized by a superior surface finish (arithmetic average roughness (R_a) ~ 4-11 µm) in comparison with the latter (R_a ~ 15-35 µm) [83].

Such initial surface roughness is known as a major drawback for adopting both SEBM and DMLS/SLM parts in the as-printed condition. This roughness is predominantly

resulted from balling and dross formation during solidification in the melt pool [27], as well as the attachment of partially melted powder particles to the surface of the sintered part [86,87]. This issue is more critical for applications that require high corrosion performance or fatigue strength, where having a rough surface can degrade both electrochemical performance and fatigue life of the material [25,26]. For such applications, typically the as-printed component undergoes a post-printing surface treatment process, such as sand-blasting [32], shot peening [27], or chemical etching [30], in which the surface roughness of the as-printed part is reduced. However, this requires an extra step in the manufacturing of the part leading to a higher production cost. Therefore, achieving the required surface roughness in the as-printed condition would contribute to lowering the fabrication costs and would make the DMLS/SLM process economically more viable [26,30]. This could be done through optimizing the process parameters [88], while assuring that the part's integrity, *i.e.* mechanical properties, porosity level, corrosion performance, etc., has not been faded.

The effects of DMLS process parameters, *i.e.* laser power, scanning speed, and hatching distance, on the achieved surface roughness of the as-printed DMLS-AlSi10Mg alloy have been investigated by Calignano *et al.* [27], where laser scanning speed was reported to have the highest impact on controlling the surface roughness of the printed part. The authors have also shown that shot peening using glass beads, as a post-treatment process, can significantly lower the surface roughness of the alloy [27]. In a similar study by Tian *et al.* [88] on SLM-Hastelloy X, the authors reported the formation of large balling

on the surface and an increased surface roughness at high laser scan speed as a result of Rayleigh instability. Increasing the energy density of the laser or reducing the scan speed was reported to reduce the balling effect due to the increased melt volume and decreased melt viscosity [88]. The authors also reported that large overlaps (large beam offset and small hatch distance) increase the surface roughness of the part due to more attachment of the particles on the surface [88].

In our previous work [26], various combinations of DMLS process parameters including laser power, scan speed, hatch spacing, and laser offset distance were utilized in printing the last top layers (upskin layer) of AlSi10Mg parts. This was to achieve a better surface roughness, while the core processing parameters and consequently its properties were kept the same. Using higher laser energy density and lower beam offset in printing the upskin layers was found to reduce the surface roughness of DMLS-AlSi10Mg part significantly (up to five times) [26]. This improved surface roughness was also complemented with the reduced porosity levels of the printed part [26].

Although the obtained mechanical properties of the parts fabricated using the same core parameters are possibly consistent, their electrochemical stability and corrosion resistivity do not follow the same trend as those are primarily controlled through the surface characteristics of the parts, including the surface roughness, composition, and microstructure of the upskin layer. The general trend between the surface roughness and corrosion resistance of a surface is known to be reversed, suggesting that increasing the surface roughness of the alloy would deteriorate the corrosion performance of the surface

[32]. It is noted that using different DMLS processing parameters would affect not only the surface roughness, but also the resultant microstructure of the printed part. Thus, the characterization of DMLS-AlSi10Mg parts processed through various upskin parameters is required to be able to identify the factors dictating the electrochemical stability and corrosion behavior of the printed parts.

In a recent study [25], the corrosion and fatigue performance of SLM-AlSi10Mg were investigated and comparisons were conducted between as-printed and polished surface finishes. The authors reported an improved electrochemical stability and fatigue performance for the samples with a polished surface than the as-printed ones [25].

In another previous study, Cabrini *et al*. [22] investigated the effects of different surface finishing, *i.e*. as-printed, shot peened, versus polished surface, on the corrosion performance of DMLS-AlSi10Mg alloy and reported that the polished surfaces and the shot peened ones have superior performance over the as-printed surfaces. The same authors (Cabrini *at al*. [24]) also performed a conversion treatment through dipping of DMLS-AlSi10Mg parts with various surface finishes in Ce(III) salt electrolyte and concluded that a polished and pickled surface shows a better corrosion resistance after this conversion treatment, while the as-printed corrosion property was not found to be improved.

In a recent study by the authors [89], the impacts of various surface finishing procedures, including the grinding and sand-blasting, on the corrosion resistance of DMLS-AlSi10Mg alloy in aerated 3.5 wt.% NaCl electrolyte were studied and compared with the as-printed ones and their cast counterparts (A360.1 alloy). The authors highlighted

improved corrosion resistance of DMLS fabricated samples than the cast alloy with a similar surface finish [89]. In addition, surface porosities and superficial roughness covering the surface of the as-printed and sand-blasted samples were reported to deteriorate the corrosion resistance of the DMLS-AlSi10Mg alloy over time [89]. On the other hand, grinding of the as-printed samples was found to be an effective post-printing surface treatment to improve the electrochemical stability and corrosion performance of the DMLS-AlSi10Mg alloy [89]. Nonetheless, in all above corrosion-surface finish relationship studies, the applied post-printing surface treatment was only implemented to change the surface roughness of as-printed AlSi10Mg without any change in the alloy's surface microstructure.

To the best of authors' knowledge, there is no study in the open literature that directly evaluates the microstructural modification and the resultant corrosion performance of a DMLS-AlSi10Mg part through changing the printing process parameters. In a few past studies, general corrosion behavior of the alloy in various environments including Harrison solution [19,22,24], 3.5 wt.% NaCl solution [32,89–91], 0.1 M NaCl solution [21], and 30 g/L of NaCl solution with 10 mL/L of HCl [20] were investigated. Unanimously, all the authors reported susceptibility of the as-printed DMLS/SLM AlSi10Mg to selective corrosion attack predominantly at the transition zone between the melt pools, where coarsening of the Si particles were observed. In addition, anisotropic corrosion properties were reported for the DMLS-AlSi10Mg planes parallel to the building direction *vs* the planes perpendicular to the building direction [21,22]. According to Cabrini *et al*. [22] and

Revilla *et al*. [21], the plane parallel to the building direction has lower corrosion resistance than the one perpendicular to the building direction due to the higher density of the melt pool boundaries as the susceptible areas to selective corrosion attack on the side plane. Therefore, any processing parameter that changes the resultant microstructure of DMLS-AlSi10Mg alloy, can directly influence the corrosion resistivity of the part. As an example, but on a different alloy, Kurzynowski *et al*. [92] have shown that increasing the laser power in selective laser melting of 316L stainless steel metal powder directly changes the final microstructure of the alloy after solidification and resulted in an increase of both texture degree and grain shape aspect ratio, while decreases the amount of δ-ferrite phase. Such microstructural variations could potentially impact the corrosion properties of the alloy significantly.

This study aims to achieve a comprehensive understanding of the microstructure and corrosion properties of DMLS-AlSi10Mg parts with significantly lowered surface roughness obtained by tuning the DMLS process parameters instead of applying a post-printing operation. The microstructural analysis of the samples was carried out using optical microscopy (OM), scanning electron microscopy (SEM), X-ray diffraction (XRD), and electron backscatter diffraction (EBSD) analysis techniques. The electrochemical behavior of the samples was evaluated in aerated 3.5 wt.% NaCl solution through monitoring open circuit potential (OCP) evolution by time, anodic and cyclic potentiodynamic polarization techniques, and electrochemical impedance spectroscopy (EIS), followed by corrosion morphology study of the corroded surfaces using scanning

electron microscopy. A detailed relationship between the microstructural characteristics and the resultant corrosion performance of the fabricated samples was delineated systematically.

4.3 Experimental Procedure

Materials and DMLS Process

Cubic samples (15×15×15 mm) were fabricated from gas atomized AlSi10Mg powder with the average particle size of 15-45 µm using an EOS M290 metal 3D printer machine (EOS, Germany), located at AMM (Additive Metal Manufacturing) company in Concord, Canada. Table 4-1 shows the nominal chemical composition of the powder used herein. The DMLS process was performed at elevated platform temperature of 165 °C in an argon atmosphere using a 400 W Ytterbium-fiber laser with a beam spot diameter of 100 µm. Other processing parameters that were kept consistent in the manufacturing of all samples include powder layer thickness of 30 µm and stripe hatch strategy with 67° laser beam rotation between successive layers.

Table 4-1: Nominal chemical compositions of AlSi10Mg_200C powder (wt.%)

Element	Si	Mg	Fe	Mn	Ti	Zn	Cu	Al
AlSi10Mg	9.0 - 11.0	0.2 - 0.45	≤ 0.55	≤ 0.45	≤ 0.15	≤ 0.10	≤ 0.05	Bal.

To fabricate samples with the same core properties but different surface roughnesses, the sample's cube model was divided into three sections, including the first two layers in the bottom of the cubes, denoted as the downskin, the last three layers on top, denoted as the upskin, and the rest of the layers in between (the core). The schematic in Fig. 1a illustrates the location of each section, *i.e.* downskin, core, and upskin, in the fabricated samples. Table 4-2 summarizes the processing parameters used in printing the core of each sample. In order to achieve different surface roughnesses, three groups of samples, namely Regular, Surface 1, and Surface 2 (shown in Figure 4-1b), were fabricated using different processing parameters in printing their upskin and downskin layers. Table 4-3 and Table 4-4 summarize the processing parameters used for fabrication of upskin and downskin layers, respectively. As summarized in Table 4-3 and Table 4-4, Surface 1 and Surface 2 samples were fabricated using the exact same processing parameters with slightly different hatch distance and beam offset values. This study focuses on the resultant surface roughness, microstructure, and electrochemical stability of only the upskin portion of each sample. To characterize the surface roughness of the top surface (upskin layer) of as-printed samples, a high-resolution 2D profiler (AlphaStep® D-500 Stylus Profiler, KLA-Tencor Corporation, Milpitas, Ca) was utilized.

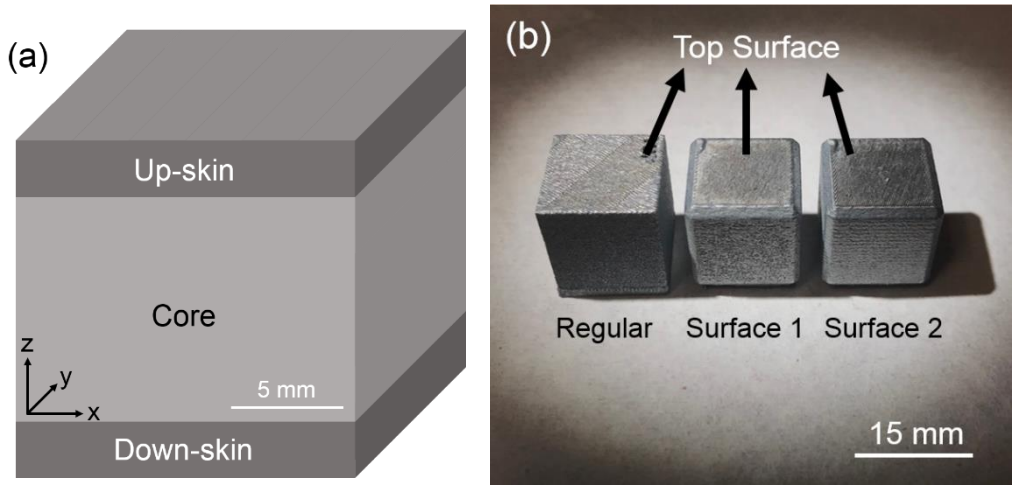

Figure 4-1: (a) Schematic of the DMLS manufactured cubes showing the positions of upskin, core, and downskin layers relative to each other and (b) three groups of DMLS-AlSi10Mg cubes, namely Regular, Surface 1, and Surface 2, manufactured using different process parameters for their upskin and downskin layers.

Table 4-2: The used DMLS process parameters for fabrication of the core of each sample.

Sample	Hatch Distance (mm)	Scan Speed (mm/s)	Laser Power (W)	Stripe Width (mm)	Stripe overlap (mm)	Beam Offset (mm)
Regular	0.19	1300	370	7	0.02	0.02
Surface 1	0.19	1300	370	6	0	0.15
Surface 2	0.19	1300	370	6	0	0.15

Table 4-3: The used DMLS process parameters for fabrication of the upskin layers of each sample.

Sample	Hatch Distance (mm)	Scan Speed (mm/s)	Laser Power (W)	Overlap with Core (mm)	Min. Length (mm)	Beam Offset (mm)
Regular	0.21	1000	360	0.02	0.2	0.2
Surface 1	0.13	775	370	0	0.2	0.15
Surface 2	0.12	775	370	0	0.2	0.1

Table 4-4: The used DMLS process parameters for fabrication of the downskin layers of each sample.

Sample	Hatch Distance (mm)	Scan Speed (mm/s)	Laser Power (W)	Overlap with Core (mm)	Min. Length (mm)
Regular	0.21	1150	340	0.02	0.2
Surface 1	0.12	775	370	0	0.2
Surface 2	0.12	775	370	0	0.2

Microscopic Characterization

Following Al alloys standard sample preparation procedures and using a Struers' Tegramin-30 grinder/polisher (Struers, Denmark), the upskin surface of each sample was carefully polished to a mirror-like finish and etched using Keller's reagent (2.5 cm^3 HNO_3, 1.5 cm^3 HCl, 1 cm^3 HF, and 95 cm^3 H_2O) for 20 s. Macro and microstructural details of the samples were revealed using a Nikon Eclipse 50i optical microscope (Nikon Instruments, Melville, NY) and an FEI MLA 650F scanning electron microscope (FEI, Hillsboro, Oregon) equipped with a high throughput Bruker energy dispersive X-ray (EDX) analytical system (Bruker, Billerica, Massachusetts) and an HKL EBSD system (Oxford Instruments, Abingdon, UK). To obtain crystallographic orientation micrographs

(inverse pole figures (IPF)), pole figures (PF), and grain boundary maps, the EBSD analysis was also performed on polished samples using a step size of 0.35 μm and 4×4 binning. Channel 5 software (HKL Inc., Hobro, Denmark) was used to post process and analyze the EBSD data.

XRD technique was used for the phase analysis of the samples using a Rigaku Ultimate IV XRD machine (Rigaku, The Woodlands, Texas) with Cu-K_α source (λ=1.5406 Å) at 40 kV and 44 mA over a diffraction angle range of 5°-90° with a step size of 0.02°.

Electrochemical Measurements

The electrochemical measurements were carried out on the top surface (x-y plane) of the as-printed upskin layers of all three DMLS produced samples using a standard three-electrode cell setup, one fitted with a graphite rod as the counter electrode (CE), a saturated silver/silver chloride (Ag/AgCl) as the reference electrode (RE), and the working electrode (as-printed DMLS-AlSi10Mg samples), in a multiport glass cell connected to an IVIUM CompactStat™ computer-controlled Potentiostat (IVIUM Technologies, Eindhoven, The Netherlands). A copper wire was connected to the back surface of each sample through a stainless steel nut. Only the top surface (upskin portion) of each sample was exposed to the electrolyte and its electrochemical active surface area was kept constant at 0.2 cm^2. Prior to corrosion testing, the samples surfaces were ultrasonically cleaned in ethanol for 5 min and dried under a cold air stream.

All electrochemical measurements in this study were performed in aerated 3.5 wt.% NaCl solution. For each experiment, a freshly prepared solution was used, and its temperature was maintained at 25±0.5 °C using a temperature-controlled water bath. OCP was monitored for 60 min prior to each electrochemical testing performed herein to allow for stabilization of the OCP. Anodic potentiodynamic polarization (APP) and cyclic potentiodynamic polarization (CPP) tests were performed at a scanning rate of 0.125 mV/s, commencing at -20 $mV_{Ag/AgCl}$ and -0.3 $V_{Ag/AgCl}$ *vs* OCP for the APP and CPP testing, respectively. For the CPP testing, the sweep direction was inverted when the current reached 1 mA/cm^2. For each DMLS-AlSi10Mg sample with different surface roughness, at least three samples were tested to check the reproducibility of the data.

EIS tests were also conducted in aerated 3.5 wt.% NaCl solution at 25 °C for immersion times ranging from initial immersion up to 96 hr, every 24 hr. The EIS tests were carried out at the OCP in the frequency range of 10 kHz to 10 mHz. Similar to the polarization tests, the repeatability of the EIS results was measured by testing at least three samples. Impedance spectra were recorded using ±10 mV sinusoidal potential signal and logarithmic sweeps of ten points per decade. Both the impedance spectra and the corrosion parameters were interpreted using the IVIUMSOFT electrochemical analysis software (IVIUM Technologies, Eindhoven, The Netherlands). A complex non-linear least squares fitting routine was utilized to fit the impedance results to an appropriate equivalent electric circuit.

After both APP and CPP experiments, to study the corrosion morphology of each sample, the formed corrosion products from the surface of each sample were removed by

immersing the samples in a concentrated HNO_3 solution (15.8 N) in an ultrasonic bath for 15 min [54], and then washed in distilled water followed by ultrasonic cleaning of the samples in ethanol for 5 min.

4.4 Results

Surface Topography in As-Printed Condition

Figure 4-2 shows the SEM micrographs from the upskin surface (x-y plane) of the as-printed Regular, Surface 1, and Surface 2 samples and their corresponding 2D surface roughness profiles (Figure 4-2d). The Regular DMLS-AlSi10Mg surface (Figure 4-2a) demonstrates high degree of surface irregularities resulted from the attachment of partially melted powder metal particles to the surface during the DMLS process [86,87], creating a superficial roughness of R_a = 5.1 ± 1.5 µm on the surface in as-printed condition. Here, the R_a value represents the arithmetic average roughness of the upskin layer.

As clearly depicted in Figure 4-2b and Figure 4-2c, the obtained roughness on Surface 1 and Surface 2 was noticeably lower than that of the Regular sample, containing a smaller number of partially melted particles attached to their surfaces. The measured roughness values for Surface 1 and Surface 2 samples were R_a = 1.4 ± 0.5 µm and 1.1 ± 0.2 µm, respectively. Therefore, the process parameters used in the fabrication of Surface 1 and Surface 2 upskin layers have contributed to the smoothest surface quality, far better than the Regular surface. The improved surface roughness of the upskin layer in Surface 1 and Surface 2 is predominantly attributed to the higher energy density used in the

manufacturing of those samples. The calculated volumetric energy densities (*VED*) used for fabrication of upskin layer in Surface 1 and Surface 2 samples were 122.4 and 132.6 J/mm^3, respectively, which are significantly higher than that of the Regular sample (57.1 J/mm^3). It should be noted that the commonly used equation (1) was used to calculate the *VED* values herein [93–95].

$$VED = {}^{P}/_{(h.V.t)} \quad (1)$$

where P is the laser power (W), h is the hatch distance (mm), V is the laser scan speed (mm/s), and t corresponds to the powder layer thickness (mm). Previous studies have highlighted that using higher laser power and lower scan speed in additive manufacturing of metallic components reduces the possibility of balling effect and dross formation in the melt pools [27], leading to a smoother surface finish in the as-printed condition.

The slightly smaller hatch distance applied in the fabrication of Surface 2 upskin layer has led to a lower surface roughness for this sample than Surface 1 sample. The obtained microstructure and the resultant corrosion properties of the upskin layers of the fabricated samples with different surface finishes in as-printed condition are investigated in the following sections.

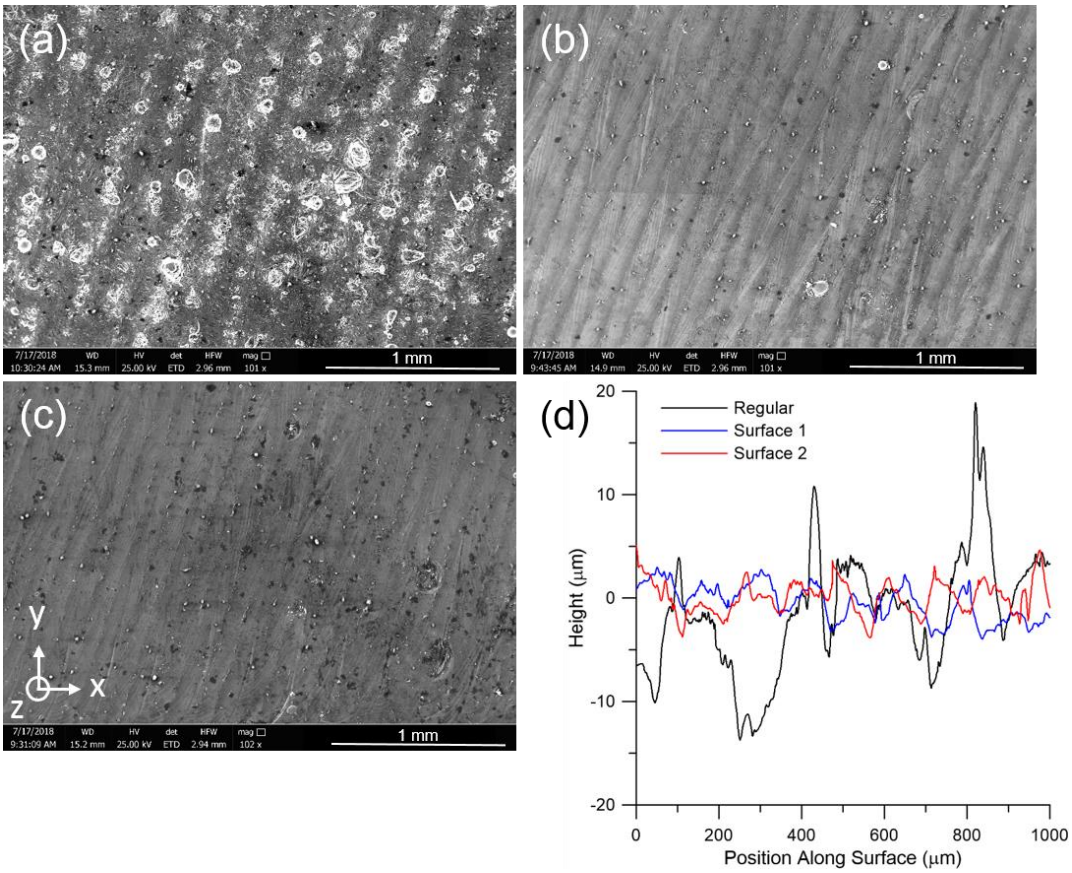

Figure 4-2: SEM images taken from the top surface (x-y plane) of the as-printed DMLS-AlSi10Mg in (a) Regular, (b) Surface 1, (c) Surface 2 conditions, (d) the surface profiles of the Regular, Surface 1, and Surface 2 samples.

As-Printed Microstructure

Fig. 3 shows the optical micrographs taken from the top view of the Regular, Surface 1, and Surface 2 samples. The morphologies of the melt pools are clearly visible in these images. To ensure that the studied surfaces are aligned with the x-y plane, all samples were

carefully prepared and polished perpendicular to the building direction. Consequently, the observed melt pools on the surface of each sample were found to be parallel to each other side by side aligned with the laser scanning direction (instead of observing an oval or tear-dropped morphology of the melt pools having irregular geometries and directions reported in previous studies [32,36,96,97]). Sweeping of the surface by the laser accompanied by the 67° rotation of the laser scan between successive layers is clearly visible. Also, it is noticeable that decreasing the hatch distance from 0.21 mm in Regular sample to 0.13 mm and 0.12 mm in Surface 1 and Surface 2 samples, respectively, has resulted in the formation of more compacted melt pools, and contributed to the formation of a higher number of melt pools per unit area of the upskin surface (see Figure 4-3b and Figure 4-3c). Comparing the geometrical features of the successive passes in Surface 1 and Surface 2 samples revealed the variation of the melt pool width in a cyclic manner. It is unequivocally visible in Figure 4-3b and Figure 4-3c that the laser melting of the powders has formed one large melt pool followed by a smaller melt pool periodically. This change in the melt pools size was more evident in Surface 1 and Surface 2 samples than the Regular sample.

To further investigate the size of the upskin melt pools of all samples, the cross-sectional overview of the melt pools on the y-z planes were studied. Figure 4-4 shows the optical micrographs of the samples taken from the y-z plane. The micrograph from the Regular sample (Fig. 4a) illustrates an approximately consistent melt pool size for all upskin melt pools, as opposed to the Surface 1 (Figure 4-4b) and more clearly in Surface 2 (Figure 4-4c) samples, where repetitive combination of large-small melt pools has formed

the structure of the upskin layer. As the schematic in Figure 4-4d presents, having different size melt pools has resulted in the formation of a bi-layer structure in the upskin layer from the top view perspective. Therefore, by decreasing the hatch distance and increasing the overlap between the two consecutive passes, the size difference between two adjacent melt pools becomes more noticeable.

The schematic in Figure 4-5 can be used to better understand the mechanism of various melt pool size formations in Surface 2 (Figure 4-5a and Figure 4-5b), Surface 1 (Figure 4-5c), and Regular (Figure 4-5d) samples. To elucidate this phenomenon, it should be noted that when laser melts the first track, only the powder particles are exposed by the laser beam. Considering the separated nature of the powder particles, the main portion of the laser beam energy is used to melt and form a large melt pool, resulting in the formation of a large track following the completion of the solidification. Then, the laser is moved equal to the hatch distance to fuse the next layer. At this step, there are some overlaps between the newly formed melt pool and the previously solidified one, suggesting that a significant portion of the laser beam energy is dissipated through conduction and reflection from the previously solidified melt pool (see the schematic in Figure 4-5b, where the blue arrows correspond to the heat flow directions). Consequently, a smaller portion of the laser beam energy is used to melt the metal powders and form the new melt pool, resulting in the formation of a smaller melt pool (Figure 4-5b). For the next layer, since the hatching distance is still the same and small (the case of Surface 1 and Surface 2 samples), the previously formed small melt pool leaves more spacing for the powder particles to interact

with the laser beam, leading to the formation of a larger melt pool again (shown in Figure 4-5a and Figure 4-5c for Surface 2 and Surface 1 samples, respectively). This periodic formation of large and small melt pools occurs repeatedly until the completion of the upskin layer. Therefore, by decreasing the hatch distance and increasing the overlap between the two consecutive passes, the heat dissipation through the previously formed track increases contributing to a more noticeable size difference between the two adjacent melt pools. Contrarily, the increased hatch distance in the fabrication of the Regular sample and the resulted less overlaps of melt pools reduce the laser beam energy lost through the previously solidified track, and contributed to the minimum melt pool size difference between successive passes in the Regular sample (shown schematically in Figure 4-5d). Such cyclic variations of the melt pools' volume stemmed from using very small hatch distances in the fabrication of additively manufactured metallic components has never been reported in previous studies. This can potentially result in macro/micro-scale anisotropic properties of the structure, as the change in the melt pool size would directly impact the solidification behavior and consequently the resultant microstructure of the solidified tracks. Therefore, a detailed microstructural study of such a bi-layer structure is of vital importance.

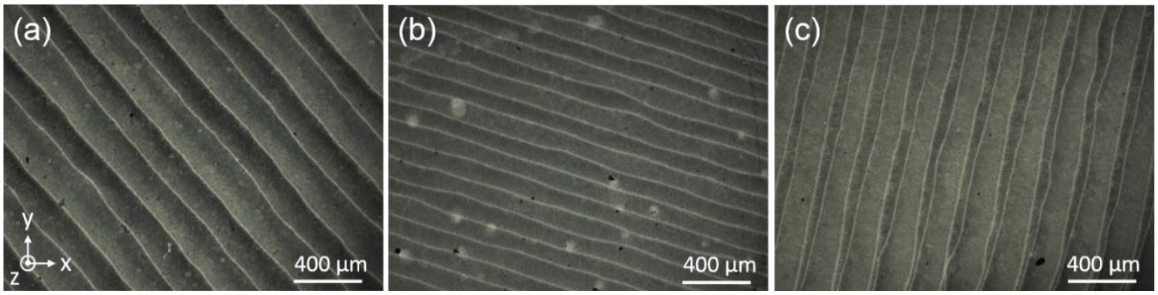

Figure 4-3: Optical micrographs taken from the top planes of the (a) Regular, (b) Surface 1, and (c) Surface 2 samples.

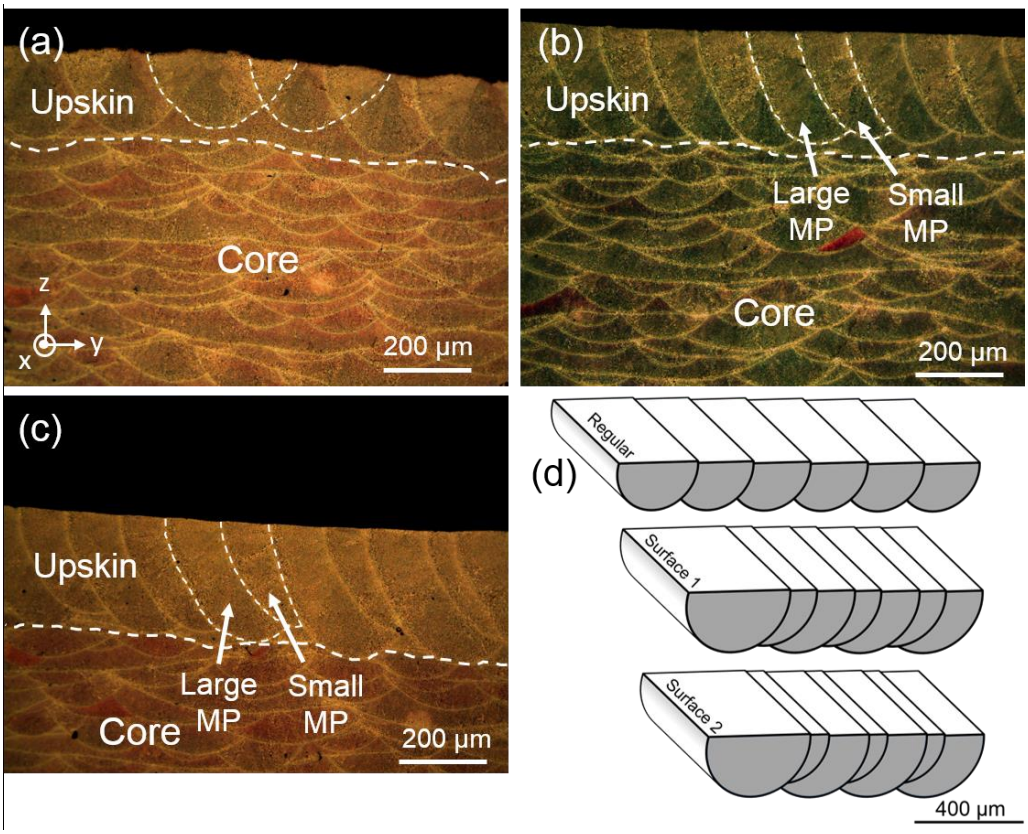

Figure 4-4: Optical microscopy images taken from the side view (y-z plane) of the (a) Regular, (b) Surface 1, and (c) Surface 2 samples, (d) the schematic model for all samples comparing the position and the geometries of the upskin melt pools relative to each other.

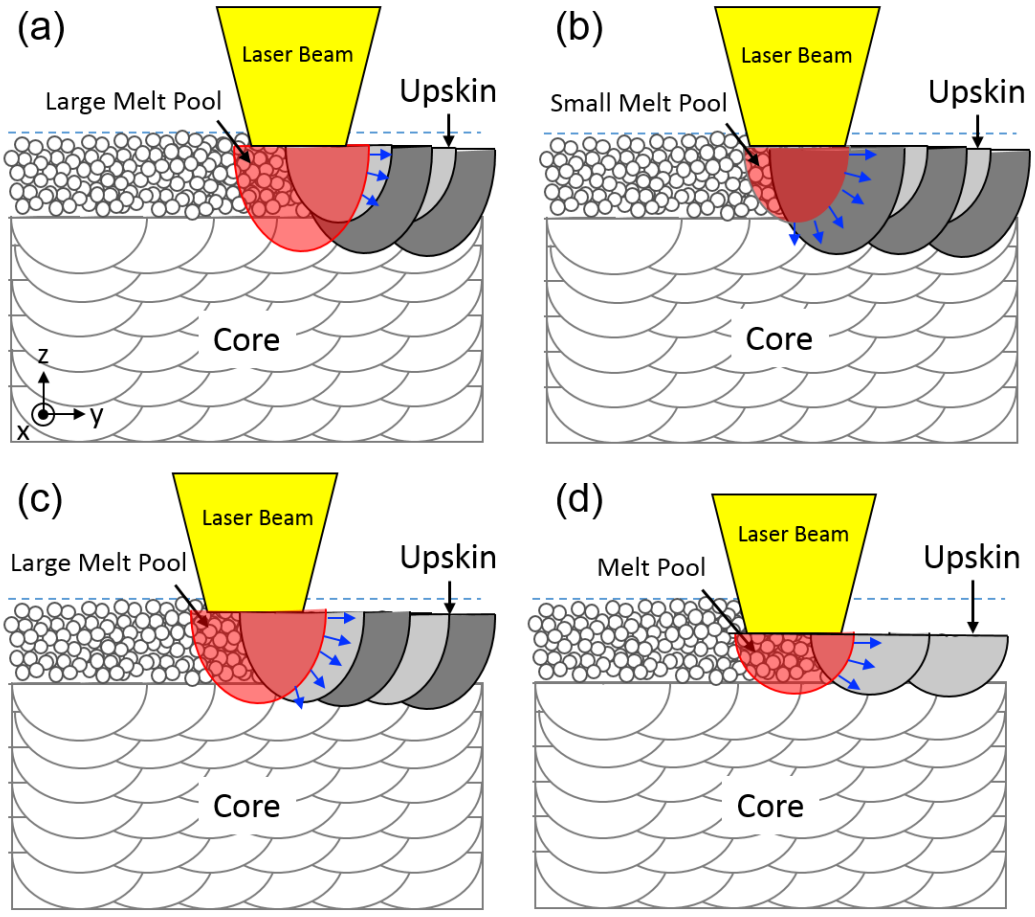

Figure 4-5: The schematic showing formation of various sizes of melt pools (MPs) in the upskin layer, (a) large MPs in Surface 2 sample, (b) small MPs in Surface 2 sample, (c) large MPs in Surface 1 sample, and (d) MPs in the Regular sample.

The detailed microstructural characteristics of all three surfaces are shown in the SEM micrographs presented in Figure 4-6 - Figure 4-9. The main similarity of all three samples is the formation of very fine cellular dendritic structure, which is common to all powder

bed fusion (PBF)-AlSi10Mg solidification structures [12,13,32,36,39,98]. Three different regions with distinct microstructures can be distinguished across each melt pool, *i.e*. region with fine cellular structure (MP-fine) formed towards the middle of the melt pool, regions having coarse cellular structure (MP-coarse) in the vicinity of each melt pool boundary, and a heat affected zone (HAZ) formed in the previously solidified layer containing broken intercellular network resulted from coarsening of Si phase into idiomorphic crystal [32,39]. A closer look into the SEM micrographs of the samples also reveals microstructural variations in terms of shape and size distribution of dendrites as well as the extension of each region. Considering co-existence of both large and small melt pools, particularly in Surface 1 and Surface 2 samples, the microstructure of the upskin layers were investigated and compared at two adjacent melt pools (different size melt pools) in each sample. A detailed image analysis of various SEM micrographs was conducted using ImageJ software to quantify the microstructural variations related to the Al cellular structure and the Si network for all samples. The aluminum matrix cell size (area) distribution of the upskin layers of different samples is presented in Figure 4-10, comparing the cell area (in μm^2) in the MP-coarse regions of large melt pools (Figure 4-10a), the MP-coarse regions of small melt pools (Figure 4-10b), the MP-fine regions of the large melt pools (Figure 4-10c), and the MP-fine regions of the small melt pools (Figure 4-10d). Table 4-5 also summarizes and compares different microstructural features of the two adjacent melt pools in the upskin layer of the Regular, Surface 1, and Surface 2 samples.

The SEM images taken from the melt pool boundaries of the Regular sample (Figure 4-6) and their corresponding MP-fine regions (shown in Figure 4-9a and Figure 4-9b) confirmed approximately the same morphology, size, and distribution of the Si network along the melt pool boundaries as well as the center of the two adjacent melt pools, *i.e.* MP1 and MP2. The average cell area in the MP-coarse regions of MP1 and MP2 (1.24±0.95 *vs* 1.21±0.90 μm^2, respectively), and in the MP-fine regions (0.36±0.19 *vs* 0.34±0.14 μm^2, respectively), the extend of MP-coarse region (14.23±0.81 *vs* 12.01±0.44 μm, respectively), as well as the HAZ (8.45±0.25 *vs* 6.66±0.49 μm, respectively) were found to be very similar between the two adjacent melt pools, which is associated to the formation of similar size melt pools in the fabrication of upskin layer in the Regular sample. In Surface 1 sample (Figure 4-7, Figure 4-9c, and Figure 4-9d), whilst the average cell size was slightly higher than the Regular sample (correlated to the higher *VED* used to fabricate this sample), their average width of MP-coarse regions were found to be very similar (14.23±0.81 and 15.16±0.76 μm, for Surface 1 and Regular samples, respectively). Likewise, the difference between the microstructure of the two adjacent melt pools in the Surface 1 sample (large and small MPs) was not that notable (refer to the data in Table 4-5).

In contrast, the MP boundaries of Surface 2 sample (Figure 4-8) revealed two distinct MP microstructure comprised a narrow MP-coarse region (10.63±0.39 μm wide) that belongs to the smaller melt pools and a wide MP-coarse region (22.18±0.69 μm wide) as part of the larger MP tracks. This coarse microstructure of large MP boundaries (both in

terms of the cell size and degree of Si network coarsening) was more noticeable in Surface 2 sample and was characterized by having a large average cell area of 2.35±1.55 μm^2 than that of the Surface 1 sample (average cell area: 1.44±1.20 μm^2). The coarser microstructure of the Surface 2 large MPs is correlated to the greater volume of the large MPs in this sample (see Fig. 4) as well as their smaller overlap with the previously solidified smaller tracks (see Figs. 4 and 5), which leads to a slower cooling rate during solidification of each MP. Analogously, the HAZ below the MP-coarse regions of the large MPs in Surface 2 sample was found to be more extended (10.31±0.72 μm wide), indicating that the smaller MPs have been exposed to high temperatures for a longer period of time during the solidification of larger MPs than their abutting large MPs with the HAZ width of 5.60±0.25 μm. Albeit the measured HAZ width of all samples followed a similar trend as the size of MP-coarse regions, the difference was not as notable as the width of the MP-coarse regions (see Table 4-5).

It is worth to mention that the microstructural features' size and the shape of a solidified structure is determined by the temperature gradient (G) and the solidification rate (R), as well as the undercooling (ΔT) [97,99]. The higher the cooling rate (product of G and R), the greater the undercooling (ΔT) is, leading to a finer structure. Therefore, the coarser microstructure of large melt pools in Surface 2 relative to the Regular and Surface 1 samples is ascribed to the lower cooling rate associated to the solidification of Surface 2 large melt pools. This applies to all regions from the melt pool center towards the melt pool boundaries. At the melt pool center, the material experiences the highest temperature

gradient (G) and the lowest solidification rate (R) (high G/R ratio), leading to formation of a more equiaxed dendritic structure [13,59]. Conversely, the fused material along the melt pool boundary undergoes the fastest solidification rate and lowest temperature gradient (low G/R ratio), contributing to the formation of a more columnar dendritic structure [13,59].

The average cell area of the Surface 1 sample seems to be slightly higher than that of the Regular sample. Nevertheless, comparing the size of the Si network formed at the intercellular regions of MP-coarse regions reveals a coarser (thicker) Si network for Regular sample (Figure 4-6b) than Surface 1 sample (Figure 4-7b). Therefore, comparing the MP-coarse regions of all samples corroborates the increase in the degree of Si network coarsening in the order of Surface 1 < Regular < Surface 2 samples.

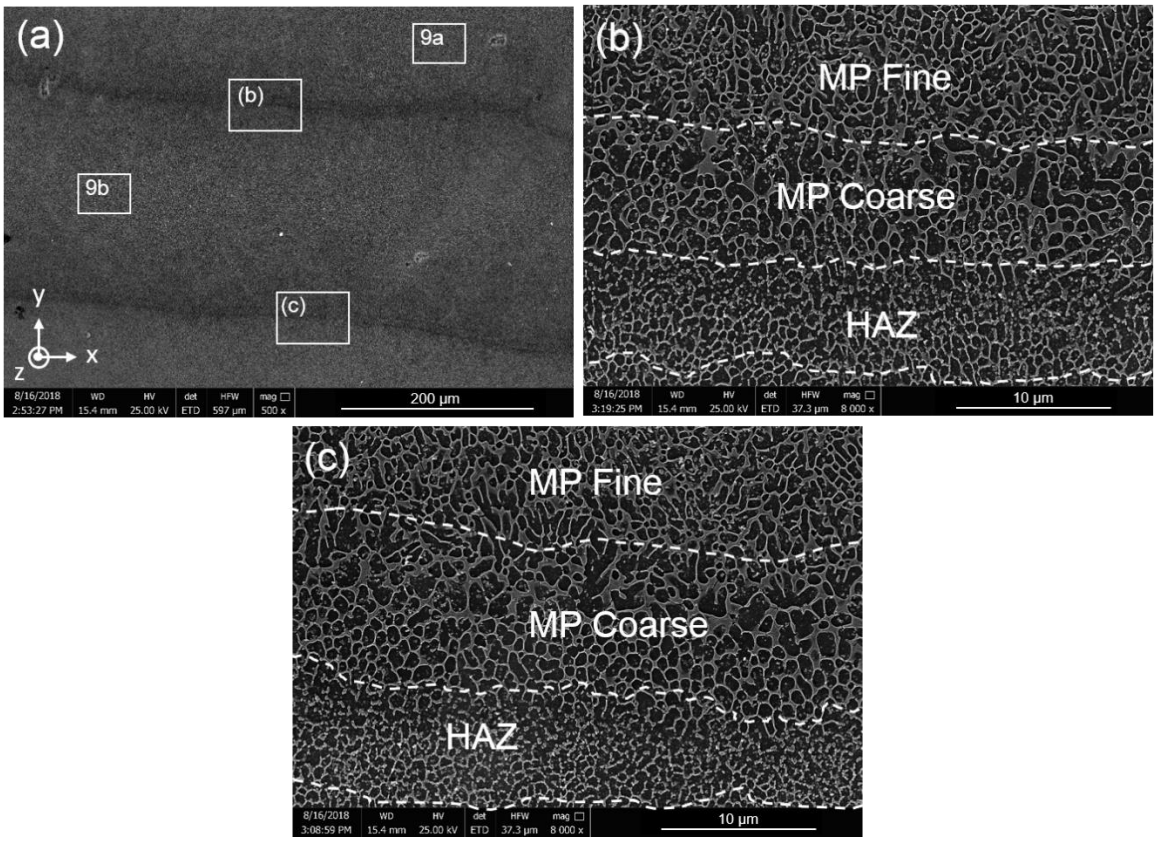

Figure 4-6: SEM micrographs showing the upskin microstructure of the Regular sample, (a) three adjacent melt pools and their boundaries are visible. Higher magnification image from the (b) top melt pool boundary (the enclosed area in (a) shown by (b)) and (c) bottom melt pool boundary (the enclosed area in (a) shown by (c)).

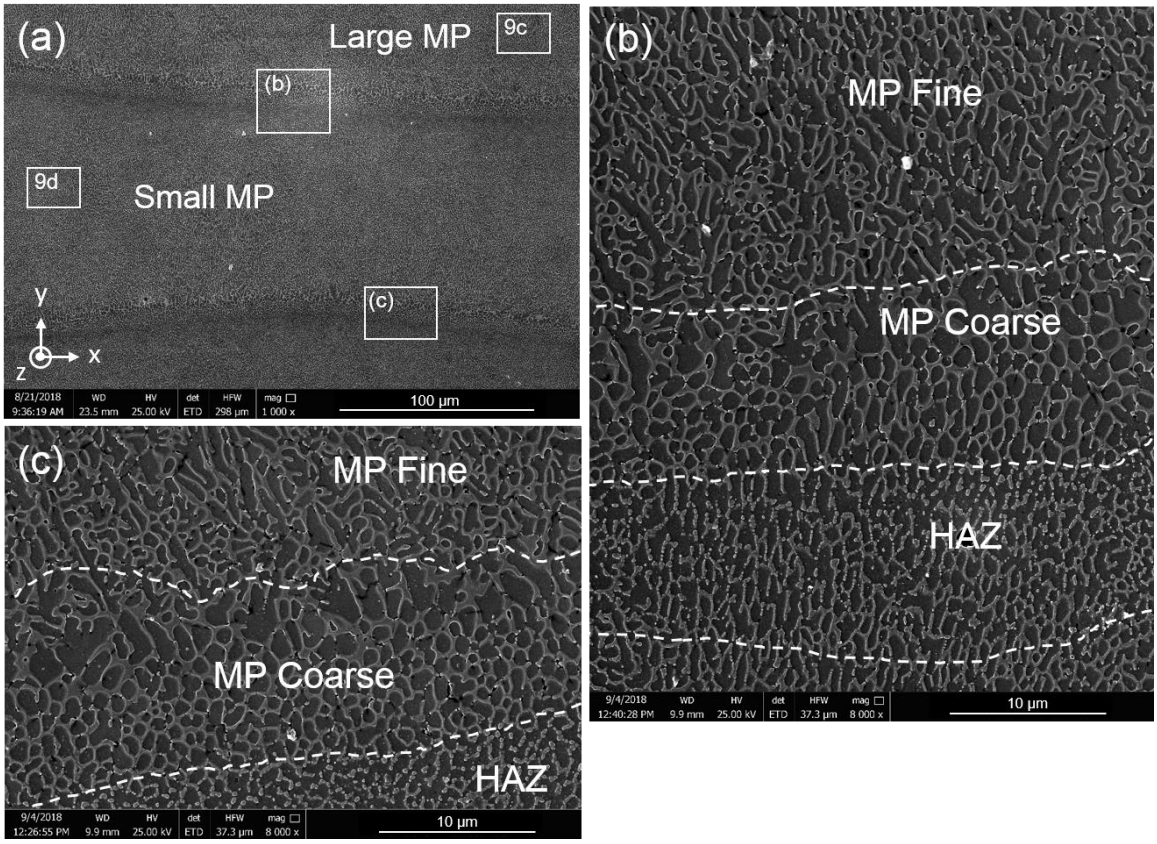

Figure 4-7: SEM micrographs showing the upskin microstructure of Surface 1 sample, (a) three adjacent melt pools and their boundaries are visible. Higher magnification image from the (b) top melt pool boundary (the enclosed area in (a) shown by (b)) and (c) bottom melt pool boundary (the enclosed area in (a) shown by (c)).

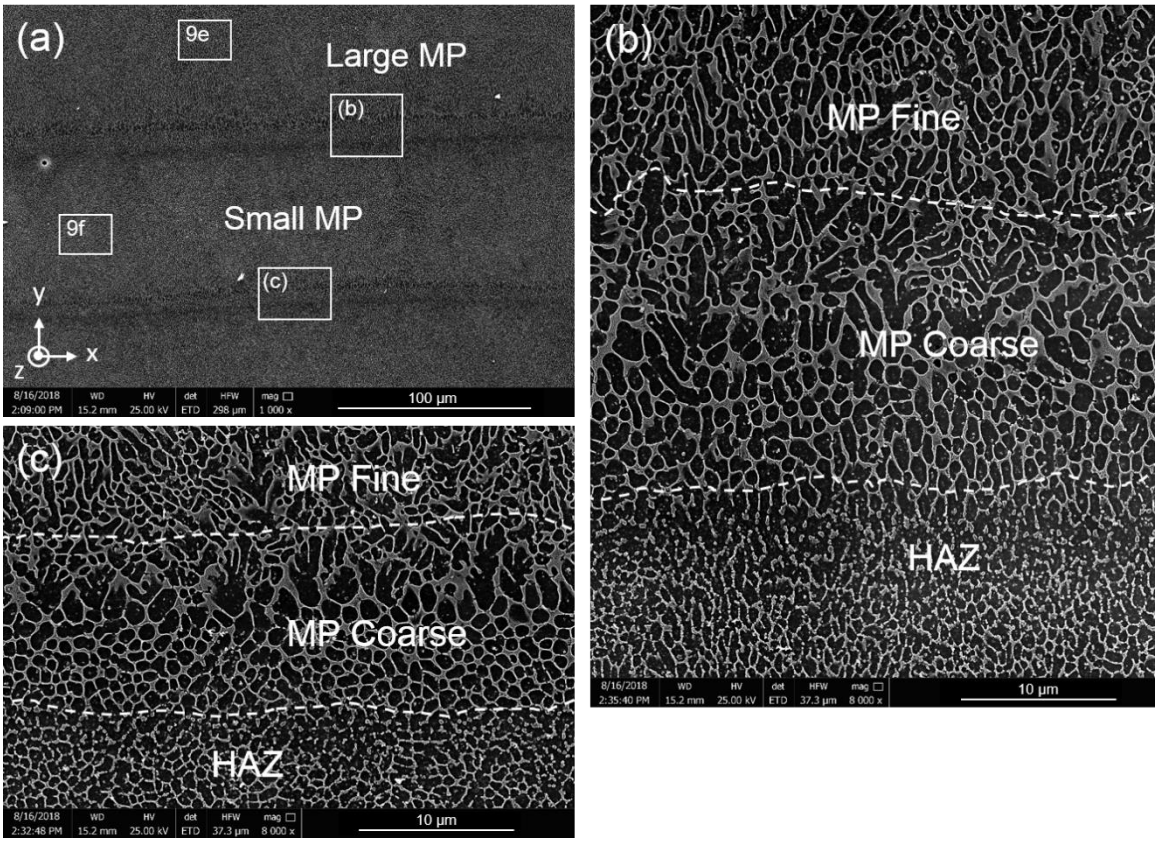

Figure 4-8: SEM micrographs showing the upskin microstructure of Surface 2 sample, (a) three adjacent melt pools and their boundaries are visible. Higher magnification image from the (b) top melt pool boundary (the enclosed area in (a) shown by (b)) and (c) bottom melt pool boundary (the enclosed area in (a) shown by (c)).

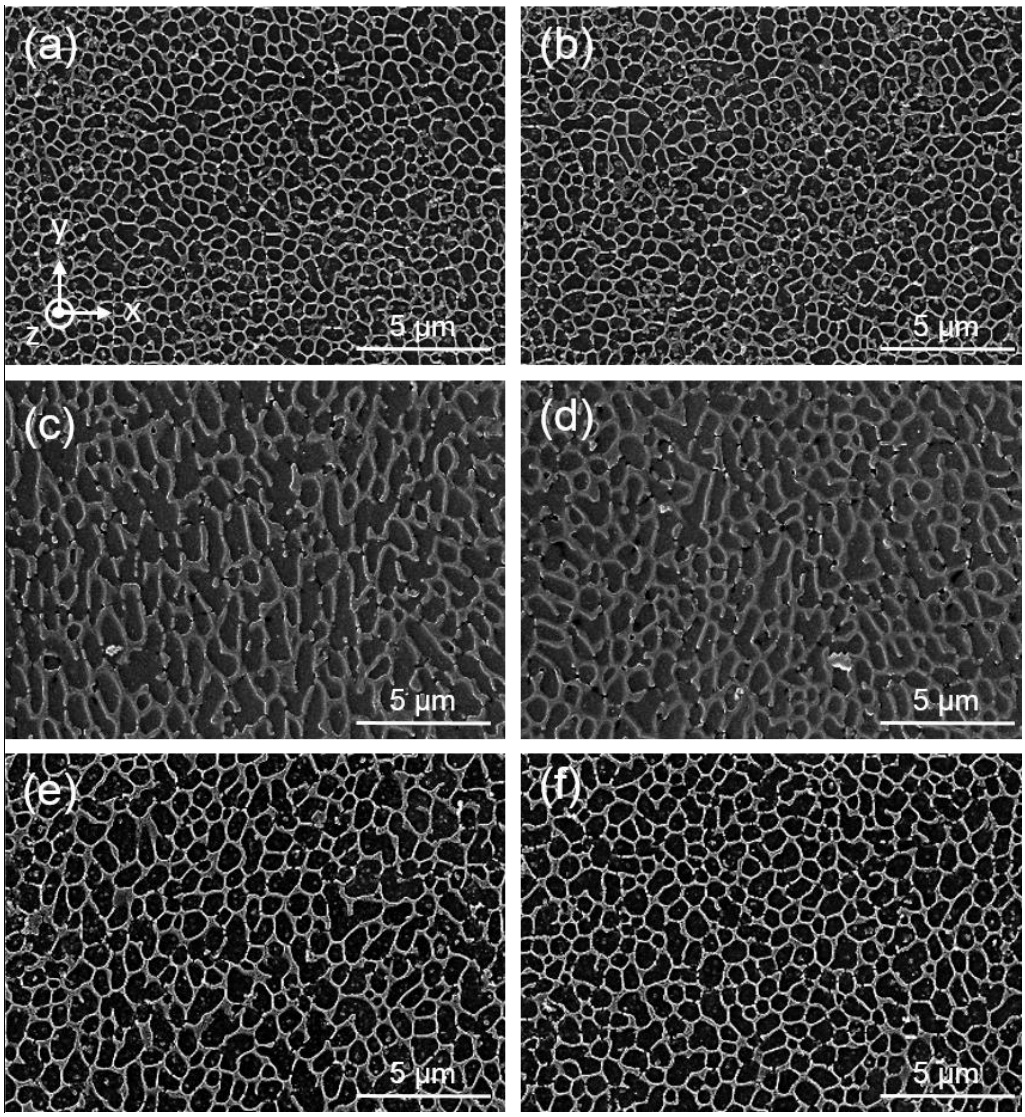

Figure 4-9: SEM images from the MP-fine regions of (a) and (b) two neighboring melt pools in Regular sample (higher magnification of the enclosed area shown by 9a and 9b in Figure 4-6a), (c) a large melt pool and (d) its adjacent small melt pool in Surface 1 sample (higher magnification of the enclosed area shown by 9c and 9d in Figure 4-7a), (e) a large melt pool and (f) its adjacent small melt pool in Surface 2 sample (higher magnification of the enclosed area shown by 9e and 9f in Figure 4-8a).

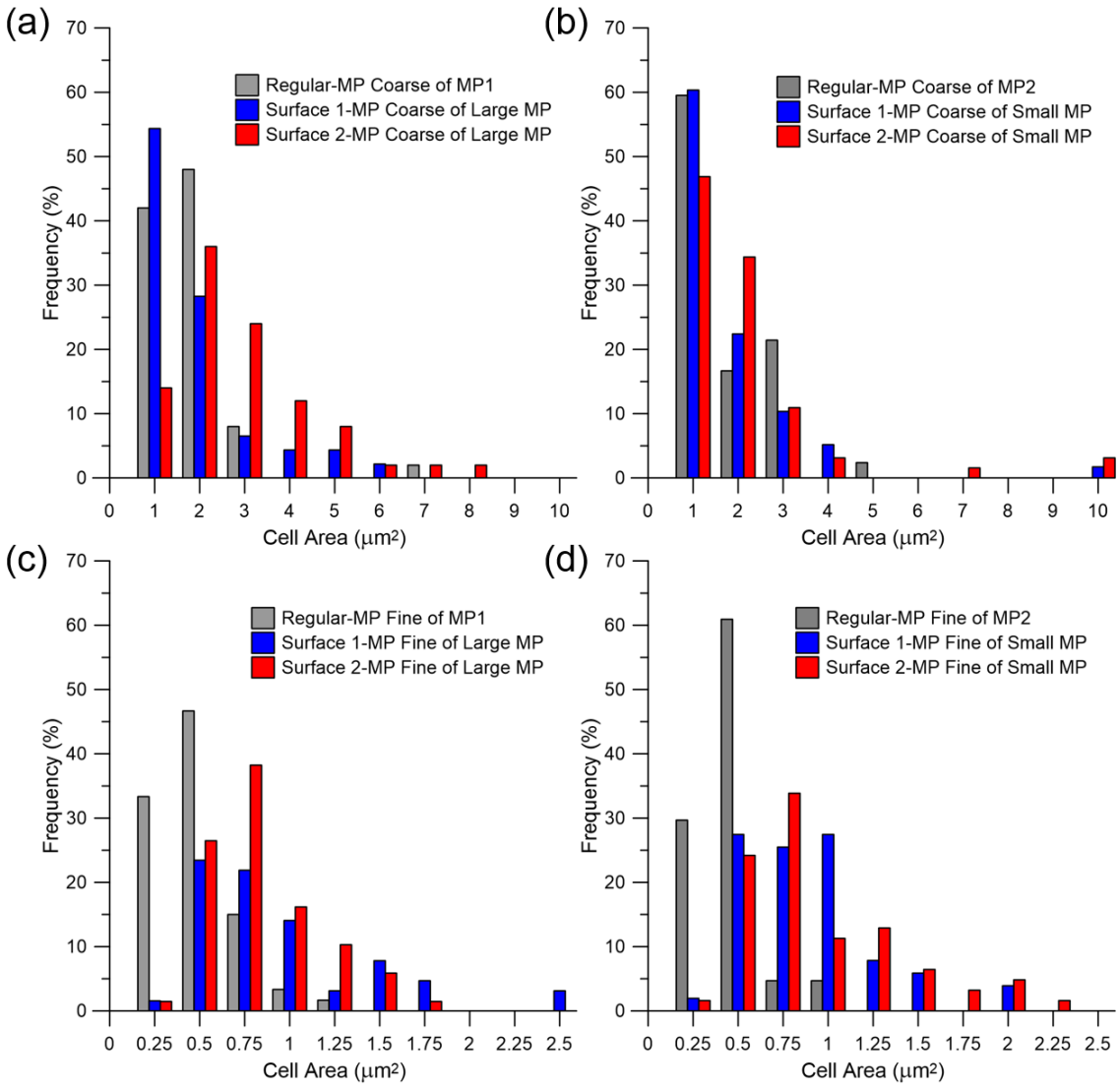

Figure 4-10: The size distribution of Al-matrix cellular structure (in area, μm^2) at different regions across the melt pool: (a) MP-coarse regions and (c) MP-fine regions of melt pool 1 (MP1) in the Regular, and large MPs in Surface 1 and 2 samples, (b) MP-coarse regions and (d) MP-fine regions of melt pool 2 (MP2) in the Regular, and small MPs in Surface 1 and 2 samples.

Table 4-5: Microstructural features of the upskin layers of the Regular, Surface 1, and Surface 2 samples.

Sample	Melt Pool Size	MP-coarse average cell area (μm^2)	MP-fine average cell area (μm^2)	MP-coarse width (μm)	HAZ width (μm)
Regular	MP1	1.26±0.95	0.36±0.19	14.23±0.81	8.45±0.25
	MP2	1.21±0.90	0.34±0.14	12.01±0.44	6.66±0.49
Surface 1	Large	1.44±1.20	0.86±0.64	15.16±0.76	9.60±0.88
	Small	1.31±1.24	0.80±0.49	13.76±1.05	7.78±0.52
Surface 2	Large	2.35±1.55	0.87±0.51	22.18±0.69	10.31±0.72
	Small	1.70±1.05	0.72±0.31	10.63±0.39	5.60±0.25

The XRD spectra obtained from the top surface of all three samples studied in this work is shown in Fig. 11. The results confirmed the existence of Si precipitates in the α–Al matrix. The Si diffraction peaks were found to be broad and weak, rendering a substantial proportion of Si content of the alloy is retained in α-Al supersaturated solid solution. Noticeably, the Si peaks for Surface 1 sample were found to be the weakest among the other samples, associated with having the highest Si content in the solid solution form in this sample. A closer look into the microstructure of the MP-coarse regions of all samples also affirmed higher concentration of Si atoms in solid solution form in the Surface 1 sample as evidenced by the lowest content of Si particles precipitated inside the Al dendrites and finer Si precipitates at the border of each dendrite in Surface 1 sample compared with the other two samples (shown in Figure 4-12).

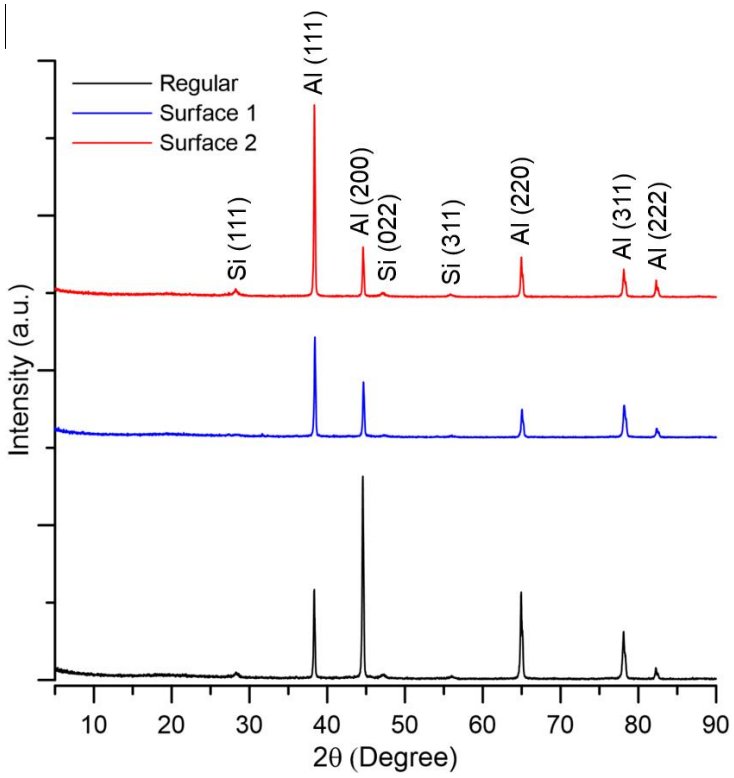

Figure 4-11: XRD patterns taken from the upskin layers of the Regular, Surface 1, and Surface 2 samples of DMLS-AlSi10Mg alloy.

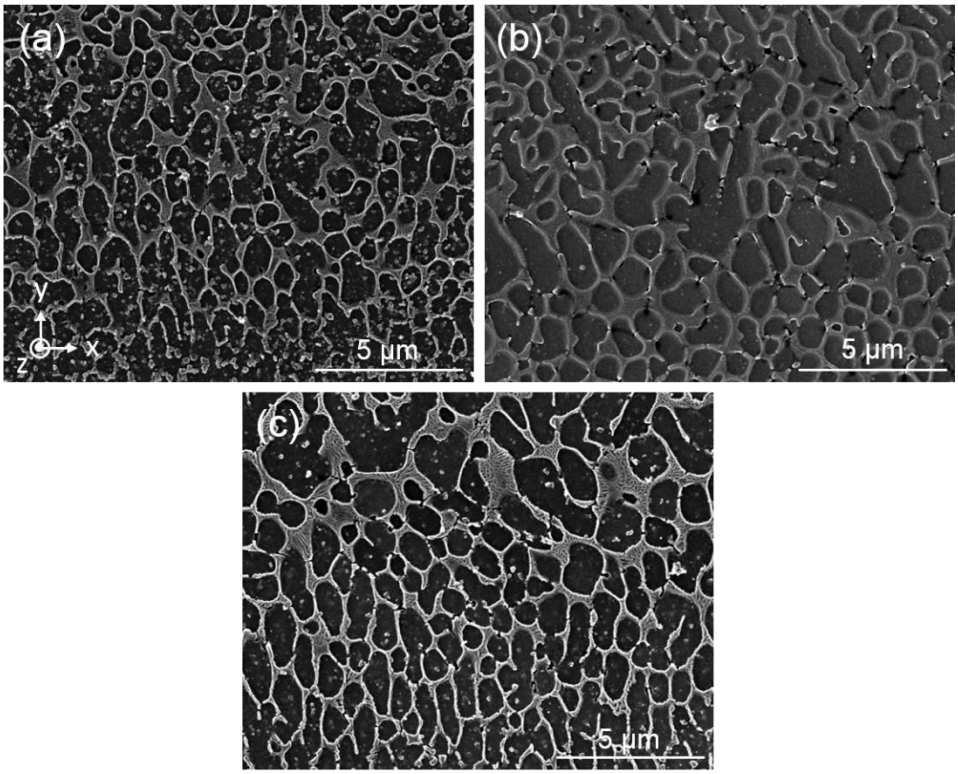

Figure 4-12: SEM micrographs taken from the MP-coarse regions of the (a) Regular, (b) Surface 1, and (c) Surface 2 samples.

To further investigate the initial microstructure of the samples, EBSD measurements from the upskin layer of all samples were performed in complementary to SEM and XRD. The obtained IPF maps, shown in Figure 4-13, are z-direction coloring maps (IPF-z), where z is aligned with the building direction of the upskin layer. The measured areas were focused on the large melt pool boundaries, covering an area that contains a large melt pool's MP-fine and MP-coarse regions as well as the HAZ in the previously deposited melt pool. The MP-coarse region was of particular interest, since this area was shown to be more

susceptible to selective corrosion attack in previous works [19–22,32,89]. Therefore, the reported results in this section represent localized characteristics of large melt pool boundaries and should not be extrapolated to the general characteristics of the upskin layer.

The coarse grain structure on the left side of the Regular sample (Figure 4-13a) or the top side of the Surface 1 and Surface 2 samples (Figure 4-13b and Figure 4-13c, respectively) corresponds to the previously deposited layer containing the heat affected zone adjacent to the melt pole boundary. The fine equiaxed or columnar grain structure shown on the right side or at the bottom of the inverse pole figures correlates to the interior of a large melt pool in each sample. The EBSD results taken from the melt pool boundaries of the samples show that the microstructure contains a combination of columnar and equiaxed grain structures with different volume fractions in different samples. Such microstructural variations form as a result of having different temperature gradients and solidification rate from the middle of the melt pool to its boundary [59]. The α-Al grains morphologies along the melt pool boundaries of the Regular and the boundaries of the large MPs of Surface 2 sample were found to vary in the sequence of very fine equiaxed grains and coarser columnar grains from the MP boundaries into the melt pools' center. The formed columnar grains directions are perpendicular to the melt pool boundaries, aligned with the maximum heat flow direction during solidification [13,15,98]. In comparison, Surface 1 grain structure (Figure 4-13b) showed noticeably lower volume fraction of such columnar grains than the other two samples.

Grain size distribution of the samples in the large melt pool areas shown in the IPFs in Figure 4-13 was measured to be 0.89±1.27, 0.79±0.90, and 0.95±1.44 µm for the Regular, Surface 1, and Surface 2 samples, respectively. This confirms that a finer and more uniformly distributed grain structure formed in the large MP of Surface 1 sample, possibly attributed to the faster solidification rate of the large melt pools in this sample. In comparison, the largest grain structure and the greatest deviation on the grain size distribution were detected for Surface 2 sample, resulted from a slower solidification rate of its large melt pools. Surface 2 also experienced the highest degree of grain coarsening in its HAZ, while the Surface 1 sample revealed the lowest amount of HAZ coarsening, affirming that the HAZ experiences the elevated temperature in a shorter period of time during solidification. This is another evidence of faster solidification of large MPs in the Surface 1 sample than that of the other two samples. Further elucidation of the grain structure variations for all samples is discussed at the end of this section.

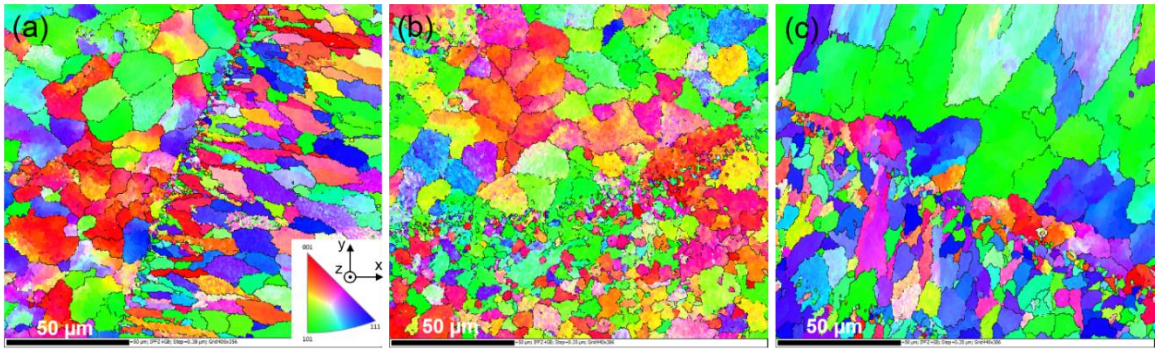

Figure 4-13: EBSD inversed pole figure (IPF-z) maps from the upskin layer of the (a) Regular, (b) Surface 1, and (c) Surface 2 samples.

To explore the micro-texture distribution arisen from the fabrication process of the larger melt pools of the upskin layers in each sample, pole figures of the melt pool microstructure in the area near the large MP boundaries were calculated from the EBSD maps. Figure 4-14 illustrates {100}, {110}, and {111} pole figures for the area below the HAZ in each large MP shown in Figure 4-13. The x and y directions are shown on the {100} pole figures and z is normal to the plane of the figure. As the PF maps demonstrate, {001}<100> cube texture is evident in the upskin layers of all samples. This texture plausibly corresponds to the epitaxial growth of the MP boundary crystals along the <001> direction, which is in good agreement with the observed solidification behavior of aluminum alloys in previous studies [11,13,97,100,101]. Among the three samples, Surface 2 PF showed the strongest texture intensity of 6.06. The slower solidification rate of the MP in Surface 2 sample has promoted the formation of columnar grains along the MP boundaries, which in turn has resulted in a strong texture in the {100} pole figure. It can be seen from the {100} PF of the Regular and Surface 2 samples that all three {100} poles are strongly aligned. Considering the direction of the MP boundaries relative to the x and y axes, one of the {100} poles is perpendicular to the direction of the MP boundary (parallel to the growth direction of the columnar grains), one is parallel to the MP large axes (laser scan direction), and one is normal to the surface of the sample.

Figure 4-14 also shows that the high-intensity regions in the pole figures of the Regular sample, indicating a higher intensity above the random background than that of Surface 1

sample (5.87 *vs* 4.88, respectively). Whilst the texture in the Regular sample is not as strong as that in the Surface 2 sample, the long axis of the columnar grains still appears to be aligned with the <100> direction.

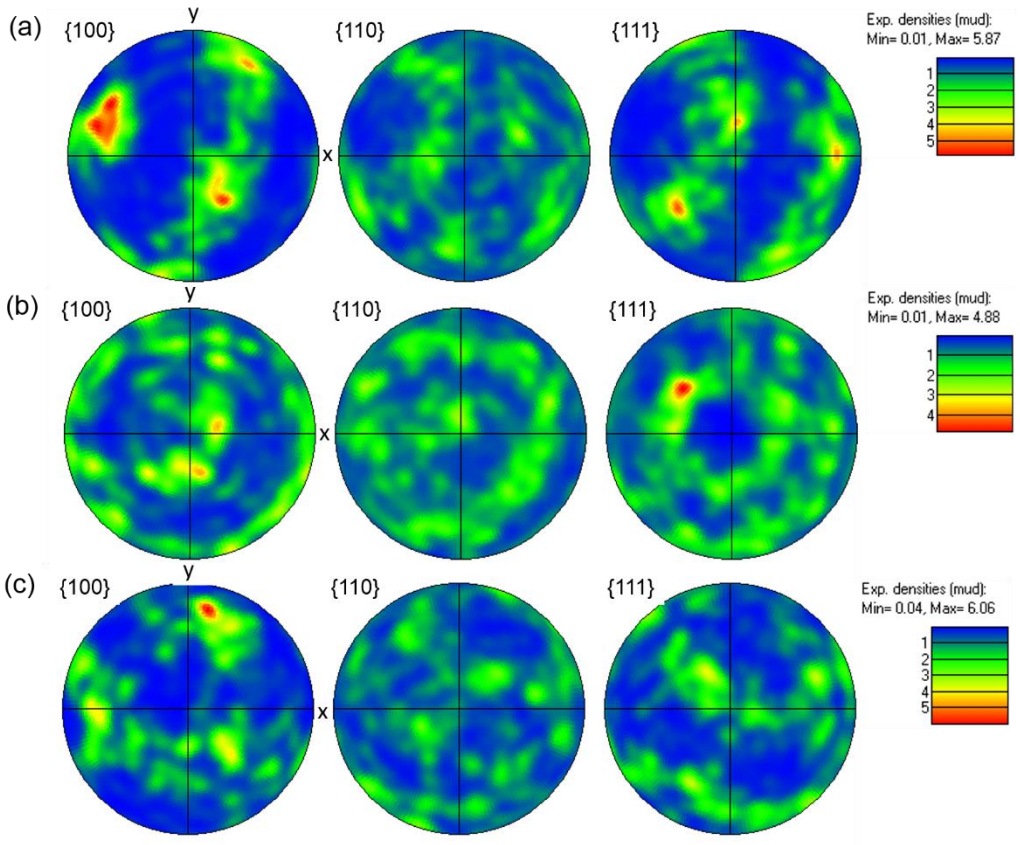

Figure 4-14: Pole figures (PF) from the large melt pools of the upskin layer of (a) the Regular, (b) Surface 1, and (c) Surface 2 samples.

To further rationalize the observed grain morphologies and sizes in Figure 4-13 and their corresponding pole figures shown in Figure 4-14 for all samples, the solidification

behavior of the melt pools in each sample should be contemplated. It is generally accepted that the MP grain structures near the MP boundaries are dominated by the epitaxial growth, implying that in a competitive growth process, aluminum FCC crystals with <100> direction (easy growth direction for cubic structures [13,15,102]) perpendicular to the MP boundary (direction of maximum heat flow) would grow more readily than the other oriented crystals. Consequently, the other oriented grains are stifled with the <100> oriented ones and form a narrow band of very fine equiaxed grains grown from each MP boundary (see Figure 4-13).

The two key parameters that determine the microstructure of aluminum grains in each melt pool after solidification are thermal gradient (G) and the solidification rate (R) [59]. The melt pool boundaries of the Regular sample (fabricated using the lowest *VED* of 57.1 J/mm^3) showed a high volume fraction of columnar grains. Increasing the applied laser energy density to 122.4 J/mm^3 to fabricate the Surface 1 upskin layer has contributed to the formation of more equiaxed crystals in its melt pools by providing longer time for the nucleus to grow, owing to the decreased temperature gradient (G), while increased overlapping between Surface 1 melt pools provides a faster cooling and higher solidification rate (R). Therefore, the G/R ratio decreases and the constitutional supercooling increases in the front of the moving solid-liquid interface [59,83] from the Regular to Surface 1 sample, resulting in the transition from columnar (in the Regular sample) to a more equiaxed grain structure (in Surface 1 sample). The displayed melt pools for Surface 2 sample in Figure 4-13c correspond to a large MP adjacent to a smaller one.

Comparing the cross sectional overview of the melt pools in Figure 4-4 and the schematic shown in Figure 4-5 clearly show that the overlapped area between a large and a small MP in Surface 2 sample is smaller than that between the MPs in Surface 1. The smaller overlap between the large and small melt pools in the Surface 2 sample has contributed to a slower solidification rate for its large melt pools. This explains the reason that the columnar grains commenced to form again in the large MP boundaries of Surface 2 sample.

As the columnar crystals form by epitaxial growth, the higher ratio of columnar grains in the Surface 2 sample has contributed to the observed stronger cube texture ({001}<100>) in the large melt pools of the upskin layer of this sample compared with the other two samples. Surface 1 sample showed the weakest texture and the Regular sample showed an intermediate texture, consistent with the expected trend in their solidification rate.

Open Circuit Potential (OCP) Variations

To evaluate the thermodynamic tendency of the samples' upskin surfaces to electrochemical oxidation, the evolution of the corrosion potential (E_{OCP} values) was monitored prior to conducting other electrochemical tests during early stage of immersion in aerated 3.5 wt.% NaCl solution. The measurements were repeated for at least 5 times for each sample to ensure that the results are reproducible. It is well understood that a more positive E_{OCP} value signifies a nobler surface and a greater stability [103–105]. As shown in Figure 4-15, the E_{OCP} of all samples decreases slightly by time, indicating that the

electrochemical reaction in naturally-aerated NaCl solution is controlled by the cathodic reaction (oxygen diffusion) and the pre-existing oxide film on the samples' surfaces initially commence to dissolve into the electrolyte [70,71]. After a certain immersion time (~ 350 s for the Regular sample and ~ 800 s for the Surface 1 and 2 samples), the E_{OCP} value eventually stabilizes and approaches a stable value (~ -0.62 ± 0.05 $V_{Ag/AgCl}$, -0.52 ± 0.02 $V_{Ag/AgCl}$, and -0.73 ± 0.03 $V_{Ag/AgCl}$ for the Regular, Surface 1, and Surface 2 samples, respectively), associated to the stabilization of the passive film on the sample's surface. A common phenomenon during immersion of a metal in a corrosive electrolyte is the continuous formation of an oxide film on its surface and dissolution of this film in a competitive manner. This simultaneous localized dissolution and re-formation of the passive film on the surface can cause electrochemical instability of the surface, consequently contributing to the fluctuation of the open circuit potential values [105]. In comparison to Surface 1 and Surface 2 samples, the Regular sample showed the most unstable E_{OCP}, possibly owing to its higher surface roughness. Therefore, the trend and values of all samples' E_{OCP} imply the highest passive film stability for Surface 1 and the lowest stability for Surface 2 sample.

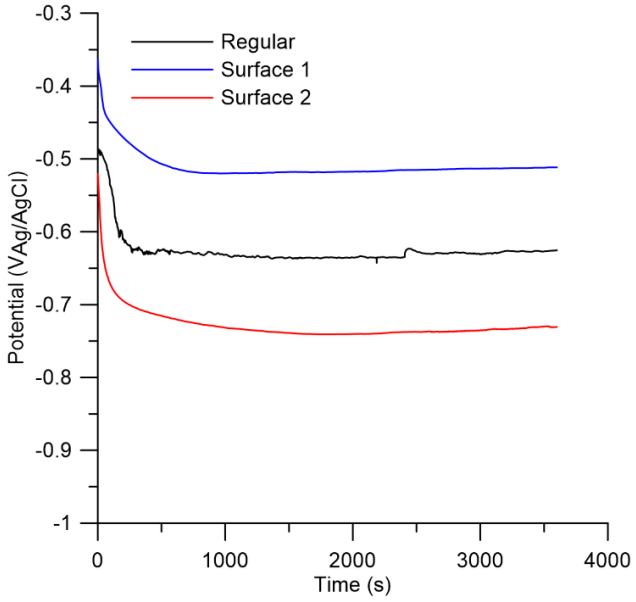

Figure 4-15: Open circuit potential values as a function of time for the Regular, Surface 1, and Surface 2 samples in aerated 3.5 wt.% NaCl solution at 25 °C.

Cyclic Polarization Results

To study the electrochemical behavior of all three samples, both anodic potentiodynamic polarization (APP) and cyclic potentiodynamic polarization (CPP) tests were conducted and the results are shown in Figs. 16a and 16b, respectively. The electrochemical parameters deducted from the polarization graphs of all samples are presented in Table 6. Before each polarization testing, to allow stabilization of the test, OCP was monitored for 1 hr after immersion in aerated electrolyte. The anodic polarization graphs (Figure 4-16a) showed a clear shift of corrosion potential towards more positive (nobler) values in the order of Surface 2 ($E_{corr.}$= -0.68±0.08 $V_{Ag/AgCl}$) < Regular ($E_{corr.}$= -0.58±0.05 $V_{Ag/AgCl}$) <

Surface 1 ($E_{corr.}$= -0.51±0.04 $V_{Ag/AgCl}$), corresponding to the highest tendency for corrosion reactions to initiate in Surface 2. Meanwhile, the corrosion current density ($I_{corr.}$) increases in the order of Surface 1 < Regular < Surface 2. Collectively, a clear passive window (although very narrow for Surface 2 sample), upper limited by the E_{pit} (pitting potential, also known as passive film breakdown potential) was readily discernible, occurring at -0.14±0.06 $V_{Ag/AgCl}$, -0.38±0.10 $V_{Ag/AgCl}$, and -0.62±0.08 $V_{Ag/AgCl}$, for Surface 1, Regular, and Surface 2 samples, respectively. This indicates a low likelihood for pit nucleation and a favorable condition for the surface repassivation in Surface 1 sample with the widest passive region ($E_{corr.}$ + 0.37 $V_{Ag/AgCl}$). The steeper anodic slope of the Surface 1 sample likewise indicates a greater passivation tendency for this sample than the other two samples. The variations of the pitting potential values also confirmed the existence of a passive film with different chemical compositions on different samples, as the pitting potential is only dictated by the passive film composition [47,106]. In the case of Surface 2 sample, the anodic current density rapidly increases slightly above the pitting potential, implying the highest susceptibility of Surface 2 sample to stable pits formation in the tested electrolyte.

For all samples, the repassivation potential ($E_{rep.}$) was found to be lower than the corrosion potential ($E_{corr.}$), confirming the existence of a favorable condition for stable pit growth on all surfaces. The $E_{rep.}$ values (Figure 4-16b) remained relatively unchanged and was similar for all samples (-0.84 ± 0.05 $V_{Ag/AgCl}$).

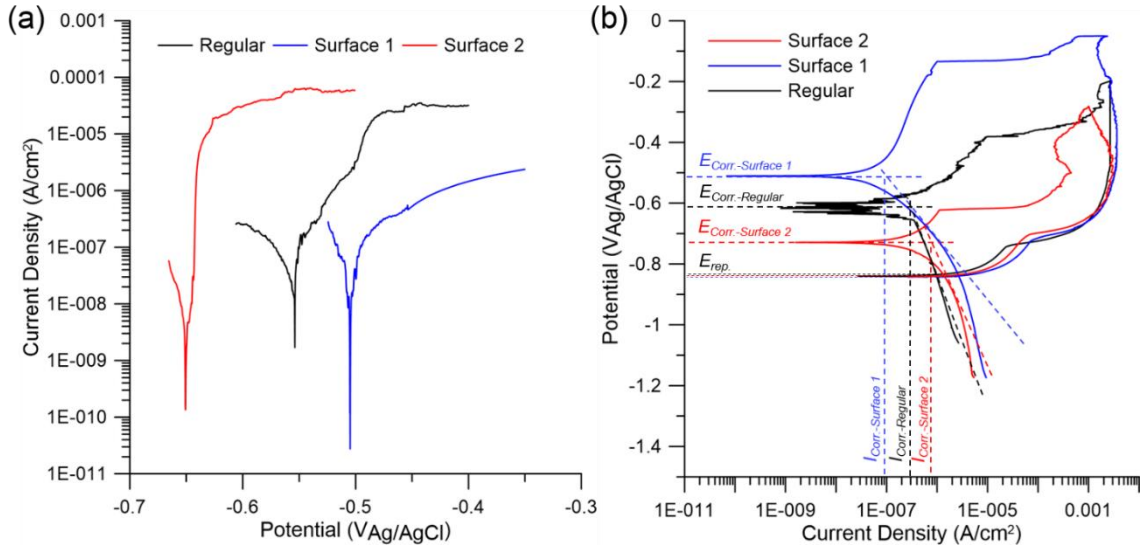

Figure 4-16: (a) The anodic potentiodynamic polarization curves and (b) the cyclic polarization curves of the Regular, Surface 1, and Surface 2 samples in aerated 3.5 wt.% NaCl solution.

Table 4-6: Polarization parameters deducted from upskin layer of Regular, Surface 1, and Surface 2 samples in aerated 3.5 wt.% NaCl solution

Sample	Corrosion potential ($V_{Ag/AgCl}$)	Pitting potential ($V_{Ag/AgCl}$)	Repassivation potential ($V_{Ag/AgCl}$)	Polarization resistance (KΩ)	Corrosion current density (A/cm^2)
Regular	-0.58 ± 0.05	-0.38 ± 0.10	-0.83 ± 0.05	934.4 ± 77.2	27.08 ± 1.49 $\times 10^{-8}$
Surface 1	-0.51 ± 0.04	-0.14 ± 0.06	-0.84 ± 0.04	5039 ± 470.8	8.26 ± 2.17 $\times 10^{-8}$
Surface 2	-0.68 ± 0.08	-0.62 ± 0.08	-0.84 ± 0.05	620.8 ± 40.7	53.34 ± 3.52 $\times 10^{-8}$

Corrosion Morphology

Figure 4-17 shows the surface morphology of the samples after cyclic potentiodynamic polarization testing followed by corrosion product removal. All surfaces showed a similar selective corrosion attack along the melt pool boundaries on the surface, where is known to be susceptible to penetrating corrosion attack on the surface of DMLS-AlSi10Mg alloy. This is ascribed to the coarsening and breakage of the Si network in the MP-coarse region and the heat affected zone, respectively, in the vicinity of each melt pool boundary [21,22,32]. A qualitative comparison of the corroded surfaces confirmed the increased intensity of the corrosion attack from Surface 1 sample to Regular, and Surface 2, clearly not in agreement with the trend of the surface roughness. However, this observation is consistent with the presented APP and CPP results in the previous section (Figure 2-16), but in contrast with the generally known effect of surface roughness on corrosion behavior [22,107]. Thus, there should be other factors than the surface roughness that control the electrochemical behavior of the samples herein.

Although the surface morphology of the samples after CPP testing revealed very intense corrosion attack along the MP boundaries of Surface 2 sample, whereas the Regular and Surface 1 samples were attacked selectively in similar locations but in lesser degree, it was not possible to identify a clear difference between corrosion of large and small MP boundaries, mainly due to the severity of the CPP testing. Therefore, performing the APP testing and investigating the morphological features of the corroded surfaces were required to discern the materials degradation along small and large MP boundaries, particularly for

Surface 2 sample. As the SEM images in Figure 4-18 illustrate, the anodic polarization testing of all samples resulted in localized pitting (typical of Al alloys [47]) of the surface of the samples primarily along the melt pool boundaries (indicated by the arrows). As shown in Figure 4-18a, the melt pool tracks on the Regular sample are not as clearly visible as the other two samples, owing to the higher surface roughness and existence of partially melted powder on its surface. A qualitative comparison of all three surfaces after the anodic polarization testing reveals a more intense pitting attack (the highest number of the pits per unit length of each melt pool boundary) along the MP boundaries of the Surface 2 sample than the other two samples at the start of the corrosion. The pitting then develops into a more severe selective corrosion attack along the MP boundaries as corrosion progresses (see Figure 4-17c), attributed to the growth and coalescence of the corrosion pits. Even though no clear difference was evidenced between the two adjacent melt pools in the Regular (Figure 4-18a) and Surface 1 (Figure 4-18b) samples, Surface 2 sample (Figure 4-18c) revealed a higher number of pits along the MP boundaries shown by the red arrows (correlated to the MP boundaries of the large MPs), while the boundaries depicted by the blue arrows were characterized by having less number of pits per unit length of the MP boundary (corresponding to the MP boundaries of the small MPs). Therefore, a higher pitting susceptibility of the large MP boundaries of Surface 2 sample was evidenced from the corroded surfaces after performing the anodic polarization testing.

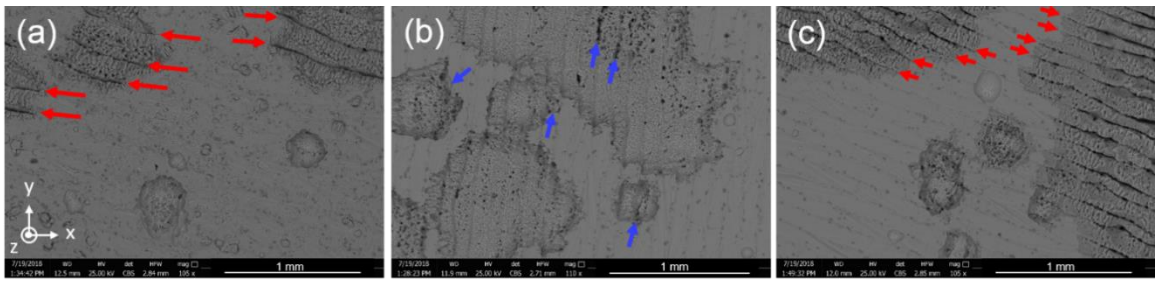

Figure 4-17: SEM micrographs of the upskin layers (x-y plane) after the CPP test and removing the corrosion products: (a) and (b) Regular, (c) and (d) Surface 1, and (e) and (f) Surface 2 samples.

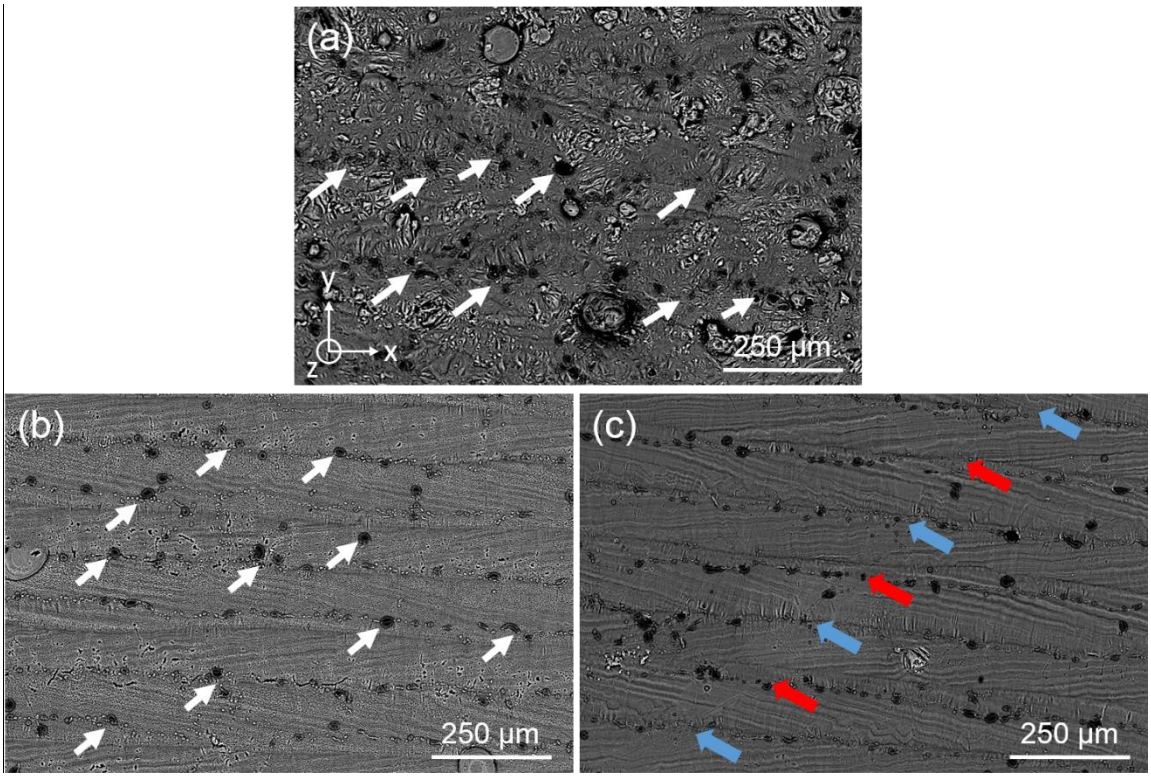

Figure 4-18: SEM micrographs of the upskin layers (x-y plane) after the anodic polarization test: (a) Regular, (b) Surface 1, and (c) Surface 2 samples.

EIS Results

To further study the electrochemical performance of the DMLS-AlSi10Mg alloys with different upskin structures, the EIS measurements in aerated 3.5 wt.% NaCl solution were carried out. The corresponding Bode plots and Nyquist plots of all samples for immersion times ranging from the initial immersion to 96 hr every 24 hr are presented in Figure 4-19a to Figure 4-19e. To analyze the characteristics of the passive film formed on all DMLS-AlSi10Mg samples and to interpret the electrochemical response of the system using the EIS data, the equivalent electric circuits (EECs) shown in Figure 4-19f with two or three time constants, expressing as $R_s((CPE_p[CPE_{dl}R_{ct})R_p])$ and $R_s(CPE_{oxide}[R_{oxide}((CPE_p[CPE_{dl}R_{ct})R_p]]))$, denoted by Model I and Model II, respectively, (commonly employed for Al alloys [108,109]) were used to represent the DMLS-AlSi10Mg alloy/electrolyte interface. These EEC models include solution resistance (R_s), passive layer resistance (R_p) in parallel with its constant phase element (CPE_p), describing its porous nature, charge transfer resistance (corroding pit resistance) (R_{ct}) parallel to the capacitor CPE_{dl}, describing double layer (*dl*) charging-discharging at the alloy's surface. The second model in Figure 4-19f also contains an extra constant phase element and a resistor in parallel (CPE_{oxide} and R_{oxide}, respectively), corresponding to a newly formed oxide layer with a porous nature on the substrate surface. The use of *CPE* is justified by the non-ideal capacitive behavior of heterogeneous interfaces. The impedance of the constant phase element is expressed as $Z_{CPE} = Y_o^{-1}(j\omega)^{-n}$, where Y_o is true capacitance of the passive layer, ω is the angular frequency (rad/s), j is the imaginary unit ($j = \sqrt{-1}$) and

n represents the exponent of the constant phase element and varies between 0 (for pure resistor) and 1 (for pure capacitor) [71,109]. Table 7 summarizes the fitting results of the EIS data. Figure 4-19 also shows the fitting of EIS data resulted from the application of the proposed equivalent circuits (either Model I or II) in Figure 4-19f to the obtained experimental data. The resulted *CPE* exponent values close to 1 (shown in Table 4-7) indicate a near capacitive behavior of the passive film formed on the surface of all DMLS-AlSi10Mg samples, regardless of the their surface roughness.

The impedance response of all three samples at all times is typical of localized corrosion of Al alloys [73,81]. At initial immersion time up to 48 hr, the phase angle *vs* frequency Bode diagrams of all three samples highlighted three time constants as follows. The first one at low frequency (0.01 Hz), associated to the charge transfer resistance arisen from anodic dissolution of aluminum as well as pitting of the surface. The second one at medium frequency range (10-100 Hz), corresponding to the formation of passive layer (aluminum oxide/aluminum hydroxide); and another one at high frequency (0.3-10 kHz), representing formation of an outer oxide layer in contact with the electrolyte, which can further contribute to the protection of the underlying layer. Correspondingly, three capacitive arcs on the Nyquist plots were generated, one at low, one at mid, and the other at high-frequency range. On the Nyquist plots, the tail at lower frequency determines the diffusion through the passive layer (corrosion product) and inside the localized corroded areas, whereas the peak (capacitive loop) at mid-frequency can result from the sealing effect of the corrosion film (passive layer) in active areas, such as surface porosities. In the

course of immersion, both the tail and the capacitive loops were the largest for Surface 1 sample, followed by Regular samples, while the Surface 2 sample exhibited a noticeably smaller capacitive loop, attributed to the existence of a passive film with less protective nature on its surface.

At the beginning of immersion in the electrolyte solution, Surface 1 sample showed the highest absolute value of impedance ($|Z|$ Ωcm^2) and the largest capacitive arcs, compared to the other two samples in the low to mid frequency ranges. This has contributed to a higher passive layer resistivity (R_p = 17.80 $k\Omega cm^2$) and charge transfer resistivity (R_{ct} = 36.50 $k\Omega cm^2$) for Surface 1 sample than those of the other two samples. The observed superior impedance of the Surface 1 sample in just immersed condition is also consistent with the polarization results (Figure 4-16). The lowest R_{oxide}, R_p, and R_{ct} values (0.27, 10.70 and 12.40 $k\Omega cm^2$, respectively) for Surface 2 sample confirmed the lowest resistivity of the protective oxide layer(s) on its surface, which is in good agreement with the polarization results (Figure 4-16). In all immersion times, Surface 2 sample showed the lowest R_p and R_{ct} values than the other two samples, while Surface 1 showed the highest resistivity.

Longer immersion time for all samples increases the susceptibility of the alloy to both general corrosion and pitting attacks as evident from the drops in R_{oxide}, R_p and R_{ct} values up to 72 hr. This is attributed to general removal and dissolution of the passive film from the surface and the exposure of the next cathodic site (Si particles) to the electrolyte. This reduction rate in R_p and R_{ct} values of the Surface 1 sample is lower (they reached a value

of 19.70 and 21.20 $k\Omega cm^2$, respectively, after 48 hr) than the other two samples, which is another compelling evidence for the formation of a more stable and compact passive layer, providing a better protection against both pitting and uniform corrosion attacks for Surface 1 sample than the other two samples. For Surface 2 sample, all *R* values dropped significantly right after the first day of immersion and remained almost constant up to 96 hr. In contrast, in the Regular and Surface 1 samples, R_{oxide}, R_p, and R_{ct} values were raised by increasing the exposure time from 72 hr to 96 hr, possibly correlated to the detachment of cathodic sites (Si particles) from the anodic matrix as the matrix around the particles oxidizes. This elimination of cathodic sites can slow down the growth rate of some of the growing pits as the corrosion reaction progresses. This improvement was not detected for Surface 2 sample even after 96 hr of immersion time, possibly ascribed to having coarser Si network and particles along its large melt pool boundaries (see Figure 4-12), which require longer immersion times in the electrolyte solution to detach.

For all DMLS-AlSi10Mg samples during the first 48 hr or 72 hr of immersion, the charge transfer resistance (R_{ct}) was found to be higher than the general passive/oxide layer resistance (sum of R_p and R_{oxide} values), confirming that the corrosion behavior is initially dominated by general uniform corrosion and metastable pitting of the surface than a stable pitting attack. This difference is more noticeable for Surface 1 sample at initial immersion time than the other two samples, affirming the observed wider passive region on the cyclic polarization curve of this sample (shown in Figure 4-16b).

Therefore, the EIS results confirmed that a more stable and compact passive layer exists on Surface 1, providing a better resistance against corrosion as compared to the Regular and Surface 2 samples.

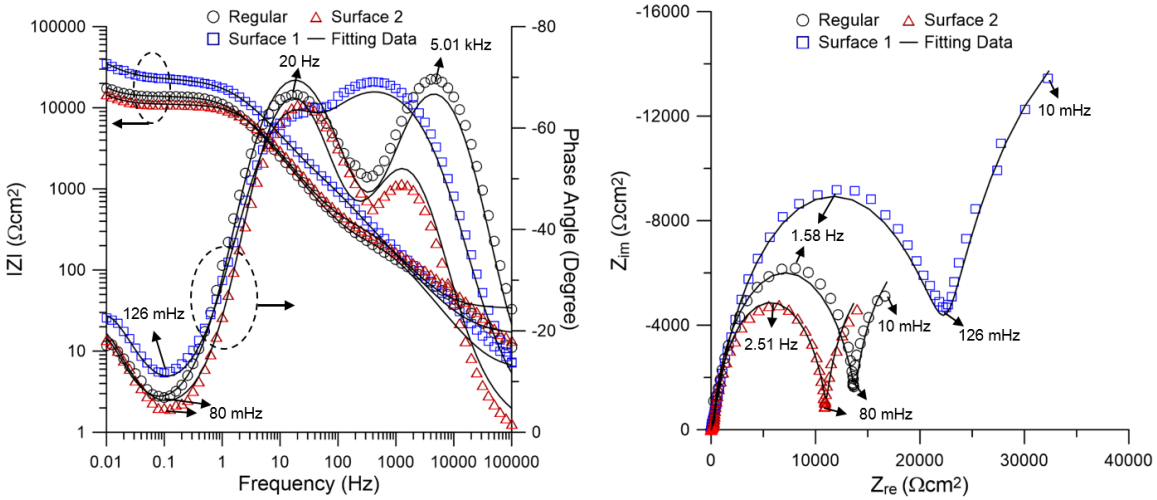

(a)

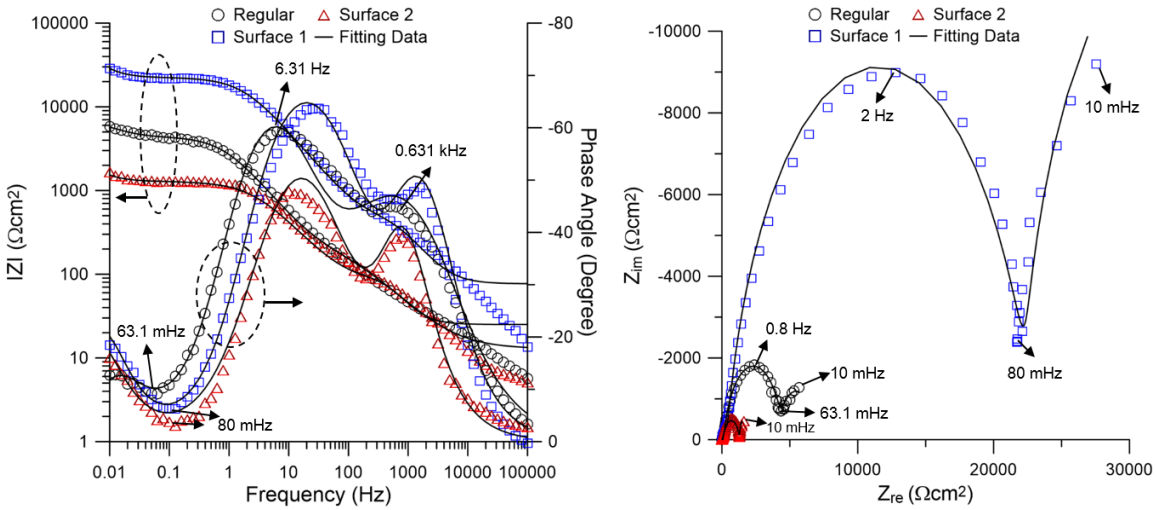

(b)

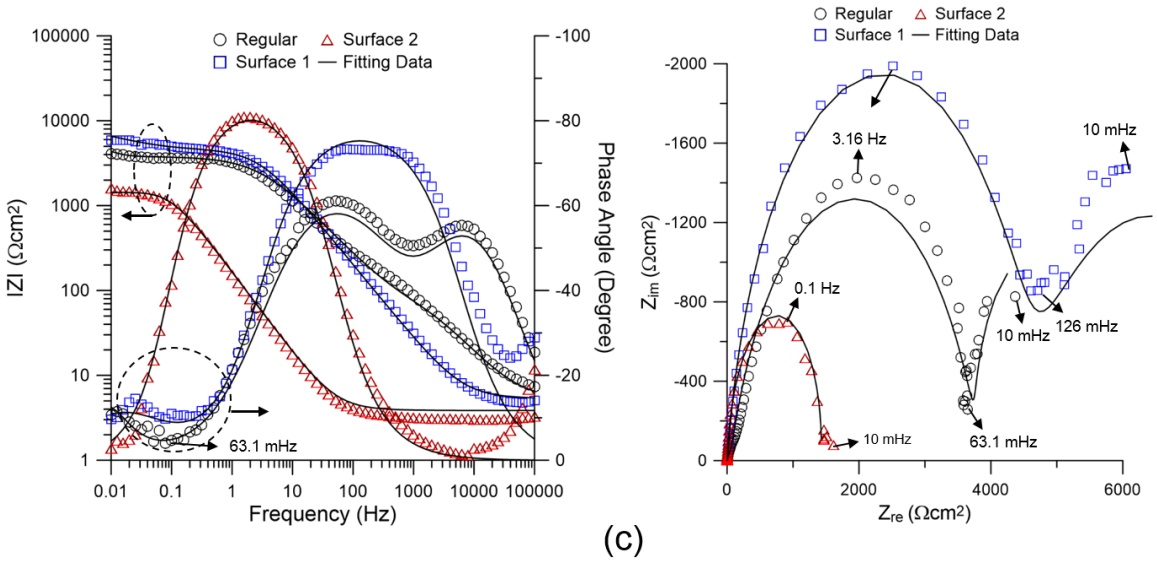
Regular
Surface 2
Surface 1
Fitting Data
|Z| (Ωcm²)
Phase Angle (Degree)
Frequency (Hz)
63.1 mHz
Zim (Ωcm²)
Zre (Ωcm²)
3.16 Hz
10 mHz
0.1 Hz
126 mHz
63.1 mHz

(c)

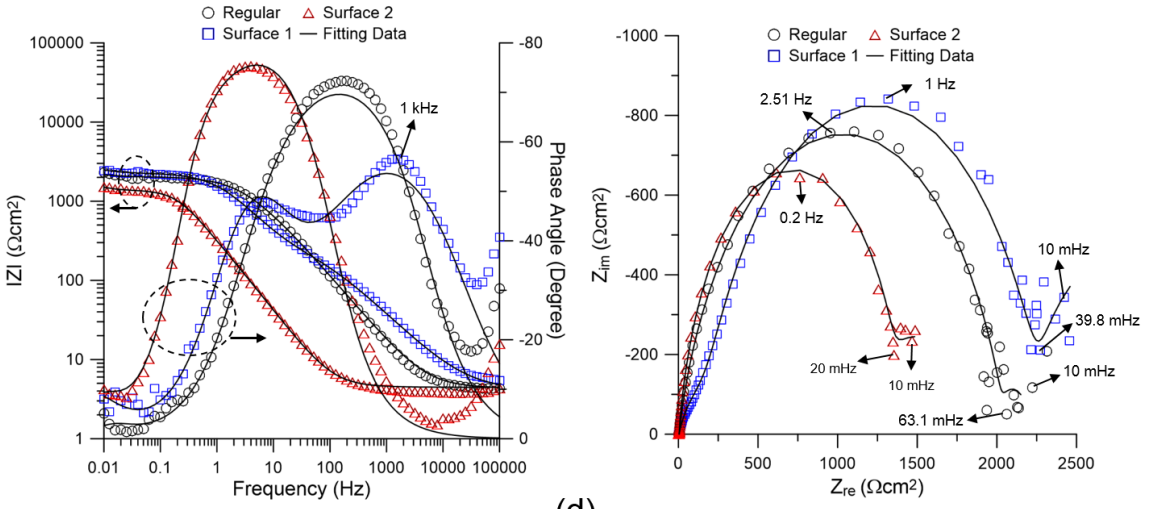
Regular
Surface 2
Surface 1
Fitting Data
|Z| (Ωcm²)
Phase Angle (Degree)
Frequency (Hz)
1 kHz
Zim (Ωcm²)
Zre (Ωcm²)
2.51 Hz
1 Hz
0.2 Hz
10 mHz
39.8 mHz
20 mHz
63.1 mHz

(d)

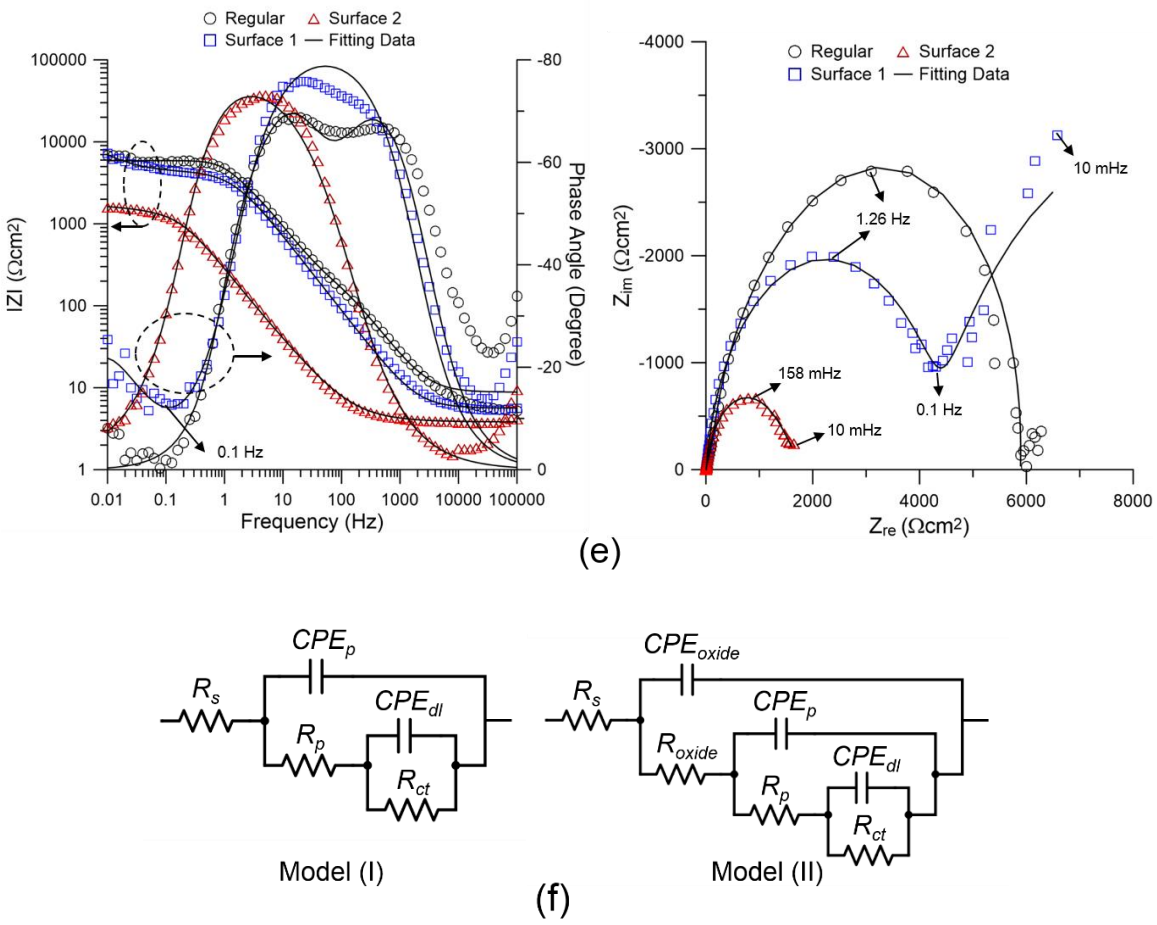

Figure 4-19: EIS spectra and the fitting data, *i.e.* Z modulus, Bode phase angle plot, and Nyquist plot of the upskin layer of the Regular, Surface 1, and Surface 2 samples in aerated 3.5 wt.% NaCl solution after (a) 1 hr, (b) 24 hr, (c) 48 hr, (d) 72 hr, and (e) 96 hr of immersion times, (f) two equivalent electric circuits proposed to describe the EIS data over time.

Table 4-7: The fitting parameters of the EIS measurements comprising the elements of the EECs shown in Figure 4-19f

Time (*hr*)	EEC Model	R_s (Ωcm^2)	R_{oxide} ($k\Omega cm^2$)	CPE_{oxide}, Y_o ($\mu S\ Sec^n\ cm^{-2}$)	n_{oxide}	R_p ($k\Omega cm^2$)	CPE_p, Y_o ($\mu S\ Sec^n\ cm^{-2}$)	n_p	R_{ct} ($k\Omega cm^2$)	CPE_{dl}, Y_o ($\mu S\ Sec^n\ cm^{-2}$)	n_{dl}
Regular											
1	II	5.93	0.29	2.00	0.92	12.80	23.30	0.99	13.80	6.98	0.91
24	II	4.95	0.15	51.60	0.93	2.31	60.20	0.97	4.23	53.40	0.91
48	II	5.16	0.10	6.00	0.93	1.70	20.80	0.92	3.72	18.70	0.99
72	I	4.46	---	---	---	0.10	22.40	0.92	1.27	5.86	0.98
96	II	8.80	2.31	35.00	0.91	1.20	23.70	0.94	3.48	36.10	0.99
Surface 1											
1	II	15.70	5.42	5.55	0.91	17.80	1.11	0.99	36.50	5.79	0.90
24	II	17.60	0.30	0.91	0.99	22.20	5.27	0.95	24.90	13.90	0.97
48	II	9.13	0.44	1.30	0.92	19.70	15.10	0.99	21.20	4.53	0.91
72	II	4.36	1.52	39.30	0.94	0.15	9.94	0.99	0.54	12.10	0.92
96	II	5.64	4.44	30.50	0.92	1.13	9.73	0.99	6.45	23.00	0.94
Surface 2											
1	II	18.60	0.27	4.02	0.97	10.70	7.53	0.94	12.40	23.60	0.97
24	II	17.21	0.10	3.91	0.99	1.22	75.40	0.93	1.39	29.80	0.98
48	I	3.85	---	---	---	0.25	40.10	0.99	0.30	25.30	0.96
72	II	4.03	2.08	92.30	0.95	0.19	68.70	0.91	0.90	30.50	0.95
96	I	3.82	---	---	---	0.10	60.70	0.99	0.67	28.60	0.92

4.5 Discussion

In this study, three groups of DMLS-AlSi10Mg samples with improved surface roughness by utilizing carefully selected DMLS processing parameters were fabricated. Albeit the surface roughness measurement data indicated improvement in the surface quality of the samples in the order of Regular < Surface 1 < Surface 2 sample, the performed electrochemical tests in aerated 3.5 wt.% NaCl solution at 25 °C confirmed a different trend for the corrosion performance and electrochemical stability of the samples in an order of

Surface 2 < Regular < Surface 1 sample. Therefore, a discrepancy was found between the samples' surface roughness trend and their electrochemical stability as Surface 2 sample with the smoothest surface demonstrated the lowest corrosion performance. To elaborate on the corrosion behavior of the Regular and more smoothed samples herein, microstructural features of the samples in their upskin layer, including the size and distribution of Si precipitates embedded in the aluminum matrix, aluminum matrix cell size distribution, grain size and orientation of the aluminum matrix, and the morphological features of the corroded surfaces should be considered. It is well established that the melt pool boundaries of the DMLS-AlSi10Mg alloy, where larger Al dendrites enclosed by coarser Si precipitates are present, compared to the center of each melt pool, are the preferred sites for selective corrosion attack in Chloride containing environments [19,21,32]. The origin of this selective corrosion attack in the coarse regions at the periphery of each melt pool has been associated to the higher potential difference between the Si and the aluminum matrix within the coarse melt pool regions than in other areas of each melt pool, leading to a higher driving force for galvanic corrosion along the melt pool borders [21,32]. As more Si atoms leave the cubic Al crystals and either form new precipitates inside Al dendrites, or join and coarsen the pre-existing Si network at the border of Al dendrites, this Volta potential difference between the Si precipitates and the Al matrix signifies [21,110]. Consequently, the susceptibility of the surface to galvanic corrosion attack increases. Therefore, not only further expansion of the coarse MP regions towards the melt pool center, but also formation of coarser Al dendrites comprising a lower

content of Si solute atoms (in solid solution form), enclosed by coarser eutectic Si particles, can deteriorate the resistance of the surface against selective corrosion attack.

Microstructural analysis of Surface 1 and Surface 2 samples revealed periodic formation of large and small melt pools in their upskin layers, which is one of the most prominent findings in this study and hitherto unreported for AM products, arising from employing a very small hatch distance in the fabrication process, and was rationalized by considering the solidification behavior of the samples. To further elaborate on this, it should be noted that the thermal conductivity at the boundaries between a melt pool in liquid or solid state and the neighboring unmelted metal powder is reported to be low [98,111], similar mechanism to low thermal conductivity of metal foams with high porosity [112], as opposed to the previously solidified deposited layer with drastically high thermal conductivity (120-170 $Wm^{-1}K^{-1}$ [113]). Therefore, the major heat dissipation during solidification of a melt pool is through the previously solidified layer. When the overlap between a fused melt pool and its adjunct solidified track is high (the case of Surface 1 sample, shown in Figure 4-5c), the MP under solidification can experience extremely high cooling rates (as high as 10^5 K/s [114,115]). This leads to the formation of a microstructure with finer grain structure (Figure 4-13) and lower content of eutectic Si precipitates (see Figure 4-11) and an α-Al matrix with higher content of solute Si in solid solution form (Figure 4-11). In other words, the heat removal capacity from the large melt pools of Surface 1 sample was higher than that of Surface 2 and Regular samples, leading to a higher cooling rate and faster solidification of its upskin layer. The slower cooling rate of the large

MPs of Surface 2 sample leads to the formation of a more expanded HAZ and coarse MP regions adjacent to the large melt pools, characterized by having an aluminum cellular dendritic structure surrounded by coarser eutectic Si precipitates. This consequently leads to a greater potential difference between Si precipitates and aluminum matrix in MP-coarse regions, indicating a higher susceptibility of Surface 2 sample to selective corrosion attack, in spite of its lowest surface roughness.

On the other hand, the faster solidification rate of the melt pools in Surface 1 sample hinders the precipitation and growth of Si phase even in its coarse melt pool regions, contributing to the formation of more confined coarse MP regions, containing Si and Al phases with lower potential differences. This suppresses the susceptibility of Surface 1 sample to selective corrosion attack.

Both microstructure and corrosion performance differences between the Regular and Surface 1 samples were not as significant as the ones between Surface 1 and Surface 2 samples, even though the overlap between the two successive passes was smaller in the Regular sample than Surface 2 sample. This can be ascribed to the lower volumetric energy density that was used to fabricate the Regular sample, leading to the formation of smaller melt pools that could undergo a faster solidification rate than the large MPs in Surface 2. Hence, in the Regular sample, melt pools experience an intermediate cooling rate as the melt pools sizes are noticeably smaller than those in the other two samples, but the greater hatch distance in this sample contributed to an intermediate cooling rate during

solidification, and resulted in a corrosion performance between Surface 2 and Surface 1 samples.

Therefore, the microstructural characteristics of the samples fabricated using different processing parameters were found to be the dominant factor in controlling and dictating the corrosion properties of the DMLS-AlSi10Mg samples in the as-printed condition, than their surface roughness. This prominent remark should be taken into the consideration to avoid unforeseen failures of the additively manufactured parts, particularly for harsh environment applications, such as in marine [32,33,89], where abrupt surface degradations of the material in the environment can unexpectedly deteriorate the functionality and integrity of the components.

4.6 Conclusions

In this study, the microstructure and electrochemical properties of three groups of AlSi10Mg alloy parts with improved surface quality; namely Regular, Surface 1, and Surface 2 samples, produced by direct metal laser sintering (DMLS) were investigated. The following conclusions can be drawn from this study:

1. Using appropriate combinations of DMLS process parameters enabled surface roughness improvement of the samples from Regular (R_a = 5.1 ± 1.5 μm) to Surface 1 (R_a = 1.4 ± 0.5 μm), and Surface 2 (R_a = 1.1 ± 0.2 μm) samples, arising from the increased volumetric energy density and the reduced hatch distance employed in fabrication of Surface 1 and Surface 2 samples.

2. The reduced hatch distance resulted in a periodic formation of large and small melt pools in Surface 1 and Surface 2 samples. Formation of such bimodal structure was ascribed to the increased heat dissipation through the previously solidified track, leading to the formation of small melt pools, followed by an increased spacing for the powder particles to interact with the laser beam in the next track, leading to the formation of large melt pools in a cyclic manner.
3. Microstructural analysis of the samples revealed noticeably larger microstructure in the coarse melt pool regions of the large MPs of Surface 2 sample, which was more extended towards the melt pool center, comprised a coarser Si network embedded in larger aluminum cellular dendritic structure. The large melt pools in Surface 1 and Regular sample were shown to exhibit a more confined MP-coarse and HAZ regions with finer cellular structure.
4. The coarser microstructure of large melt pools in Surface 2 relative to Regular and Surface 1 samples was correlated to the lower cooling rate associated with the solidification of Surface 2 large melt pools, owing to the smaller overlap between the large and small melt pools in Surface 2 sample.
5. Slower solidification rate of large MPs in Surface 2 sample was also confirmed by coarser aluminum grain structure possessing a stronger {100}<100> cubic texture.
6. The large melt pools of Surface 1 sample exhibited a finer and more uniformly distributed grains having a weaker texture in its large melt pools, ascribed to the faster

cooling and higher solidification rate of the melt pools in this sample, resulted from the increased overlapping between its melt pools.

7. To characterize and measure the electrochemical properties of all samples, anodic potentiodynamic polarization, cyclic potentiodynamic polarization, and electrochemical impedance spectroscopy were conducted in aerated 3.5 wt.% NaCl electrolyte at 25 °C. Polarization results revealed the highest corrosion potential accompanied by the lowest corrosion current density and the highest pitting potential for Surface 1 sample, confirming the highest resistance to general and pitting attack for Surface 1 than the other two samples.
8. Surface 2 sample exhibited the lowest corrosion performance indicated by the lowest corrosion and pitting potentials along with the highest corrosion current density for this sample.
9. EIS results also confirmed the existence of a more stable passive layer on Surface 1, providing a better resistance against corrosion, followed by the Regular and Surface 2 samples.
10. The corrosion morphology study of the surfaces after polarization testing also confirmed increased severity of pitting and selective corrosion attacks along the melt pool boundaries of the samples in the order of Surface 1 < Regular < Surface 2 samples.
11. The poor corrosion performance of Surface 2 sample was attributed to the coarser microstructure of both Al dendrite and Si precipitates along the borders of its large

MPs, consequently contributing to formation of a higher potential difference between the Si network and Al matrix in that region, representing a greater driving force for galvanic corrosion.

12. The faster cooling and solidification rate of large MPs in Surface 1 sample limited the coarsening of aluminum dendrites and Si precipitates in the large MP regions and contributed to a reduced potential difference between Al and Si phases in that region, leading to the reduced susceptibility of the alloy to both pitting and selective corrosion attacks.

Chapter 5

SUMMARY AND FUTURE WORK

5.1 Summary

In this research, with the primary goal of understanding the corrosion performance and electrochemical behaviour of direct metal laser sintered (DMLS) AlSi10Mg alloy versus its cast counterpart, A360.1 alloy, initially, general microstructure and corrosion properties of the DMLS-AlSi10Mg were evaluated and compared with those of the cast A360.1 alloy, using various characterization, polarization, and electrochemical impedance spectroscopy testing techiques. The microstructure of the DMLS-AlSi10Mg alloy was characterized by by a cellular dendritic structure composed of dendrites of the α-Al solid solution and the interdendritic Si particles, entirely different from the heavily precipitated microstructure of the cast alloy. An improved corrosion resistance was detected for the DMLS fabricated alloy correlated to the fine microstructure, uniform distribution of fine Si particles without formation of any intermetallic resulted from extremely rapid cooling and solidification rate during DMLS process. However, the melt pool boundaries in the DMLS fabricated alloy were found to be susceptible to a selective corrosion attack on the α-Al matrix, where Si particles separate as idiomorphic crystals.

Following the initial step of this research, the impact of post-printing surface finishing procedures, including grinding and sandblasting, on the corrosion performance of the alloy was also investigated. The results highlighted an improved corrosion resistance of the DMLS-AlSi10Mg alloy after surface grinding, attributed to the formation of a stable,

dense, and thick passive film on its surface. Differently, the as-printed and sandblasted surfaces were found to be more susceptible to corrosion attack due to the existing surface porosities and the superficial roughness on the surface of these samples.

Since the superficial roughness on the surface of as-printed DMLS-AlSi10Mg alloy was found to be detrimental to the corrosion performance of the alloy, significantly lowered surface roughness values were achieved by tuning the DMLS process parameters instead of applying a post-printing operation. Interestingly, the reduced hatched distance used in fabrication of DMLS-AlSi10Mg samples led to formation of a periodic large and small melt pools in the structure. The larger melt pools revealed a coarser microstructure comprised of a coarser Si network embedded in larger aluminium cellular dendritic structure possessing a stronger {100}<100> cubic texture. The samples containing larger melt pools revealed a poor corrosion resistance in spite of their improved surface roughness. This behaviour was was attributed to the coarser microstructure of both Al dendrite and Si precipitates along the borders of its large MPs, consequently contributing to formation of a higher potential difference between the Si network and Al matrix in that region, representing a greater driving force for galvanic corrosion.

5.2 Recommendations for Future Research

The following topics are suggested for future research:

1. In current thesis, to evaluate the impact of the surface roughness on the electrochemical stability of the low surface roughness DMLS-AlSi10Mg samples, all corrosion testing

had to be done on the as-printed surfaces. However, to study only the impact of microstructure on the corrosion resistance of the samples, the contributions from the surface roughness or any other impacting surface related factor, such as surface porosities, has to be eliminated, and all tests should be done on polished surfaces. This is a subject for a future study.

2. All the samples in current study were fabricated using virgin feedstock metal powder. This potentially increases the cost of fabrication process. One way to increase the affordability of the DMLS process is to minimize wasting of the feedstock metal powder and collecting the remaining powder after each building cycle and reuse it. However, the impacts of utilizing re-used powder on the formation of solidification defects and corrosion properties of the fabricated parts are still unknown. This is also another subject for a future study.

3. Finally, for many industrial applications, using dissimilar aluminum alloys with different chemical compositions is common. Such dissimilar metal combinations can potentially be fabricated using DMLS process. However, due to the susceptibility of dissimilar metals to galvanic corrosion attack, evaluating the electrochemical behavior of such dissimilar metals are critical and demands for extensive analysis in the future.

REFERENCES

[1] W.J. Sames, F.A. List, S. Pannala, R.R. Dehoff, S.S. Babu, The metallurgy and processing science of metal additive manufacturing, Int. Mater. Rev. 61 (2016) 315–360. doi:10.1080/09506608.2015.1116649.

[2] E. Atzeni, A. Salmi, Economics of additive manufacturing for end-usable metal parts, Int. J. Adv. Manuf. Technol. 62 (2012) 1147–1155. doi:10.1007/s00170-011-3878-1.

[3] D. Herzog, V. Seyda, E. Wycisk, C. Emmelmann, Additive manufacturing of metals, Acta Mater. 117 (2016) 371–392. doi:10.1016/j.actamat.2016.07.019.

[4] Trumpf GmbH & Co. KG, (n.d.). www.trumpf.com (accessed June 5, 2017).

[5] D.D. Gu, W. Meiners, K. Wissenbach, R. Poprawe, Laser additive manufacturing of metallic components: materials, processes and mechanisms, Int. Mater. Rev. 57 (2012) 133–164. doi:10.1179/1743280411Y.0000000014.

[6] N. Kang, P. Coddet, H. Liao, T. Baur, C. Coddet, Wear behavior and microstructure of hypereutectic Al-Si alloys prepared by selective laser melting, Appl. Surf. Sci. 378 (2016) 142–149. doi:https://doi.org/10.1016/j.apsusc.2016.03.221.

[7] B. Li, H. Wang, J. Jie, Z. Wei, Effects of yttrium and heat treatment on the microstructure and tensile properties of Al–7.5Si–0.5Mg alloy, Mater. Des. 32 (2011) 1617–1622. doi:https://doi.org/10.1016/j.matdes.2010.08.040.

[8] P. Wei, Z. Wei, Z. Chen, J. Du, Y. He, J. Li, Y. Zhou, The AlSi10Mg samples produced by selective laser melting: single track, densification, microstructure and mechanical behavior, Appl. Surf. Sci. 408 (2017) 38–50. doi:https://doi.org/10.1016/j.apsusc.2017.02.215.

[9] M. Rafieazad, P. Fathi, M. Mohammadi, X. Duan, A.M. Nasiri, Low temperature heat-treatment cycle on AlSi10Mg_200C alloy fabricated by direct laser metal sintering: microstructure evolution and corrosion resistivity, in: Int. Conf. Alum. Alloy., Montreal, 2018.

[10] A.K. Gupta, D.J. Lloyd, S.A. Court, Precipitation hardening in Al–Mg–Si alloys with and without excess Si, Mater. Sci. Eng. A. 316 (2001) 11–17. doi:https://doi.org/10.1016/S0921-5093(01)01247-3.

[11] A. Hadadzadeh, B.S. Amirkhiz, J. Li, A. Odeshi, M. Mohammadi, Deformation mechanism during dynamic loading of an additively manufactured AlSi10Mg_200C, Mater. Sci. Eng. A. 722 (2018) 263–268. doi:https://doi.org/10.1016/j.msea.2018.03.014.

[12] A. Hadadzadeh, C. Baxter, B.S. Amirkhiz, M. Mohammadi, Strengthening mechanisms in direct metal laser sintered AlSi10Mg: Comparison between virgin

and recycled powders, Addit. Manuf. 23 (2018) 108–120. doi:10.1016/j.addma.2018.07.014.

[13] A. Hadadzadeh, B.S. Amirkhiz, J. Li, M. Mohammadi, Columnar to equiaxed transition during direct metal laser sintering of AlSi10Mg alloy: Effect of building direction, Addit. Manuf. 23 (2018) 121–131. doi:10.1016/j.addma.2018.08.001.

[14] S. Marola, D. Manfredi, G. Fiore, M.G. Poletti, M. Lombardi, P. Fino, L. Battezzati, A comparison of Selective Laser Melting with bulk rapid solidification of AlSi10Mg alloy, J. Alloys Compd. 742 (2018) 271–279. doi:10.1016/j.jallcom.2018.01.309.

[15] J. Liu, A.C. To, Quantitative texture prediction of epitaxial columnar grains in additive manufacturing using selective laser melting, Addit. Manuf. 16 (2017) 58–64. doi:10.1016/j.addma.2017.05.005.

[16] Y.J. Liu, Z. Liu, Y. Jiang, G.W. Wang, Y. Yang, L.C. Zhang, Gradient in microstructure and mechanical property of selective laser melted AlSi10Mg, J. Alloys Compd. 735 (2017) 1414–1421. doi:10.1016/j.jallcom.2017.11.020.

[17] A. Hadadzadeh, B.S. Amirkhiz, A. Odeshi, M. Mohammadi, Dynamic loading of direct metal laser sintered AlSi10Mg alloy: Strengthening behavior in different building directions, Mater. Des. 159 (2018) 201–211. doi:https://doi.org/10.1016/j.matdes.2018.08.045.

[18] C. Baxter, E. Cyr, A. Odeshi, M. Mohammadi, Constitutive models for the dynamic behaviour of direct metal laser sintered AlSi10Mg_200C under high strain rate shock loading, Mater. Sci. Eng. A. 731 (2018) 296–308. doi:https://doi.org/10.1016/j.msea.2018.06.040.

[19] M. Cabrini, S. Lorenzi, T. Pastore, S. Pellegrini, E.P. Ambrosio, F. Calignano, D. Manfredi, M. Pavese, P. Fino, Effect of heat treatment on corrosion resistance of DMLS AlSi10Mg alloy, Electrochim. Acta. 206 (2016) 346–355. doi:10.1016/j.electacta.2016.04.157.

[20] M. Cabrini, F. Calignano, P. Fino, S. Lorenzi, M. Lorusso, D. Manfredi, C. Testa, T. Pastore, Corrosion behavior of heat-treated AlSi10Mg manufactured by laser powder bed fusion, Materials (Basel). 11 (2018). doi:10.3390/ma11071051.

[21] R.I. Revilla, J. Liang, S. Godet, I. De Graeve, Local Corrosion Behavior of Additive Manufactured AlSiMg Alloy Assessed by SEM and SKPFM, J. Electrochem. Soc. 164 (2017) C27–C35. doi:10.1149/2.0461702jes.

[22] M. Cabrini, S. Lorenzi, T. Pastore, S. Pellegrini, D. Manfredi, P. Fino, S. Biamino, C. Badini, Evaluation of corrosion resistance of Al – 10Si – Mg alloy obtained by means of Direct Metal Laser Sintering, J. Mater. Process. Tech. 231 (2016) 326–335. doi:10.1016/j.jmatprotec.2015.12.033.

[23] Y. Chen, J. Zhang, X. Gu, N. Dai, P. Qin, L.-C. Zhang, Distinction of corrosion resistance of selective laser melted Al-12Si alloy on different planes, J. Alloys

Compd. 747 (2018) 648–658. doi:https://doi.org/10.1016/j.jallcom.2018.03.062.

[24] M. Cabrini, S. Lorenzi, T. Pastore, S. Pellegrini, M. Pavese, P. Fino, E.P. Ambrosio, F. Calignano, D. Manfredi, Corrosion resistance of direct metal laser sintering AlSiMg alloy, Surf. Interface Anal. 48 (2016) 818–826. doi:10.1002/sia.5981.

[25] A. Leon, E. Aghion, Effect of surface roughness on corrosion fatigue performance of AlSi10Mg alloy produced by Selective Laser Melting (SLM), Mater. Charact. 131 (2017) 188–194. doi:10.1016/j.matchar.2017.06.029.

[26] M. Mohammadi, H. Asgari, Achieving low surface roughness AlSi10Mg 200C parts using direct metal laser sintering, Addit. Manuf. 20 (2018) 23–32. doi:10.1016/j.addma.2017.12.012.

[27] F. Calignano, D. Manfredi, E.P. Ambrosio, L. Iuliano, P. Fino, Influence of process parameters on surface roughness of aluminum parts produced by DMLS, Int. J. Adv. Manuf. Technol. 67 (2013) 2743–2751. doi:10.1007/s00170-012-4688-9.

[28] A. Leon, E. Aghion, Effect of surface roughness on corrosion fatigue performance of AlSi10Mg alloy produced by Selective Laser Melting (SLM), Mater. Charact. 131 (2017) 188–194. doi:https://doi.org/10.1016/j.matchar.2017.06.029.

[29] W.J. Wang, K.C. Yung, H.S. Choy, T.Y. Xiao, Z.X. Cai, Effects of laser polishing on surface microstructure and corrosion resistance of additive manufactured CoCr alloys, Appl. Surf. Sci. 443 (2018) 167–175. doi:https://doi.org/10.1016/j.apsusc.2018.02.246.

[30] G. Pyka, G. Kerckhofs, I. Papantoniou, M. Speirs, J. Schrooten, M. Wevers, Surface Roughness and Morphology Customization of Additive Manufactured Open Porous Ti6Al4V Structures, (2013) 4737–4757. doi:10.3390/ma6104737.

[31] P. Wen, M. Voshage, L. Jauer, Y. Chen, Y. Qin, R. Poprawe, J.H. Schleifenbaum, Laser additive manufacturing of Zn metal parts for biodegradable applications: Processing, formation quality and mechanical properties, Mater. Des. 155 (2018) 36–45. doi:https://doi.org/10.1016/j.matdes.2018.05.057.

[32] P. Fathi, M. Mohammadi, X. Duan, A.M. Nasiri, A comparative study on corrosion and microstructure of direct metal laser sintered AlSi10Mg_200C and die cast A360.1 aluminum, J. Mater. Process. Technol. 259 (2018) 1–14. doi:https://doi.org/10.1016/j.jmatprotec.2018.04.013.

[33] H. Asgari, M. Mohammadi, Microstructure and mechanical properties of stainless steel CX manufactured by Direct Metal Laser Sintering, Mater. Sci. Eng. A. 709 (2018) 82–89. doi:10.1016/j.msea.2017.10.045.

[34] N. Hrabe, T. Gnäupel-Herold, T. Quinn, Fatigue properties of a titanium alloy (Ti–6Al–4V) fabricated via electron beam melting (EBM): Effects of internal defects and residual stress, Int. J. Fatigue. 94, Part 2 (2017) 202–210. doi:https://doi.org/10.1016/j.ijfatigue.2016.04.022.

[35] E. Cyr, H. Asgari, S. Shamsdini, M. Purdy, K. Hosseinkhani, M. Mohammadi, Fracture behaviour of additively manufactured MS1-H13 hybrid hard steels, Mater. Lett. 212 (2018) 174–177. doi:10.1016/j.matlet.2017.10.097.

[36] I. Rosenthal, A. Stern, N. Frage, Microstructure and Mechanical Properties of AlSi10Mg Parts Produced by the Laser Beam Additive Manufacturing (AM) Technology, Metallogr. Microstruct. Anal. 3 (2014) 448–453. doi:10.1007/s13632-014-0168-y.

[37] A.P. Ventura, Microstructural Evolution and Mechanical Property Development of Selective Laser Melted Copper Alloys, Lehigh University, 2017.

[38] Z. Mao, D.Z. Zhang, P. Wei, K. Zhang, Manufacturing feasibility and forming properties of Cu-4Sn in selective laser melting, Materials (Basel). 10 (2017). doi:10.3390/ma10040333.

[39] H. Asgari, C. Baxter, K. Hosseinkhani, M. Mohammadi, On microstructure and mechanical properties of additively manufactured AlSi10Mg_200C using recycled powder, Mater. Sci. Eng. A. 707 (2017) 148–158. doi:10.1016/j.msea.2017.09.041.

[40] M. Tang, P.C. Pistorius, Oxides, porosity and fatigue performance of AlSi10Mg parts produced by selective laser melting, Int. J. Fatigue. 94, Part 2 (2017) 192–201. doi:https://doi.org/10.1016/j.ijfatigue.2016.06.002.

[41] H. Asgari, A. Odeshi, K. Hosseinkhani, M. Mohammadi, On dynamic mechanical behavior of additively manufactured AlSi10Mg_200C, Mater. Lett. 211 (2018) 187–190. doi:https://doi.org/10.1016/j.matlet.2017.10.001.

[42] N.T. Aboulkhair, I. Maskery, C. Tuck, I. Ashcroft, N.M. Everitt, The microstructure and mechanical properties of selectively laser melted AlSi10Mg: The effect of a conventional T6-like heat treatment, Mater. Sci. Eng. A. 667 (2016) 139–146. doi:10.1016/j.msea.2016.04.092.

[43] S.G. Shabestari, H. Moemeni, Effect of copper and solidification conditions on the microstructure and mechanical properties of Al–Si–Mg alloys, J. Mater. Process. Technol. 153 (2004) 193–198. doi:https://doi.org/10.1016/j.jmatprotec.2004.04.302.

[44] D. Manfredi, F. Calignano, M. Krishnan, R. Canali, E.P. Ambrosio, E. Atzeni, From powders to dense metal parts: Characterization of a commercial AlSiMg alloy processed through direct metal laser sintering, Materials (Basel). 6 (2013) 856–869. doi:10.3390/ma6030856.

[45] D. Manfredi, F. Calignano, E.P. Ambrosio, M. Krishnan, R. Canali, S. Biamino, M. Pavese, E. Atzeni, L. Luliano, P. Fino, C. Badini, Direct Metal Laser Sintering: An additive manufacturing technology ready to produce lightweight structural parts for robotic applications, Metall. Ital. 105 (2013) 15–24. doi:10.1016/j.jallcom.2016.10.285.

[46] N.T. Aboulkhair, I. Maskery, C. Tuck, I. Ashcroft, N.M. Everitt, On the formation of AlSi10Mg single tracks and layers in selective laser melting: Microstructure and nano-mechanical properties, J. Mater. Process. Technol. 230 (2016) 88–98. doi:https://doi.org/10.1016/j.jmatprotec.2015.11.016.

[47] Z. Szklarska-Smialowska, Pitting corrosion of aluminum, Corros. Sci. 41 (1999) 1743–1767. doi:https://doi.org/10.1016/S0010-938X(99)00012-8.

[48] R.P. Wei, C.-M. Liao, M. Gao, A transmission electron microscopy study of constituent-particle-induced corrosion in 7075-T6 and 2024-T3 aluminum alloys, Metall. Mater. Trans. A. 29 (1998) 1153–1160. doi:10.1007/s11661-998-0241-8.

[49] V. Guillaumin, G. Mankowski, Localized corrosion of 6056 T6 aluminium alloy in chloride media, Corros. Sci. 42 (2000) 105–125. doi:https://doi.org/10.1016/S0010-938X(99)00053-0.

[50] L.E. Fratila-Apachitei, I. Apachitei, J. Duszczyk, Characterization of cast AlSi(Cu) alloys by scanning Kelvin probe force microscopy, Electrochim. Acta. 51 (2006) 5892–5896. doi:https://doi.org/10.1016/j.electacta.2006.03.027.

[51] F. Andreatta, H. Terryn, J.H.W. de Wit, Effect of solution heat treatment on galvanic coupling between intermetallics and matrix in AA7075-T6, Corros. Sci. 45 (2003) 1733–1746. doi:https://doi.org/10.1016/S0010-938X(03)00004-0.

[52] Y. Liao, Practical Electron Microscopy and Database, Al-X phase diagrams, (2007). http://www.globalsino.com/EM/.

[53] ASTM-G5-82, Standard reference method for making potentiostatic and potentiodynamic anodic polarisation measurements, Annul B. ASTM Standards vol. 03.02, Reapproved as ASTM-65-87 and as ASTM-65-94, 1982.

[54] K.S. Ferrer, R.G. Kelly, Comparison of Methods for Removal of Corrosion Product from AA2024-T3, Corrosion. 57 (2001) 110–117.

[55] R. Chou, J. Milligan, M. Paliwal, M. Brochu, Additive Manufacturing of Al-12Si Alloy Via Pulsed Selective Laser Melting, JOM. 67 (2015) 590–596. doi:10.1007/s11837-014-1272-9.

[56] R. Chou, A. Ghosh, S.C. Chou, M. Paliwal, M. Brochu, Microstructure and mechanical properties of Al10SiMg fabricated by pulsed laser powder bed fusion, Mater. Sci. Eng. A. 689 (2017) 53–62. doi:10.1016/j.msea.2017.02.023.

[57] N.T. Aboulkhair, N.M. Everitt, I. Ashcroft, C. Tuck, Reducing porosity in AlSi10Mg parts processed by selective laser melting, Addit. Manuf. 1 (2014) 77–86. doi:10.1016/j.addma.2014.08.001.

[58] I. Rosenthal, A. Stern, N. Frage, Materials Science & Engineering A Strain rate sensitivity and fracture mechanism of AlSi10Mg parts produced by Selective Laser Melting, Mater. Sci. Eng. A. 682 (2017) 509–517. doi:10.1016/j.msea.2016.11.070.

[59] S. Kou, Welding Metallurgy, 2nd ed., Wiley Interscience, New Jersey, 2003.

[60] Y. Birol, Microstructural evolution during annealing of a rapidly solidified Al–12Si alloy, J. Alloys Compd. 439 (2007) 81–86. doi:https://doi.org/10.1016/j.jallcom.2006.08.068.

[61] O. Uzun, T. Karaaslan, M. Gogebakan, M. Keskin, Hardness and microstructural characteristics of rapidly solidified Al–8–16 wt.%Si alloys, J. Alloys Compd. 376 (2004) 149–157. doi:https://doi.org/10.1016/j.jallcom.2004.01.017.

[62] S. Van Bael, G. Kerckhofs, M. Moesen, G. Pyka, J. Schrooten, J.P. Kruth, Micro-CT-based improvement of geometrical and mechanical controllability of selective laser melted Ti6Al4V porous structures, Mater. Sci. Eng. A. 528 (2011) 7423–7431. doi:https://doi.org/10.1016/j.msea.2011.06.045.

[63] A. Dobkowska, B. Adamczyk – Cieślak, J. Mizera, K.J. Kurzydłowski, A. Kiełbus, The Comparison of the Microstructure and Corrosion Resistance of Sand Cast Aluminum Alloys, Arch. Metall. Mater. 61 (2016) 209–212. doi:10.1515/amm-2016-0038.

[64] S.G. Shabestari, The effect of iron and manganese on the formation of intermetallic compounds in aluminum–silicon alloys, Mater. Sci. Eng. A. 383 (2004) 289–298. doi:https://doi.org/10.1016/j.msea.2004.06.022.

[65] W. Zhou, N.N. Aung, A. Choudhary, M. Kanouni, Heat-transfer corrosion behaviour of cast Al alloy, Corros. Sci. 50 (2008) 3308–3313. doi:10.1016/j.corsci.2008.08.047.

[66] D.J. Chakrabarti, D.E. Laughlin, Phase relations and precipitation in Al–Mg–Si alloys with Cu additions, Prog. Mater. Sci. 49 (2004) 389–410. doi:https://doi.org/10.1016/S0079-6425(03)00031-8.

[67] M.A. Pech-Canul, R. Giridharagopal, M.I. Pech-Canul, E.E. Coral-Escobar, Localized Corrosion Behavior of Al-Si-Mg Alloys Used for Fabrication of Aluminum Matrix Composites, J. Mater. Eng. Perform. 22 (2013) 3922–3932. doi:10.1007/s11665-013-0674-0.

[68] J.R. Davis, ASM Specialty Handbook: Aluminum and Aluminum Alloys, ASM International, Metals Park, Ohio, USA, 1993.

[69] K.A. Yasakau, M.L. Zheludkevich, S. V Lamaka, M.G.S. Ferreira, Role of intermetallic phases in localized corrosion of AA5083, Electrochim. Acta. 52 (2007) 7651–7659. doi:https://doi.org/10.1016/j.electacta.2006.12.072.

[70] R. Arrabal, B. Mingo, A. Pardo, M. Mohedano, E. Matykina, M.C. Merino, A. Rivas, Microstructure and corrosion behaviour of A356 aluminium alloy modified with Nd, Mater. Corros. 66 (2015) 535–541. doi:10.1002/maco.201407674.

[71] R. Arrabal, B. Mingo, A. Pardo, M. Mohedano, E. Matykina, I. Rodríguez, Pitting

corrosion of rheocast A356 aluminium alloy in 3.5wt.% NaCl solution, Corros. Sci. 73 (2013) 342–355. doi:https://doi.org/10.1016/j.corsci.2013.04.023.

[72] S. Jain, Corrosion and protection of heterogeneous cast Al-Si (356) and Al-Si-Cu-Fe (380) alloys by chromate and cerium inhibitors, Ohio State University, 2006.

[73] A. Pardo, M.C. Merino, R. Arrabal, F. Viejo, M. Carboneras, Improvement of Corrosion Behavior of A3xx.x/SiCp Composites in 3.5 wt % NaCl Solution by Ce Surface Coatings, J. Electrochem. Soc. 153 (2006) B52. doi:10.1149/1.2150151.

[74] E. Onofre-Bustamante, M.A. Domínguez-Crespo, A.M. Torres-Huerta, A. Olvera-Martínez, J. Genescá-Llongueras, F.J. Rodríguez-Gómez, Characterization of cerium-based conversion coatings for corrosion protection of AISI-1010 commercial carbon steel, J. Solid State Electrochem. 13 (2009) 1785–1799. doi:10.1007/s10008-009-0871-9.

[75] W.R. Osório, P.R. Goulart, A. Garcia, Effect of silicon content on microstructure and electrochemical behavior of hypoeutectic Al-Si alloys, Mater. Lett. 62 (2008) 365–369. doi:10.1016/j.matlet.2007.05.051.

[76] J.A. Taylor, The Effect of Iron in Al-Si Casting Alloys, 35th Aust. Foundry Inst. Natl. Conf. (2004) 148–157.

[77] K.K. Pius, A Study on the Effects of Iron on Microstructure and Mechanical Properties of Al-Si Alloys, University of Nairobi, 2012.

[78] R.S. Rana, R. Purohit, S. Das, Reviews on the influences of alloying elements on the microstructure and mechanical properties of aluminum alloys and aluminum alloy composites, Int. J. Sci. Res. Publ. 2 (2012) 1–7. doi:10.1023/A:1004674822751.

[79] E.O. Olakanmi, Selective laser sintering/melting (SLS/SLM) of pure Al, Al–Mg, and Al–Si powders: Effect of processing conditions and powder properties, J. Mater. Process. Technol. 213 (2013) 1387–1405. doi:https://doi.org/10.1016/j.jmatprotec.2013.03.009.

[80] P. Dumas, D. Rivi, Y. Levy, J. Corset, P. Dumas, D. Rivi, Growth of Thin Alumina Film on Aluminium At Room Temperature : a Kinetic and Spectroscopic Study By Surface Plasmon Excitation, J. Phys. Colloq. 44 (1983) C10-205-C10-208.

[81] K. Jafarzadeh, T. Shahrabi, M.G. Hosseini, EIS study on pitting corrosion of AA5083-H321 aluminum-magnesium alloy in stagnant 3.5% NaCl solution, J. Mater. Sci. Technol. 24 (2008) 215–219. https://www.scopus.com/inward/record.uri?eid=2-s2.0-42449122372&partnerID=40&md5=c31f8b7c8883b82db68e703ed1385780.

[82] H.-S. Lee, J.K. Singh, M.A. Ismail, C. Bhattacharya, Corrosion Resistance Properties of Aluminum Coating Applied by Arc Thermal Metal Spray in SAE J2334 Solution with Exposure Periods, Metals (Basel). 6 (2016).

[83] S. Gorsse, C. Hutchinson, M. Gouné, R. Banerjee, Additive manufacturing of metals : a brief review of the characteristic microstructures and properties of steels , Ti-6Al-4V and high-entropy alloys, 18 (2017) 584–610.

[84] W.E. Frazier, Metal Additive Manufacturing: A Review, J. Mater. Eng. Perform. 23 (2014) 1917–1928. doi:10.1007/s11665-014-0958-z.

[85] E.O. Olakanmi, R.F. Cochrane, K.W. Dalgarno, A review on selective laser sintering/melting (SLS/SLM) of aluminium alloy powders: Processing, microstructure, and properties, Prog. Mater. Sci. 74 (2015) 401–477. doi:10.1016/J.PMATSCI.2015.03.002.

[86] A. Barari, H.A. Kishawy, F. Kaji, M.A. Elbestawi, On the surface quality of additive manufactured parts, Int. J. Adv. Manuf. Technol. 89 (2017) 1969–1974. doi:10.1007/s00170-016-9215-y.

[87] J. Delgado, J. Ciurana, L. Serenó, Comparison of forming manufacturing processes and selective laser melting technology based on the mechanical properties of products, Virtual Phys. Prototyp. 6 (2011) 167–178. doi:10.1080/17452759.2011.613597.

[88] Y. Tian, D. Tomus, P. Rometsch, X. Wu, Influences of processing parameters on surface roughness of Hastelloy X produced by selective laser melting, Addit. Manuf. 13 (2017) 103–112. doi:https://doi.org/10.1016/j.addma.2016.10.010.

[89] P. Fathi, M. Mohammadi, X. Duan, A.M. Nasiri, Effects of Surface Finishing Procedure on Corrosion Behavior of DMLS-AlSi10Mg_200C Alloy vs Die Cast A360.1 Aluminum, JOM. (2019) 1–12. https://doi.org/10.1007/s11837-019-03344-8.

[90] A. Leon, E. Aghion, Effect of surface roughness on corrosion fatigue performance of AlSi10Mg alloy produced by Selective Laser Melting (SLM), Mater. Charact. 131 (2016) 188–194. doi:10.1016/j.matchar.2017.06.029.

[91] A. Leon, A. Shirizly, E. Aghion, Corrosion Behavior of AlSi10Mg Alloy Produced by Additive Manufacturing (AM) vs. Its Counterpart Gravity Cast Alloy, Metals (Basel). 6 (2016) 148. doi:10.3390/met6070148.

[92] T. Kurzynowski, K. Gruber, W. Stopyra, B. Kuźnicka, E. Chlebus, Correlation between process parameters, microstructure and properties of 316 L stainless steel processed by selective laser melting, Mater. Sci. Eng. A. 718 (2018) 64–73. doi:https://doi.org/10.1016/j.msea.2018.01.103.

[93] Z. Xiang, M. Yin, G. Dong, X. Mei, G. Yin, Modeling of the thermal physical process and study on the reliability of linear energy density for selective laser melting, Results Phys. 9 (2018) 939–946. doi:https://doi.org/10.1016/j.rinp.2018.03.047.

[94] J. Ciurana, L. Hernandez, J. Delgado, Energy density analysis on single tracks

formed by selective laser melting with CoCrMo powder material, Int. J. Adv. Manuf. Technol. 68 (2013) 1103–1110. doi:10.1007/s00170-013-4902-4.

[95] U.S. Bertoli, A.J. Wolfer, M.J. Matthews, J.-P.R. Delplanque, J.M. Schoenung, On the limitations of Volumetric Energy Density as a design parameter for Selective Laser Melting, Mater. Des. 113 (2017) 331–340. doi:https://doi.org/10.1016/j.matdes.2016.10.037.

[96] M. Krishnan, E. Atzeni, R. Canali, F. Calignano, D. Manfredi, E.P. Ambrosio, L. Iuliano, On the effect of process parameters on properties of AlSi10Mg parts produced by DMLS, Rapid Prototyp. J. 20 (2014) 449–458. doi:10.1108/RPJ-03-2013-0028.

[97] L. Thijs, K. Kempen, J.P. Kruth, J. Van Humbeeck, Fine-structured aluminium products with controllable texture by selective laser melting of pre-alloyed AlSi10Mg powder, Acta Mater. 61 (2013) 1809–1819. doi:10.1016/j.actamat.2012.11.052.

[98] M. Liu, N. Takata, A. Suzuki, M. Kobashi, Microstructural characterization of cellular AlSi10Mg alloy fabricated by selective laser melting, Mater. Des. 157 (2018) 478–491. doi:10.1016/j.matdes.2018.08.005.

[99] C. Yan, L. Hao, A. Hussein, P. Young, J. Huang, W. Zhu, Microstructure and mechanical properties of aluminium alloy cellular lattice structures manufactured by direct metal laser sintering, Mater. Sci. Eng. A. 628 (2015) 238–246. doi:https://doi.org/10.1016/j.msea.2015.01.063.

[100] Q. Chu, R. Bai, H. Jian, Z. Lei, N. Hu, C. Yan, Microstructure, texture and mechanical properties of 6061 aluminum laser beam welded joints, Mater. Charact. 137 (2018) 269–276. doi:https://doi.org/10.1016/j.matchar.2018.01.030.

[101] D. Buchbinder, W. Meiners, K. Wissenbach, R. Poprawe, Selective laser melting of aluminum die-cast alloy—Correlations between process parameters, solidification conditions, and resulting mechanical properties, J. Laser Appl. 27 (2015) S29205. doi:10.2351/1.4906389.

[102] H.L. Wei, J. Mazumder, T. DebRoy, Evolution of solidification texture during additive manufacturing., Sci. Rep. 5 (2015) 16446. doi:10.1038/srep16446.

[103] Y. Bai, X. Gai, S. Li, L.-C. Zhang, Y. Liu, Y. Hao, X. Zhang, R. Yang, Y. Gao, Improved corrosion behaviour of electron beam melted Ti-6Al–4V alloy in phosphate buffered saline, Corros. Sci. 123 (2017) 289–296. doi:https://doi.org/10.1016/j.corsci.2017.05.003.

[104] N. Dai, L.-C. Zhang, J. Zhang, Q. Chen, M. Wu, Corrosion behavior of selective laser melted Ti-6Al-4V alloy in NaCl solution, Corros. Sci. 102 (2016) 484–489. doi:https://doi.org/10.1016/j.corsci.2015.10.041.

[105] B. Wu, Z. Pan, S. Li, D. Cuiuri, D. Ding, H. Li, The anisotropic corrosion behaviour

of wire arc additive manufactured Ti-6Al-4V alloy in 3.5% NaCl solution, Corros. Sci. 137 (2018) 176–183. doi:https://doi.org/10.1016/j.corsci.2018.03.047.

[106] Z. Szklarska-Smialowska, Pitting Corrosion of Metals, NACE, Houston, TX, 1986.

[107] J. Liu, K. Zhao, M. Yu, S. Li, Effect of surface abrasion on pitting corrosion of Al-Li alloy, Corros. Sci. 138 (2018) 75–84. doi:https://doi.org/10.1016/j.corsci.2018.04.010.

[108] H. Zhao, M. Yu, J. Liu, S. Li, B. Xue, M. Liang, Effect of Surface Roughness on Corrosion Resistance of Sol-Gel Coatings on AA2024-T3 Alloy, J. Electrochem. Soc. 162 (2015) C718–C724. doi:10.1149/2.0271514jes.

[109] G. Šekularac, I. Milošev, Corrosion of aluminium alloy AlSi7Mg0.3 in artificial sea water with added sodium sulphide, Corros. Sci. 144 (2018) 54–73. doi:https://doi.org/10.1016/j.corsci.2018.08.038.

[110] N. Sathirachinda, R. Pettersson, S. Wessman, J. Pan, Study of nobility of chromium nitrides in isothermally aged duplex stainless steels by using SKPFM and SEM/EDS, Corros. Sci. 52 (2010) 179–186. doi:https://doi.org/10.1016/j.corsci.2009.08.057.

[111] N. Takata, H. Kodaira, A. Suzuki, M. Kobashi, Size dependence of microstructure of AlSi10Mg alloy fabricated by selective laser melting, Mater. Charact. 143 (2018) 18–26. doi:https://doi.org/10.1016/j.matchar.2017.11.052.

[112] M.F. Ashby, A. Evans, N.A. Fleck, J.W. Hutchinson, H.N.G. Wadley, Metals Foams: A Design Guide, 1st ed., Elsevier Science, Burlington, MA, 2000.

[113] E.G.– E.O. Systems, EOS Aluminum AlSi10Mg (material data sheet), (2014). https://cdn0.scrvt.com/eos/public/8837de942d78d3b3/4e099c3a857fdddca4be9d59fbb1cd74/EOS_Aluminium_AlSi10Mg_en.pdf (accessed June 15, 2018).

[114] X.P. Li, X.J. Wang, M. Saunders, A. Suvorova, L.C. Zhang, Y.J. Liu, M.H. Fang, Z.H. Huang, T.B. Sercombe, A selective laser melting and solution heat treatment refined Al–12Si alloy with a controllable ultrafine eutectic microstructure and 25% tensile ductility, Acta Mater. 95 (2015) 74–82. doi:https://doi.org/10.1016/j.actamat.2015.05.017.

[115] X. Ding, L. Wang, Heat transfer and fluid flow of molten pool during selective laser melting of AlSi10Mg powder: Simulation and experiment, J. Manuf. Process. 26 (2017) 280–289. doi:https://doi.org/10.1016/j.jmapro.2017.02.009.

[116] P. Fathi, M. Mohammadi, X. Duan, A.M. Nasiri, A comparative study on corrosion and microstructure of direct metal laser sintered AlSi10Mg_200C and die cast A360.1 aluminum, J. Mater. Process. Technol. 259 (2018). doi:10.1016/j.jmatprotec.2018.04.013.

[117] P. Fathi, M. Rafieazad, X. Duan, M. Mohammadi, A.M. Nasiri, On microstructure

and corrosion behaviour of AlSi10Mg alloy with low surface roughness fabricated by direct metal laser sintering, Corros. Sci. (2019). doi:https://doi.org/10.1016/j.corsci.2019.05.032.